

Absolute Value of the Magnetic Penetration Depth and Field Profile in the Meissner State of Exotic Superconductors

With concentration on YBCO and Pnictides

by

Md Masrur Hossain

M.Sc., The University of British Columbia, 2006

A THESIS SUBMITTED IN PARTIAL FULFILLMENT
OF THE REQUIREMENTS FOR THE DEGREE OF

Doctor of Philosophy

in

THE FACULTY OF GRADUATE STUDIES
(Physics)

THE UNIVERSITY OF BRITISH COLUMBIA
(Vancouver)

April 2012

© Md Masrur Hossain, 2012

Abstract

One of the fundamental quantities of a superconductor is the London penetration depth, λ , which is the characteristic length scale that a magnetic field penetrates into the surface of a superconductor while in the Meissner state. In the clean limit the absolute value of λ is directly related to the superfluid density n_s via $1/\lambda^2 = \mu_0 e^2 n_s / m$ and consequently its variation as a function of temperature, doping and orientation are of central importance in testing microscopic theories of exotic superconductors. Low energy (≤ 30 keV) μ SR beam of muon (μ^+) such as in Paul Scherrer Institut (PSI), Switzerland, is ideal to measure London penetration depth λ . When a muon (μ^+) decays, it emits a fast decay positron preferentially along the direction of its spin due to the parity violating decay. The time evolution of statistical average direction of the spin polarization of the muon ensemble depends very sensitively on the spatial distribution and dynamical fluctuations of the muons' magnetic environment.

In this thesis, accurate measurements of λ and the anisotropies ($\equiv \lambda_a / \lambda_b$) have been done for three different oxygen ($x = 6.52, 6.92, 6.998$) contents of $\text{YBa}_2\text{Cu}_3\text{O}_{6+x}$ and for $\text{Ba}(\text{Co}_{0.07}\text{Fe}_{0.93})_2\text{As}_2$. The measured values of λ and the anisotropies are considerably different from that of literature, often found with indirect methods. We observe an exponential decay of the magnetic field and corresponding supercurrent density deep inside the crystals. Small deviations from the London model are observed which indicate there is a suppression of the supercurrent density close to the surface. The measured (λ) values are also found to depart substantially from the widely reported relation ($T_c \propto 1/\lambda_a^2$).

Preface

Results presented in section 4.1.1 has been published [1], under the title "Direct measurement of the London penetration depth in $\text{YBa}_2\text{Cu}_3\text{O}_{6.92}$ using low-energy μSR " with me being the second author. Sections 4.1.2 and 4.1.3 are currently in the process of being published. The design of research methods, literature review, data analysis, were done by myself in consultation with my supervisor R. F. Kiefl. Manuscript of the published paper [1] was written primarily by R. F. Kiefl. The co-authors have been partly involved in taking the data and reviewing and commenting on the manuscripts, or supplying the studied samples. The results presented in section 4.2 is published in Physical Review B(R) [2]. A significant of part of data analysis was done by me. Manuscript was written by O. Ofer & microwave analysis was done by J. C. Baglo.

The large majority of figures presented in this thesis are vector graphics, i.e, can be zoomed to inspect specific areas without any loss of resolution. To avoid large whitespaces in figures, they are purposefully made compact.

This document is best viewed with freely available [Adobe Reader](#). Other suboptimal viewers (in order of preference) are Preview (Machintosh only), [Foxit Reader](#) (Windows only), [Evince](#) (Go Forward/Backward links nonresponsive), [Okular](#) (appearance of broken lines in figures).

Table of Contents

Abstract	ii
Preface	iii
Table of Contents	iv
List of Tables	vi
List of Figures	vii
List of Symbols	ix
Glossary	x
Acknowledgments	xi
1 Introduction	1
1.1 Brief History Of Superconductivity	1
1.2 Brief Review Of Superconducting Properties	3
1.3 High Temperature Superconductivity: A Review	5
1.3.1 Cuprates: CuO ₂ Layer Based High-T _c Superconductor	5
1.3.2 Pnictide: A New Type Of High-T _c Superconductor	10
1.4 Pairing Symmetry And Magnetic Penetration Depth Measurement	13
2 Theory	16
2.1 BCS Theory	16
2.2 London Penetration Depth	17
2.3 Pairing Mechanism And Order parameter symmetry	20
3 Experimental Techniques	23
3.1 Introduction To μ SR	23
3.1.1 Properties And Production Of Muons	23
3.1.2 General μ SR Techniques	26

3.2	Low Energy μ SR	26
3.2.1	Principles Of LE- μ SR	27
3.2.2	Stopping Distribution	31
4	Results & Analysis	33
4.1	LE- μ SR experiments on $\text{YBa}_2\text{Cu}_3\text{O}_{6+x}$ single crystals	34
4.1.1	$\text{YBa}_2\text{Cu}_3\text{O}_{6.92}$	35
4.1.2	$\text{YBa}_2\text{Cu}_3\text{O}_{6.998}$	42
4.1.3	$\text{YBa}_2\text{Cu}_3\text{O}_{6.52}$	48
4.2	Pnictide	57
4.3	Summary Of Results	63
4.4	Discussion On “Deadlayer”	67
5	Conclusions & Outlook	70
	Bibliography	71

List of Tables

Table 3.1	Properties of Muon	26
Table 4.1	Summary of results in $\text{YBa}_2\text{Cu}_3\text{O}_{6.92}$	41
Table 4.2	Summary of results for $\text{YBa}_2\text{Cu}_3\text{O}_{6.998}$	47
Table 4.3	Summary of results in $\text{YBa}_2\text{Cu}_3\text{O}_{6.52}$	57
Table 4.4	Pnictide Two Fields	64
Table 4.5	Measurements of the absolute value of the magnetic penetration depth ($\lambda_{a,b}$) in $\text{YBa}_2\text{Cu}_3\text{O}_{6.52}$, $\text{YBa}_2\text{Cu}_3\text{O}_{6.92}$ and $\text{YBa}_2\text{Cu}_3\text{O}_{6.998}$	66

List of Figures

Figure 1.1	Approximate number of publications on superconductivity	2
Figure 1.2	External field expulsion in Meissner state	2
Figure 1.3	History of superconducting critical temperature (T_c)	4
Figure 1.4	Simplified phase diagram of type I & II superconductors	4
Figure 1.5	A schematic model of the electronic/magnetic structure of the HTSC vortex core	5
Figure 1.6	Stoichiometric crystal structure of YBCO	7
Figure 1.7	Schematic phase diagram of cuprate superconductors	8
Figure 1.8	Two models for high- T_c superconductivity	9
Figure 1.9	Crystal structure of Pnictide	11
Figure 1.10	Phase diagram for $\text{BaCo}_x\text{Fe}_{2-x}\text{As}_2$	12
Figure 2.1	BCS model of electron interactions in superconductors	16
Figure 2.2	Temperature dependence of the superconducting energy gap in the weak coupling limit of BCS interaction	17
Figure 2.3	Density of electronic states in s & d wave superconductivity	18
Figure 2.4	Modified London model of exponential decay of external magnetic field .	20
Figure 2.5	A schematic representation of the superconducting (s, d and s_{\pm} wave) order parameters	22
Figure 3.1	Positively charged pion decay into muon and a neutrino	24
Figure 3.2	Angular probability distribution of positrons emitted from muons	24
Figure 3.3	Schematic of the arrangement for a TF- μ SR experiment	25
Figure 3.4	LE- μ SR experimental setup	28
Figure 3.5	Histogram of raw counts & asymmetry for a particular positron detector	31
Figure 3.6	Muon implantation profiles and average depth ($\langle z_{\mu} \rangle$) in YBCO	32
Figure 4.1	Quick outline of fitting procedure in normal and superconducting states	34
Figure 4.2	YBCO-II mosaic of small crystals	35
Figure 4.3	Measured surface roughness of YBCO crystals	36

Figure 4.4	The muon spin precession signal in the normal and superconducting state of $\text{YBa}_2\text{Cu}_3\text{O}_{6.92}$	36
Figure 4.5	Magnetic field distribution inside YBCO-I	37
Figure 4.6	The average magnetic field ($\langle B \rangle_{a,b}$) versus mean stopping depth in an applied field of 9.46 mT	39
Figure 4.7	The muon spin precession signal in the normal and superconducting state of $\text{YBa}_2\text{Cu}_3\text{O}_{6.998}$	42
Figure 4.8	Magnetic field distribution inside YBCO-II	43
Figure 4.9	Asymmetry, phase and broadening parameter for experiments on $\text{YBa}_2\text{Cu}_3\text{O}_{6.998}$	44
Figure 4.10	YBCO 6.998 average magnetic field $\langle B \rangle_{a,b}$ inside $\text{YBa}_2\text{Cu}_3\text{O}_{6.998}$	45
Figure 4.11	Comparison of average magnetic field in two magnetic field	46
Figure 4.12	Temperature dependence of London penetration depth in $\text{YBa}_2\text{Cu}_3\text{O}_{6.998}$	46
Figure 4.13	Summary of results for $\text{YBa}_2\text{Cu}_3\text{O}_{6.998}$	49
Figure 4.14	$\text{YBa}_2\text{Cu}_3\text{O}_{6.52}$ spectra in ± 1.45 mT	50
Figure 4.15	The muon spin precession signal in the normal & superconducting state of $\text{YBa}_2\text{Cu}_3\text{O}_{6.52}$	51
Figure 4.16	YBCO 6.52 broadening parameter (σ) are shown for an external applied field of 1.45 mT, 4.6 mT and 7.8 mT	52
Figure 4.17	Magnetic field distribution inside YBCO-II	52
Figure 4.18	Global fit λ and individually fitted λ 's are shown for an external field of 1.5 mT	53
Figure 4.19	YBCO 6.52 average magnetic field $\langle B \rangle_{a,b}$ inside $\text{YBa}_2\text{Cu}_3\text{O}_{6.52}$	54
Figure 4.20	YBCO 6.52 average magnetic field $\langle B \rangle_{a,b}$ inside $\text{YBa}_2\text{Cu}_3\text{O}_{6.52}$	55
Figure 4.21	Temperature dependence of λ in external fields of 1.45 and 4.6 mT	55
Figure 4.22	Asymmetry, phase (φ), broadening parameter (σ) and the goodness of fit χ^2/DF for three different external fields	56
Figure 4.23	Muon precession signals in $\text{Ba}(\text{Co}_x\text{Fe}_{1-x})_2\text{As}_2$ in an applied field of $\mu_0 H = 4.7$ mT	58
Figure 4.24	Broadening parameter (σ) in $\text{Ba}(\text{Co}_x\text{Fe}_{1-x})_2\text{As}_2$ in external applied fields of $\mu_0 H = 2.5$ mT and 4.7 mT	59
Figure 4.25	The average magnetic field versus the muon energy in Pnictide	60
Figure 4.26	Magnetic field distribution inside Pnictide	61
Figure 4.27	The temperature dependence of λ plotted versus $t = T/T_c$	61
Figure 4.28	The temperature dependence of ρ plotted versus T/T_c	63
Figure 4.29	T_c vs $\lambda_{a,b}$	65
Figure 4.30	External field decay in the case of a rough surface	68
Figure 4.31	Simulated external field fitted to the London model function for the depth range 0 to 10λ . Only the region of $0-\lambda$ is shown.	69

List of Symbols

$\Delta(k, T)$	Momentum & energy dependent superconducting energy gap, page 16	eV
κ	Ginzburg-Landau parameter, page 3	
T_c	Superconducting critical temperature, page 1	K
ξ	Ginzburg-Landau coherence length, page 5	m
λ	London penetration depth, page 1	m
λ_{ab}	Average magnetic penetration depth, page 65	m
ϕ_0	Unit of flux quantum, page 5	
ψ	Superconducting order parameter, page 1	
σ	Optical conductivity, page 10	
τ	Relaxation time, page 18	
H_c	Critical magnetic field, page 3	Tesla
n_s	Superfluid density, page 5	
T^*	Strange metallic phase temperature, page 8	K
γ_μ	Muon gyromagnetic ratio, page 26	MHz/Tesla
$\mathcal{A}(t)$	Time dependent muon asymmetry, page 33	
\mathcal{R}	Ratio of magnetic penetration depth, ie, $\frac{\lambda_a}{\lambda_b}$, page 45	
τ_μ	Muon lifetime, page 26	s

Glossary

UBC University of British Columbia

PSI [Paul Scherrer Institute, Villigen, Switzerland](#)

CIFAR [Canadian Institute for Advanced Research, Canada](#)

TRIUMF [TRI-University Meson Facility, Canada](#)

NSERC [Natural Sciences and Engineering Research Council of Canada](#)

YBCO Yttrium barium copper oxide/ $\text{YBa}_2\text{Cu}_3\text{O}_{6+x}$

FE-PNICTIDE Fe-As based superconductors

MUSR Muon spin [resonance/rotation/relaxation](#)

QCP Quantum Critical Point

HTSC High Temperature Superconductor

ODLRO Off Diagonal Long Range Order

YBCO-I $\text{YBa}_2\text{Cu}_3\text{O}_{6.92}$

YBCO-II $\text{YBa}_2\text{Cu}_3\text{O}_{6.998}$

YBCO-III $\text{YBa}_2\text{Cu}_3\text{O}_{6.52}$

Acknowledgments

First and foremost I would like to thank my supervisor Rob Kiefl and his support and advice throughout the course of my PhD. I am very grateful for his responses to my inquiries and availability during my entire stay at UBC. I would also like to thank my committee members: D. A. Bonn, M. Franz, and A. Damascelli for their comments, and for reading the thesis.

I also thank Zaher Salman and Gerald Morris who have always been very helpful in providing software expertise and acting as general UNIX/LINUX gurus. Zaher's super-fast response to queries for technical help has been invaluable in many occasions. Special thanks to D. Arseneau for letting me use the fastest computer in μ SR group in TRIUMF. This has saved many precious hours of analysis time & possible frustrations. Many thanks to R. Liang for providing the YBCO samples with 3 different oxygen contents. Also thanks to AMES laboratory for providing the FE-PNICTIDE samples.

I wish also to thank my colleagues in β -NMR group. Special thanks to Susan Q. Song for helping taking magnetization data at AMPEL. A big thanks to J.C. Baglo for providing supplementary microwave analysis. My colleagues Terry Parolin, Dong Wang, Micheal Smadella, Hassan Saadaoui, Susan Q. Song, J.C. Baglo and others have spent many nights taking the actual data; for that and for the helpful discussions and good times we had together, I am very grateful.

The data in this project was taken over many years and a lot of people, other than the ones that have been already mentioned above, have helped to take shifts & helped doing supplementary analysis. I will also like to thank μ SR support staff & colleagues at PSI, B. M. Wojek, T. Prokscha, A. Suter. Special thanks goes to B. M. Wojek for his critical & thorough analysis of data and valuable insight.

I would like to mention the β -NMR technical support staff R. Abasalti, D. Arseneau, K. H. Chow, S. Dunsiger, B. Hitti, C. D. P. Levy, R. Miller, M. R. Pearson, and D. Vyas.

The μ SR measurements were performed at PSI. These works were supported by NSERC, CIFAR and the U.S. Department of Energy.

Finally, thanks to the writers of \LaTeX and many accompanying packages, used in typesetting this thesis.

2 Introduction

1.1 Brief History Of Superconductivity

4 HISTORICALLY superconductivity has played an important role in condensed matter
5 physics. With the discovery of superconductivity in Hg [3], hundred years ago, it
6 remains a very active area of research and continuing surprises. Figure 1.1 roughly
7 shows the number of publications on the phenomenon of superconductivity in the last decade.
8 Before the discovery of the phenomena of superconductivity, it was known that the resistivity
9 of a metal drops with decreasing temperature. Resistivity in metals is generally attributed
10 to electron-phonon scattering, the rate of which is proportional to the thermally excited
11 phonons. However, the number of thermally excited phonons is finite above absolute zero
12 and thus the resistivity is expected to be non zero at any finite temperature. Consequently, K.
13 Onnes' discovery of virtual absence of resistivity in Mercury below 4.15K, in 1911 [4] was
14 rather surprising. Soon after, in 1913, Lead was found to be superconducting below 7.2K
15 and after 17 years of this discovery, niobium was found to be superconducting at 9.2K. The
16 virtual absence of resistance in superconductor has been demonstrated by experiments with
17 persistent currents in superconducting rings. Such currents have a decay time of magnitude
18 of 10^5 years. The other important characteristic beyond zero resistivity is the phenomenon of
19 the Meissner effect in which magnetic field is expelled ([5] figure 1.2) out of a sample when
20 it's cooled below the so called critical temperature T_c . The phenomenon of the Meissner effect
21 is different from perfect diamagnetism. In perfect diamagnetism, currents are generated to
22 oppose any change in applied field. However, if the sample already had non-zero magnetic
23 flux through it, cooling through T_c wouldn't make any change in the field whereas, in
24 the Meissner effect, the field would be expelled from the sample when cooled below T_c .
25 This phenomenon of the Meissner effect led London brothers [6] to propose equations to
26 predict how the field is excluded from the sample and in particular, the field penetration
27 near the surface. Londons' theory was later (1950) derived from the phenomenological
28 theory of Ginzburg and Landau [7] (GL), who described superconductivity in terms of a
29 macroscopic complex order parameter ψ which roughly dictates the extent to which a system
30 is ordered. In the case of superconductivity, the amplitude of order parameter is proportional
31 to superconducting electron density.

32 Although the phenomenological GL theory had been successful, the microscopic theory

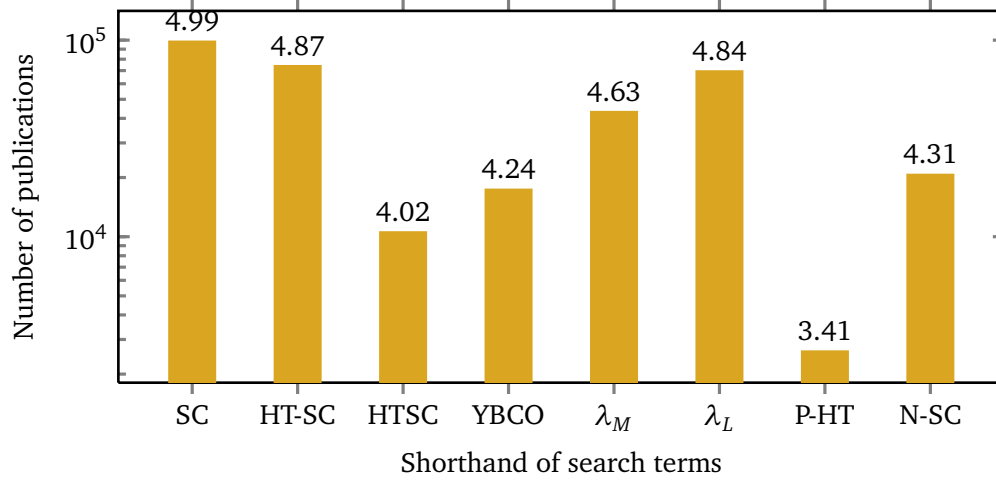


Figure 1.1: Number of publications (year 2000 onwards) in log scale, for different search terms from a prominent search engine's scholar edition, done on January 17, 2012. Expansion of the shorthand terms: SC: superconductivity; HT-SC: high temperature superconductivity; HTSC: HTSC; YBCO: YBCO; λ_M : magnetic penetration depth; λ_L : London penetration depth; P-HT: pseudogap in high temperature superconductivity; N-SC: normal state in high temperature superconductivity. As may be seen, an enormous scholarly interest in the phenomenon of superconductivity exists in the contemporary physics.

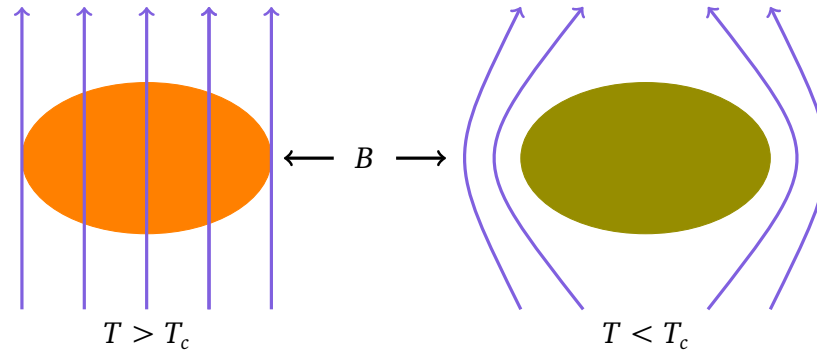


Figure 1.2: Meissner effect for a type I superconductor. When a superconductor is placed in an external magnetic field H and cooled below its superconducting temperature T_c , the magnetic flux is abruptly expelled. For $B < B_c$, it penetrates the surface of the superconductor within the penetration depth λ .

only came in 1957 from J. Bardeen, Leon Cooper and John Schrieffer [8, 9], now famously known as BCS theory. BCS theory explains superconductivity in terms of electron-electron interaction mediated by sound waves (phonons) and predicted that superconductivity may be found with critical temperature $T_c \leq 23$ K. The carriers of supercurrents were shown to be a pair of electrons (“Cooper pairs” [10]) with opposite spin and momentum. Many new metals and alloys with superconducting properties, at low temperatures, were found by 1980, with the noted exceptions of ferromagnets such as Fe, Ni. It was later realized that magnetic order is antagonistic to superconductivity.

In 1986, J.G. Bednorz and K.A. Muller [11] discovered superconductivity in $\text{La}_{2-x}\text{Ba}_x\text{CuO}_4$ at 35K, thus initiating the era of high-temperature superconductivity. Building on that, Maw-Kuen Wu and his graduate students, Ashburn and Torng [12] at the University of Alabama discovered YBCO has a T_c of 93 K. Their work led to a rapid succession of new high temperature superconducting materials, ushering a new era in material science and chemistry. YBCO was the first family of materials to become superconducting above 77 K, the boiling point of liquid nitrogen. All materials developed before 1986 became superconducting only at temperatures near the boiling points of liquid helium ($T_b = 4.2$ K) or liquid hydrogen ($T_b = 20.28$ K) the highest being Nb_3Ge at 23 K. Although met with initial skepticism, the observations were validated when Uchida *et. al.* and Chu *et. al.* reproduced original results in 1987. In 2008, one new family of Fe-based superconductors were discovered. Due to the typical antagonistic relationship of superconductivity and magnetism, this was quite surprising. Remarkable progress has been made in discovering high- T_c superconductors as shown in the figure 1.3. As superconductivity is found in so many different material families, it is considered a robust phenomenon; however high- T_c superconductivity has many open questions.

1.2 Brief Review Of Superconducting Properties

Besides having a critical temperature T_c , superconductors also have critical magnetic fields (H_c), above which their properties change. In this respect, superconductors are classified in two broad categories (figure 1.4), i) Type I, in which the material becomes normal above a critical magnetic field $H_{c,0}$. ii) Type II, in which the material has two critical magnetic fields H_{c1} and H_{c2} . In type II, at $H < H_{c1}$, the material remains in the Meissner state and at $H_{c1} < H < H_{c2}$, magnetic field penetrate the material in quantized vortices (for a very detailed review, consult [14]) and for $H > H_{c2}$, it becomes normal. Two other parameters characterize superconductivity in general, namely the coherence length ξ and the magnetic penetration depth λ . The coherence length ξ is the distance over which order parameter ψ varies appreciably and penetration depth λ is the depth over which shielding currents circulate to expel the applied external field. λ and ξ are two fundamental length scales in superconductivity. Other parameters of interest such as Ginzburg-Landau parameter $\kappa = \frac{\lambda}{\xi}$, two critical fields H_{c1} , H_{c2} , thermodynamical critical field H_c may be derived from them.

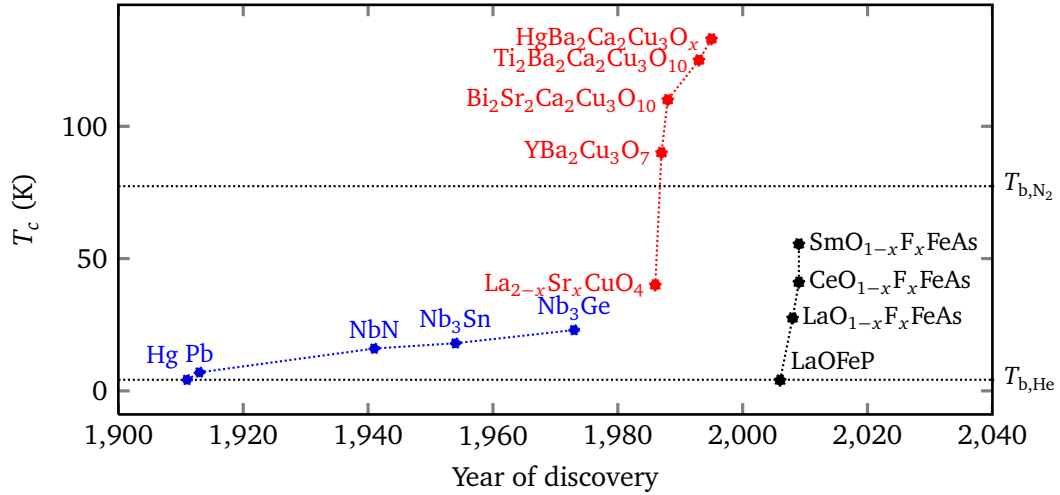


Figure 1.3: Superconducting critical temperature ([13]) T_c has risen almost linearly with time, from 4 K to 40 K till about 1986. Around 1987, one of the CuO based high temperature superconductor family was found. In 2008, one new family of Fe-based superconductors were discovered. Due to the typical antagonistic relationship of superconductivity and magnetism, this was a significant surprise for science.

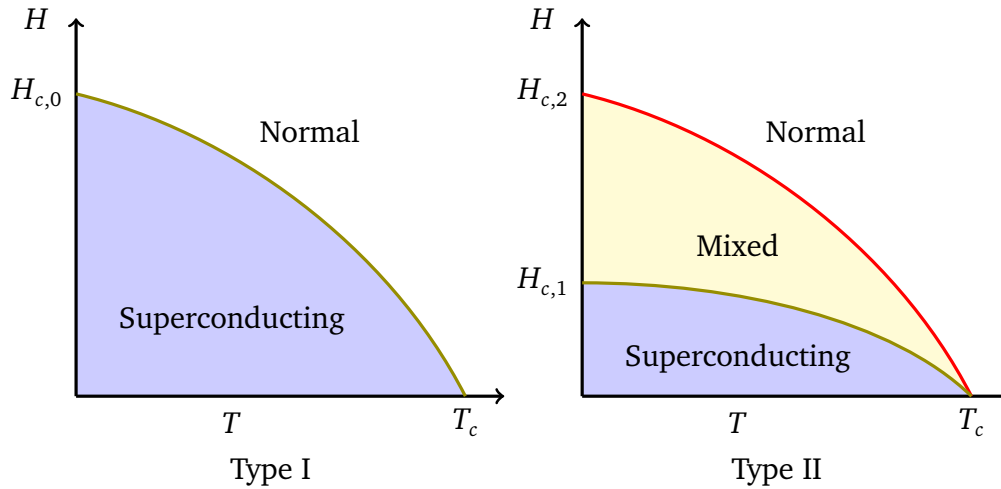


Figure 1.4: Superconductivity is destroyed when external field is too large or temperature too high. Superconductors are divided in two classes depending on the manner of this destruction. For type I superconductors, superconductivity is abruptly destroyed in a first order phase transition if $H > H_c$ or $T > T_c$. Type II superconductivity has a complete Meissner region (below $H < H_c$) in $H-T$ phase diagram, however, in the “Mixed” ($H_{c1} < H < H_{c2}$) state, laminar vortices with normal state cores enter into superconductor and superconductivity is destroyed in a continuous 2nd order phase transition to a normal state. Most high- T_c superconductors are type II.

1 The normal regions (“vortices”) in a “mixed state” of a type II superconductor are
2 configured to maximize surface area and minimize volume while keeping the magnetic flux
3 constant. Abrikosov showed that this occurs if vortices are cylindrical and parallel to the
4 local field direction. At the center of a vortex, superconductivity is completely destroyed,
5 i.e, order parameter $|\psi|^2$ vanishes (figure 1.5). However, the velocity of the carriers tend to
6 increase as we approach the core. Within a radial distance of ξ , carrier density n_s reaches its
7 bulk value. The radius ξ is known as “vortex core” and contains exactly one quantum of
8 magnetic flux $\phi_0 = \frac{c\hbar}{2e}$. The supercurrent flowing around the vortex produces a magnetic
9 field which is maximum at the center and decays approximately exponentially, with a length
10 scale of λ in the radial direction. The vortices are usually arranged in a periodic lattice
11 known as the Abrikosov lattice, the flux lattice or the flux line lattice. Vortices may also be
12 dynamic and interacting depending on the level of doping and the magnetic field [15].

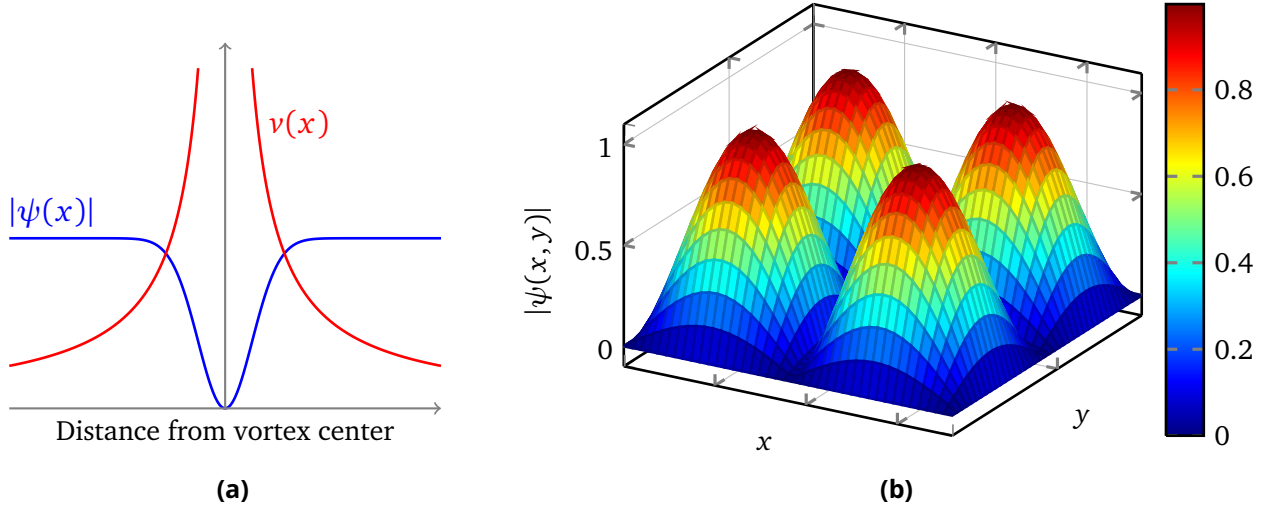


Figure 1.5: Left: A schematic model of the electronic/magnetic structure of the HTSC vortex core. Superfluid velocity $v(x)$ rises and the HTSC order parameter $|\psi(x)|$ falls as the core is approached. Right: The superconducting order is suppressed at the cores of the vortices. The colored surface shows the envelope of this order parameter, superimposed on the vortex lattice. This type of order can be static or dynamically fluctuating depending on the level of doping and the magnetic field.

1.3 High Temperature Superconductivity: A Review

1.3.1 Cuprates: CuO_2 Layer Based High- T_c Superconductor

15 Discovery of superconductivity in the ceramic materials (with copper oxides) has led to
16 a pursuit to understand this new phenomenon. This new type of superconductivity is
17 considerably different from the “conventional” (i.e, BCS)-type superconductivity & exact
18 microscopic mechanism is so far debated. However, significant inroads have been made in
19 understanding different aspects of this “unconventional” superconductivity.

1 A traditional description of electronic behavior in solids is modeled after Drude, Sommer-
 2 field, Wiedemann and Franz, where heavier positively charged cores of atoms form periodic
 3 lattice and are immobile and electrons are almost free as in gas molecules in a jar, aptly
 4 named as “free electron gas”. This theory is also known as Landau’s “Fermi-liquid theory”.
 5 The Wiedemann-Franz (WF) law (an empirical observation) is one of the basic properties of
 6 a Fermi liquid, reflecting the fact that the ability of a “free electron” to transport heat is the
 7 same as its ability to transport charge, provided it cannot lose energy through collisions and
 8 is written as

$$\frac{k}{\sigma T} = \frac{\pi^2}{3} \left(\frac{k_B}{e} \right)^2 = \text{constant} \quad (1.1)$$

9 where k and σ are the heat/electrical conductivity, respectively. In high- T_c cuprate supercon-
 10 ductor $(\text{Pr,Ce})_2\text{CuO}_4$, the WF law is violated in the normal state, suggesting that elementary
 11 excitation that carry heat in this material are not fermions[16]. The Fermi-liquid description
 12 is highly successful in explaining metallic, insulating and semiconducting behavior, however
 13 fails to account for unconventional superconductivity where electron-electron interaction
 14 is too strong. Strong Coloumb repulsion among electrons lead to antiferromagnetic Mott
 15 insulating behavior in CuO materials at a composition where “free electron gas” theory
 16 predicts a metal. Changes in composition (O doping) leads to many exotic phenomenon
 17 such as superconductivity, charge ordering, strange metallicity, quantum criticality and Fermi
 18 liquid phenomenon. A Mott insulator is very different from a regular (band) insulator. In
 19 a band insulator, lack of conductivity arises due to Pauli exclusion principle as the highest
 20 occupied band contains two electrons per unit cell and all the orbitals are filled. In a
 21 Mott insulator, due to strong Coloumb repulsion, charge conduction is blocked, leaving
 22 charge per unit cell fixed with electron spins fluctuating at each site. This fluctuation is
 23 antiferromagnetic (figure 1.8) in nature. Doping (hole/electron) restores some electrical
 24 conductivity by creating sites to which electrons can jump without having to gain additional
 25 Coloumb energy.

26 High-temperature superconductivity arises in a family of layered copper oxides that all
 27 feature weakly coupled square-planar sheets of CuO_2 . Structure of one of the member of this
 28 family, $\text{YBa}_2\text{Cu}_3\text{O}_{7-\delta}$ (hereafter “YBCO”, possibly the most studied) is shown in figure 1.6,
 29 as this material was a subject of this research. For $\text{YBa}_2\text{Cu}_3\text{O}_7$, three copper-oxygen layers
 30 are stacked along the tetragonal \hat{c} axis. Two of these layers have oxygen atoms between
 31 the copper ions in both the \hat{a} and \hat{b} directions, and are called CuO_2 plane layers. The third
 32 layer, called the CuO chain layer, has oxygen ions only along the \hat{b} direction [19]. The phase
 33 diagram for YBCO, dependent on oxygen(hole) doping, is shown schematically in figure 1.7.
 34 As may be noted from the phase diagram, with increased hole doping, antiferromagnetic
 35 insulating state turns to be superconducting. The dependence of critical temperature $T_c(p)$

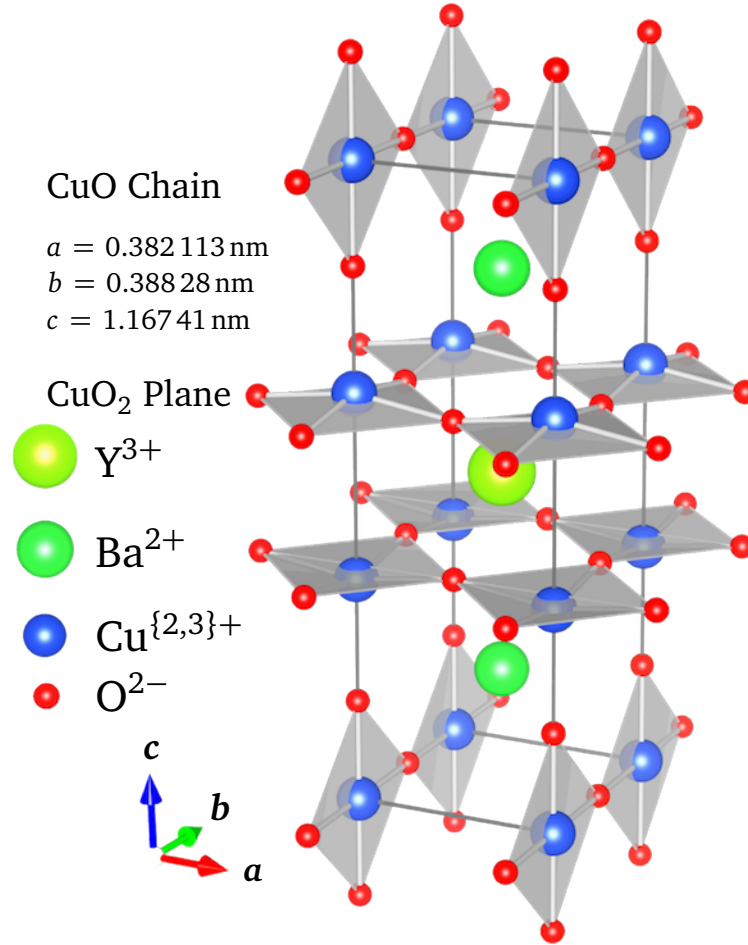


Figure 1.6: YBCO consists of CuO₂ planes & CuO chains. Each plane layer consists of a single Cu atom sharing with four Oxygen vertices and perpendicular to these CuO₂ planes, are CuO chains where each Cu atom shares two oxygen vertices. The Yttrium atoms are found between CuO₂ planes, while the Barium atoms are found between CuO₂ planes and CuO chains. YBa₂Cu₃O₇ is a well-defined chemical compound with a specific stoichiometry. Non-stoichiometry is defined by oxygen vacancies as in YBa₂Cu₃O_{7-x}. With $x = 1$, O(1) sites in CuO₂ planes are vacant and the structure is tetragonal and insulating. For $x < 0.65$, CuO chains along b -axis start to form and the structure becomes orthorhombic. Maximum $T_c \sim 95 \text{ K}$ occurs for $x \sim 0.8$ [17, 18].

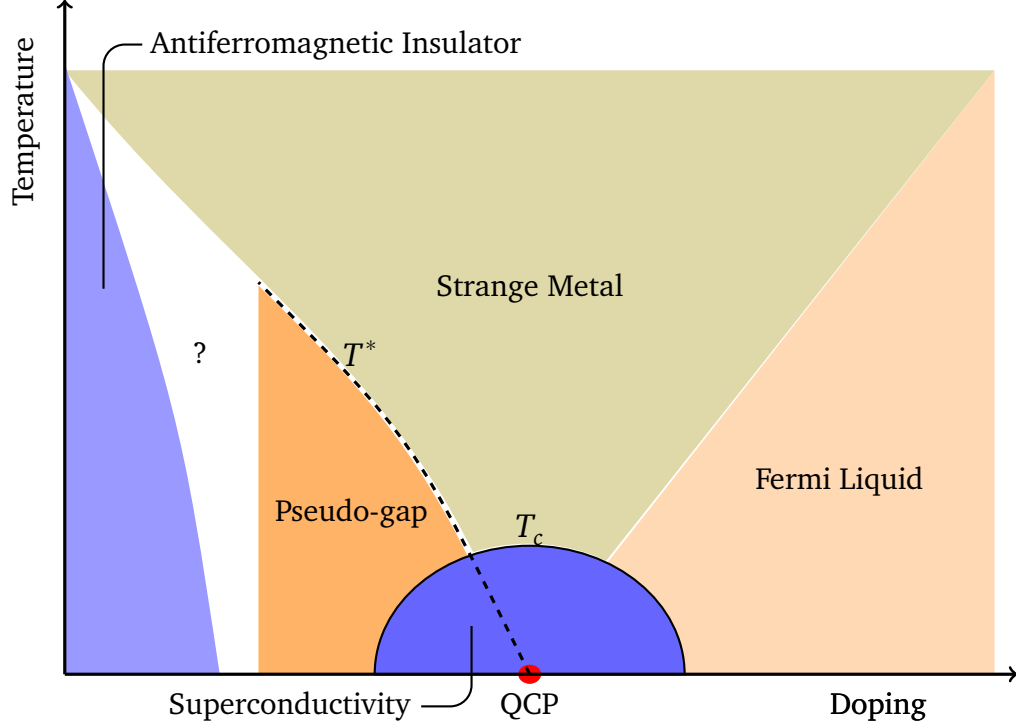


Figure 1.7: Schematic phase diagram: At very low levels of electron-hole doping, cuprates are insulating and antiferromagnetic (the materials' neighboring spins point in opposite directions). At increased doping levels, they become conducting, and the exact temperature and doping level determine which phase of matter they will be in. At temperatures below T_c , they become superconducting, and at temperatures above T_c but below T^* they fall into the pseudogap phase. The boundary of the pseudogap region at low doping levels is unknown. The transition between the Fermi-liquid phase and the strange-metal phase occurs gradually (by crossover). QCP denotes the quantum critical point at which the temperature T^* goes to absolute zero.

1 on doping is given by an empirical relationship [20],

$$T_c(p) = T_{c,\max} \left[1 - 82.6(p - 0.16)^2 \right], \quad (1.2)$$

2 where doping level p varies from 0.05 to 0.27. The proximity of antiferromagnetism and
3 superconductivity gives rise to the conjecture that superconductivity is driven by magnetic
4 interactions between electrons rather than pairing via phonons. Also important to note that,
5 a signature of lattice vibration driving superconductivity, ie, the “isotope effect” has not
6 been observed in high temperature superconductivity. However there has been renewed
7 interest in the possible role of electron-lattice coupling [21–26] in high- T_c superconductivity,
8 although the role is suggested to be indirect [26] and small [23, 27]. A possible mechanism
9 proposed by P. W. Anderson [28] is that “quantum fluctuations” may create instability in the

1 antiferromagnetic order and give rise to resonating valence bond [29–31] in which the spins
 2 form a “spin-liquid” phase of singlet($s = 0$) pairs. “Spin liquid” is defined to be aggregation
 3 of pairs of antiparallel spins. The motion of such singlet pairs is similar to the resonance of
 4 π bonds in benzene, originating the term “resonating valence bond” (RVB), schematically
 5 shown in figure 1.8. In this picture, electrons are paired up in antiparallel spin-formation
 6 but cannot move due to Coloumb repulsion. Reducing average occupancy, from one, will
 7 make these singlet pairs mobile, Anderson argued, giving rise to superconductivity. In
 contrast, YBCO was found out to be antiferromagnets and not spin-liquid phase [32–34]. It

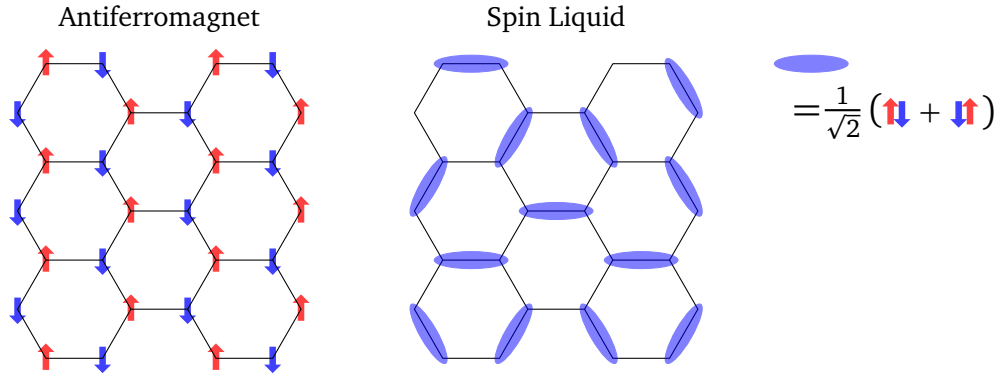


Figure 1.8: An example of a short range “resonating valence bond” (an aggregation of antiparallel neighboring spins). An oval represents a superposition of different possible spin configurations. This is a “spin-liquid” since there is no static order but their motions are highly correlated. Motions of singlet pairs are hindered due to Coloumb repulsion. Reducing average occupancy from one may make these singlet pairs mobile.

8

9 has been established that in cuprate systems, antiferromagnetic ordering resides entirely
 10 on the CuO_2 plane [35, 36], with a three-dimensional magnetic transition dictated by
 11 very weak coupling between planes. As seen in the phase diagram in figure 1.7, T_c varies
 12 (peaks at “optimal” doping) as a function of doping and is a well observed phenomenon in
 13 all CuO_2 layer based superconductors [37]. With increased doping 3D antiferromagnetic
 14 ordering gives way to a disordered state with short range correlations [37], thereby retaining
 15 some magnetism. At $T > T_c$, metallic behavior is observed for a broad range of dopings
 16 & d.c electrical resistance is T -dependent rather than T^2 -dependent as would have been
 17 expected from a normal metal Fermi liquid behavior. In the overdoped regime, the copper
 18 oxides behave more like ordinary metals with a T^2 dependence of d.c resistivity [38]. A
 19 naturally overdoped Copper oxide $\text{TlBa}_2\text{Cu}_3\text{O}_{6+x}$ has been observed to show polar angular
 20 magnetoresistance oscillation [39, 40], in high field, establishing the existence of a 3D Fermi
 21 surface, consistent with the prediction from single electron band theory, i.e, metallic behavior.
 22 However, the existence of 3D coherent Fermi surface poses a challenge to the widely held
 23 belief and experimental evidence [41] that high- T_c superconductivity arises from purely 2D

1 electron motion within the CuO_2 planes. In underdoped regime, copper oxides have been
2 found to show quantum oscillations [42], an indication of metallic behavior, in de Haas-van
3 Alphen spectra. As may be noted in phase diagram Cu-O based superconductors includes a
4 “pseudogap” region [41, 43], a precursor to the superconducting state. It has been shown
5 that this phase originates in CuO_2 planes and not in the CuO chains [44]. Whether this is
6 a distinct phase of matter is still under debate [45]. It is metallic, however some parts of
7 the Fermi surface show gaps [41, 43, 46]. If it exists, a quantum critical point [47–49] in
8 the cuprates would also probably be the end point of a line(T^*) [50] of phase transitions
9 that separates the pseudogap and strange-metal regions. It has also been suggested that
10 the phase diagram is controlled by a quantum critical point [51, 52]. A QCP develops in a
11 material at absolute zero temperature when a new form of order emerges from its ground
12 state. QCP is a phenomenon of great interest because of their ability to influence the finite
13 temperature properties of materials. The “normal” region (“strange metal”) above transition
14 temperature T_c is of very unusual properties [53–55] (thermal conductivity $k(T)$, optical
15 conductivity $\sigma(\omega)$, the nuclear relaxation rate $T_1^{-1}(T)$), with large temperature-dependent
16 resistivity implying a scattering rate linear in T , however several orders of magnitude of the
17 average excitation energy $k_B T/h$ [56, 57].

18 With all the significant differences from conventional superconductivity, supercurrent
19 is still carried by electron pairs, shown via quantization of magnetic flux in units of $\frac{h}{2e}$
20 [58–60]. Most of the physical properties of the CuO_2 have experimentally been established
21 with a high degree of reliability and advances in preparing the materials are such that
22 spurious effects and uncertainties in materials compositions, homogeneities and impurity
23 content may be eliminated as hindrance to the understanding of the phenomenon of high- T_c
24 superconductivity. In spite of substantial efforts in both experimental and theoretical
25 research, there are many open questions regarding mechanism for high- T_c superconductivity.

1.3.2 Pnictide: A New Type Of High- T_c Superconductor

27 Because of the typically antagonistic relationship between superconductivity and magnetism
28 has led researchers to avoid using magnetic elements (eg. Fe) in particular, as potential
29 building blocks of new superconducting materials. The recent (2008) discovery of super-
30 conductivity at T_c 's up to 55 K in iron pnictide systems [61–65] has sparked enormous
31 interest in this class of materials. Even more surprising is that pnictide is the only material
32 other than cuprates (CuO_2 layer based superconductors) to have T_c higher than 40 K (\sim BCS
33 theoretical maximum). The crystal structure of the parent compound BaFe_2As_2 is shown in
34 the figure 1.9 as a Co-doped pnictide ($\text{Ba}(\text{Co}_{0.074}\text{Fe}_{0.926})_2\text{As}_2$) is a subject of this work.

35 Cuprates and pnictides show similar behavior in many aspects, such as (i) both are
36 layered structures, (ii) parent (non-superconducting) compounds are antiferromagnets,
37 although with possibly different electronic correlation strengths, (iii) both materials show
38 superconducting order upon doping. Striking dissimilarities are also abound: (i) parent

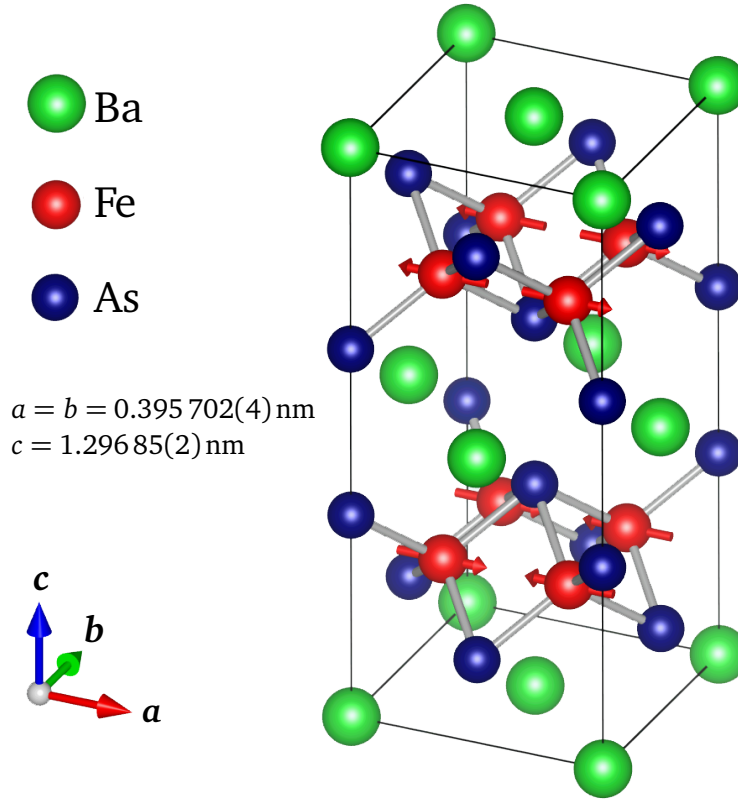


Figure 1.9: Left: Pnictide crystal structure [66] shows the antiferromagnetic alignment and magnetic moment (red arrows) both along the longer a axis in the FeAs plane. The magnetic unit cell is the same as the orthorhombic chemical unit cell.

1 compound for cuprates are Mott insulators while for pnictides, they are semimetals, (ii)
 2 cuprates are essentially one-band while iron pnictides have multibands at the Fermi energy,
 3 (iii) superconducting gap function is d -wave in cuprates whereas for pnictides, strong
 4 contender is an “extended s -wave”, also called s_{\pm} .

5 Two families(parent materials) of pnictides have so far been discovered: originating from
 6 RFeAsO [64] (R =rare earth, abbreviated as 1111 for its 1:1:1:1 ratio of the four elements)
 7 and AFe_2As_2 [67] (A =alkaline, the 122 compounds) earth metal, which are tetragonal at
 8 room temperature but undergo an orthorhombic distortion in the range 100 K to 200 K that
 9 is associated with the onset of antiferromagnetic order [66, 68–72]. Tuning the system
 10 via element substitution [73, 74] or oxygen deficiency [75, 76] suppresses the magnetic
 11 order and structural distortion in favor of superconducting T_c 's up to 55 K, with an overall
 12 behavior strikingly similar to the high- T_c copper oxide family of superconductors. However,
 13 the induction of superconductivity by doping Co or other transition metals into the Fe site
 14 indicates that atomic disorder in the superconducting Fe layer ostensibly does not suppress
 15 superconductivity, contrary to the behaviors of layered cuprate high- T_c superconductors

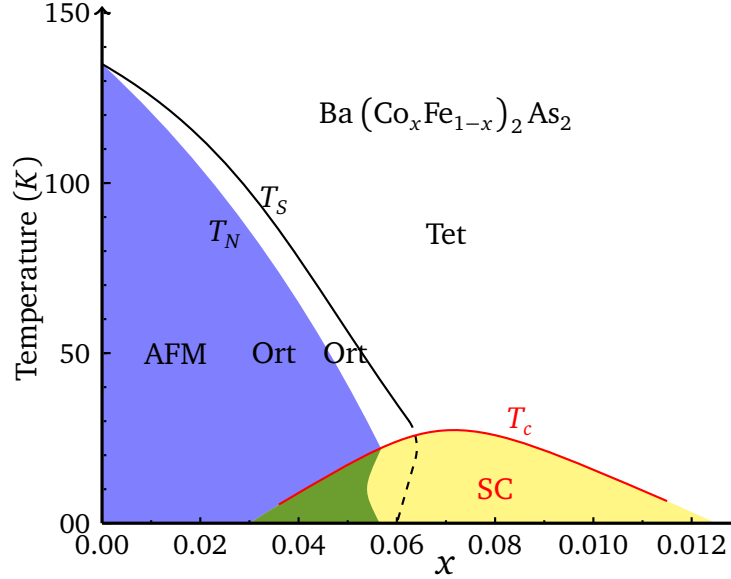


Figure 1.10: Phase diagram [77, 78] for $\text{BaCo}_x\text{Fe}_{2-x}\text{As}_2$. Yellow indicates the superconducting phase, which appears below the superconducting transition temperature T_c . A structural transition occurs at T_s from the tetragonal phase (Tet) at higher temperature to the orthorhombic phase (Ort). Blue represents the antiferromagnetic order (AFM), which appears at T_N , slightly below T_s . The stripes of enhanced superfluid density are observed only in the regime $0.04 < x < 0.06$.

1 where doping onto the Cu sublattice is always detrimental to T_c .
2 A preliminary phase diagram [77, 78] of pnictide superconductors is shown in the
3 figure 1.10. It may be noted that parent compound of superconducting iron arsenides exhibit
4 spin density wave (SDW)-type long-range magnetic ordering at low temperatures [68, 79]
5 just like the cuprates [32]. As it appears that in high- T_c superconductivity, AF order needs
6 to be suppressed before superconductivity may appear, leads many to the proposition that
7 dynamic rather than static antiferromagnetism (or AF fluctuations) is favorable for high- T_c
8 superconductivity. A recent neutron-scattering experiment found that, in $\text{BaFe}_{1.85}\text{Co}_{0.15}\text{As}_2$,
9 the AF fluctuation is as strong as that of $\text{YBa}_2\text{Cu}_3\text{O}_{6+x}$ [80] and electron-phonon coupling
10 is not the primary driver of superconductivity in pnictides. Origin of antiferromagnetic
11 ordering in the pnictide parent compounds is a hotly debated topic, largely owing to its
12 implications for the pairing mechanism: the electronic structure suggests that the same
13 magnetic interactions that drive the AFM ordering also produce the pairing interaction for
14 superconductivity [81]. Regardless of the exact nature of magnetic order, it is believed
15 that magnetostructural coupling is prevalent throughout the Fe-based superconductors in
16 the form of coupled magnetic and structural transitions [82, 83]. Competing presence of
17 superconductivity and AF spin fluctuations has led to suggestions that quantum criticality

1 may play an important role [84–86], however, prominence of quantum critical behavior in
 2 iron pnictides is disputed elsewhere [87]. Due to the large number of pnictides and the
 3 nature of chemical substitution, one limitation so far is that many experiments have been
 4 carried out on different systems or different chemical compositions of the same crystalline
 5 system, and thus make comparisons difficult. However their generic features enables
 6 general conclusions to be drawn from several experiments. For instance, NMR experiments
 7 determined from Knight shift measurements that the superconducting state spin symmetry
 8 is probably singlet [88–90], suggesting an even order parameter symmetry (eg. *s* wave, *d*
 9 wave).

11.4 Pairing Symmetry And Magnetic Penetration Depth Measurement

11 One fundamental quantity in characterization of superconductors is London penetration
 12 depth λ , which is closely related to superfluid density ($\rho_s \equiv \frac{1}{\lambda^2} \propto \frac{n_s}{m^*}$). In general, the
 13 penetration depth λ is given as a function of n_s , effective mass m^* , Ginzburg-Landau
 14 coherence length ξ and the mean free path l as [91]

$$\frac{1}{\lambda^2} = \frac{4\pi n_s e^2}{m^* c^2} \times \frac{1}{1 + \xi/l} \quad (1.3)$$

15 Close to the clean limit, $\frac{\xi}{l} \rightarrow 0$ and the second term in (1.3) becomes unity. λ 's variation
 16 as a function of temperature, doping and orientation are of central importance in testing
 17 microscopic theories of exotic superconductors. For example, the linear variation of $1/\lambda^2$
 18 with respect to temperature was a key finding confirming the *d*-wave nature of the pairing
 19 in $\text{YBa}_2\text{Cu}_3\text{O}_{6+x}$ [92, 93]. Also, early μSR studies of the vortex phase in polycrystalline
 20 samples found a linear correlation between $1/\lambda^2$ and T_c in the under-doped region [94, 95].
 21 The resulting Uemura plot has played a prominent role in theoretical efforts to understand
 22 high T_c superconductivity [96]. Departure from Uemura scaling and the decline of the slope
 23 as the $T_c = 0$ quantum critical point is approached can be understood in terms of a 3D-QCP
 24 model [97]. Scaling of T_c with $n_s(0)$ in underdoped cuprates may also be due to quantum
 25 fluctuations near a 2D quantum critical point [98].

26 It is widely believed that cuprate high- T_c superconductivity originates in two-dimensional
 27 CuO_2 layers [34, 35, 99]. $\text{YBa}_2\text{Cu}_3\text{O}_{6+x}$ also has one dimensional (1D) CuO chains which
 28 contribute to superconductivity the mechanism for which is not fully understood [100].
 29 CuO chains are believed to act as quasi-1D system and charge reservoir [19]. Magnetic
 30 ordering of Cu moments have been observed to be at different temperatures in plane and
 31 chain layers [101]. Penetration depth anisotropy measurements indicate that chains become
 32 superconducting at the same temperature as CuO_2 planes [102]. Due to differences in
 33 band structures between planes and chains [103], one natural explanation for the same
 34 transition temperature is proximity effect [104–106] where by electron hopping between

1 chains and planes contribute to superfluidity along chain direction. The 1D nature of
2 the chains themselves induces, in the filled chain compound, $a - b$ anisotropy which has
3 been observed in dc resistivity [107, 108] and optical conductivity and penetration depth
4 measurements [102, 109] and is expected to affect the vortex core structure [104]. In
5 this simple model of multiband superconductivity in $\text{YBa}_2\text{Cu}_3\text{O}_{7-\delta}$, there is an intrinsic
6 pairing interaction in the plane, but the chains are intrinsically normal, which means that
7 the superconducting order parameter is nonzero in the plane layer only [104]. The pairing
8 mechanism of $\text{YBa}_2\text{Cu}_3\text{O}_{6+x}$ is thought to be predominantly d -wave type. Other possible
9 pairing states involving complicated gap functions, have been suggested [110–113]. Recently
10 discovered BaFe_2As_2 family of superconductors has yet to have a definitive pairing symmetry.
11 An accurate determination of $\lambda(T)$ is one way to probe the symmetry of the pairing state.
12 It has been theorized [114] that only low temperature dependence of $\lambda(T)$ is sensitive to
13 pairing state of the superconductor. It is clear that accurate measurements of λ and $a - b$
14 anisotropy are essential in clarifying central questions in $\text{YBa}_2\text{Cu}_3\text{O}_{6+x}$.

15 Unfortunately, accurate measurements of λ are difficult due to systematic uncertainties.
16 For example, in any bulk measurement the assumption of an exponential decay of the
17 field in the Meissner state is only valid in the local London limit of a perfect surface [115].
18 Significant non-local effects are expected if the coherence length is comparable to the
19 penetration depth [116] or if there are nodes in the superconducting gap function [117].
20 Even within the London limit, there may be a non-exponential decay of the field, arising from
21 any depth dependent change in the magnitude or symmetry of the order parameter. These
22 add uncertainty to all conventional bulk measurements where the field profile is assumed
23 and not measured. Alternatively, one can determine the absolute value of λ from μSR studies
24 in the vortex state where the muon acts as a sensitive probe of the local magnetic field
25 distribution. However, an accurate determination of λ requires there to be a well ordered
26 vortex lattice with known symmetry. Also, there are substantial non-local and non-linear
27 effects associated with vortices which complicate the theory and make it difficult to extract
28 the true λ [117–120]. One approach is to fit the observed field distribution to a simple
29 Ginzburg-Landau model involving an effective λ and then to extrapolate to zero magnetic
30 field (or vortex density) [121]. Until now, the penetration depth has been measured in the
31 vortex state via muon spin rotation [122] and using microwave techniques [92, 123–125].
32 In vortex state measurement, Sonier *et al.* used a GL model for magnetic field distribution
33 to extract λ as a function of applied magnetic field. However, it was mentioned that λ_{ab}
34 measured is an effective penetration depth which is model dependent. Consequently, one
35 may expect some difference in λ measured in the Meissner state where there are no vortices.
36 The microwave techniques used in [92, 123–125] reported London penetration depth for a
37 number of high- T_c superconductors. Microwave techniques are well-suited to measuring
38 temperature dependence of λ but generally not very sensitive to the absolute value of λ .

1 In this thesis, a reduction of magnetic field $B(z)$ is measured as it enters the sample,
2 via the reduction of muon spin precession frequency. The precession frequency contains all
3 the information about muons' interaction with the local magnetic environment. Using a
4 modified London model in the Meissner state, absolute value of magnetic penetration depths
5 are obtained for three oxygen dopings of YBCO and a Co doped FE-PNICTIDE.

1

2 Theory

2.1 BCS Theory

4 The basic idea for BCS superconductivity is that an attractive interaction between electrons,
 5 regardless of their strength, can bind the electrons into pairs [10]. We consider a case for
 6 only two electrons added to the Fermi sea. The first electron attracts positive ions and these
 7 ions, in turn, attract the second electron giving rise to an effective attractive interaction
 8 between electrons. Due to the movement of ion cores, phonon waves are generated and
 9 the interaction between electrons is thereby phonon mediated. The total energy of the
 10 electron system is minimized when there are Cooper pairs compared to a Fermi gas with no
 11 correlation. The center of mass of a Cooper pair is zero since the electrons have opposite
 12 momenta and spin $|\hbar\vec{k}, \uparrow\rangle$ and $|\hbar\vec{k}, \downarrow\rangle$. Due to this opposite momenta and spin, it is
 13 labeled *s*-wave pairing since the relative angular momenta of the two electrons is zero. The
 14 electron-phonon system is described by the single order parameter ψ . An schematic of
 15 “in-phase” motion of the system is shown in the figure 2.1

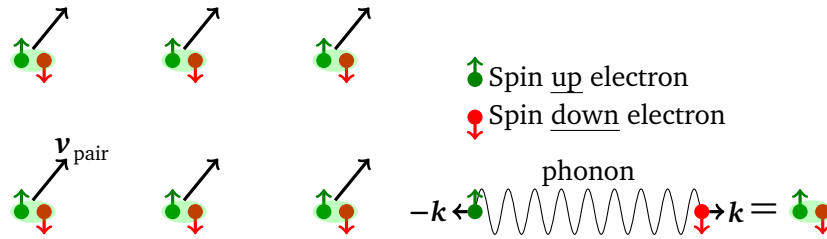


Figure 2.1: In the superconducting state, electrons pair up in zero-spin composites. They all move “in phase” and are said to be “coherent”. This is considered to be a ordered state and the whole electron-phonon system may be described by a single wavefunction.

16 One important consequence of the BCS theory is that the presence of a momentum
 17 dependent energy gap $\Delta(k)$ at the Fermi surface so that an amount of $2\Delta(k, T)$ energy is
 18 required to break a Cooper pair. The energy gap is schematically shown in the figure 2.3.
 19 The gap is opened at the Fermi energy as the temperature is lowered below the critical
 20 temperature. A *d*-wave density of state is also shown in the figure 2.3. Unlike the *s*-wave
 21 superconductors, some carriers are always available at the Fermi surface even at the lowest
 22 temperatures. In the weak coupling limit, where the gap Δ is much smaller than the

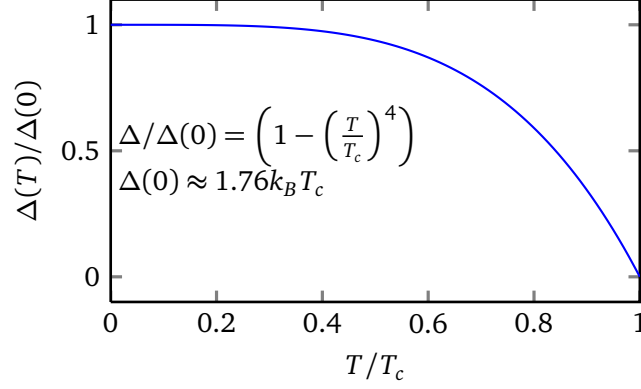


Figure 2.2: Temperature dependence of the superconducting energy gap in the weak coupling limit of BCS interaction. The superfluid density $n_s \propto$ in a two-fluid model [126] implies the (T/T_c) dependence of energy gap. This gap model is also experimentally verified [127].

1 characteristic phonon energy $\hbar\omega_D$,

$$\frac{2\Delta(0)}{k_B T_c} = 3.52. \quad (2.1)$$

2 The numerical factor 3.52 is well tested in experiments and found to be reasonable, in
 3 purely BCS type interactions. $\Delta(T)$ remains fairly constant until the phonon energy becomes
 4 enough to thermally excite the quasiparticles. Near the transition temperature T_c , $\Delta(T)$
 5 varies as

$$\frac{\Delta(T)}{\Delta(0)} \sim 1.74 \left(1 - \frac{T}{T_c}\right)^{\frac{1}{2}}, \quad T \sim T_c \quad (2.2)$$

6 and is graphically shown in the figure 2.2.

7 The most important manifestation of the electron-phonon interaction is the super-
 8 conducting state itself. According to our present understanding of Cooper pairing, the
 9 electron-phonon induced attraction between two electrons would not overcome their direct
 10 Coulomb repulsion, except for the fact that the former is retarded whereas the latter is not.
 11 This gives rise to the pseudopotential effect; in some sense the pseudopotential effect is the
 12 true mechanism of superconductivity, rather than the electron phonon interaction per se.

2.2 London Penetration Depth

14 We consider the penetration depth in the Meissner state of a type II superconductor. Below
 15 H_{c1} , the London equations provide a good description of the electromagnetic properties.
 16 The relevant Maxwell's equation is

$$\vec{\nabla} \times \vec{E} = -\frac{1}{c} \frac{\partial \vec{B}}{\partial t}. \quad (2.3)$$

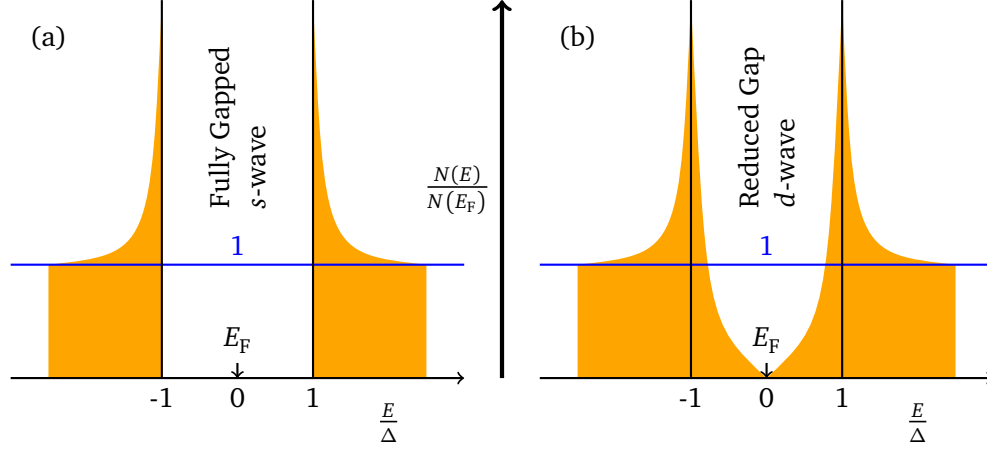


Figure 2.3: Left (*s*-wave): Density of states in a conventional superconductor such as Nb. The density of states is a measurement of how many electrons can reside at a specific energy level. In the figure, there is a region at the Fermi surface where no electrons can reside. This region comprises the superconducting energy gap. On either sides of this gap there are peaks in the density of states where large numbers of electrons can occupy the energy levels. Right (*d*-wave): Density of states in a high- T_c superconductor like YBCO. The density of states is reduced at the Fermi surface, however there is no true gap.

1 In the classical Drude model of electrical conductivity, we have

$$\vec{F} = -m \frac{d\vec{v}}{dt} - e\vec{E} = m \frac{d\vec{v}}{dt}, \quad (2.4)$$

2 where \vec{v} is the average velocity of the electrons, m is the mass of an electron, \vec{E} is the
 3 electric field the electrons are in and τ is the relaxation time, i.e, roughly the time required
 4 to bring the drift velocity to zero if electric field was suddenly set to zero. In a normal metal,
 5 the competition between the scattering and the acceleration in (2.4) leads to a steady state
 6 average velocity

$$\vec{v} = \frac{e\vec{E}\tau}{m}. \quad (2.5)$$

7 Assuming n conduction electrons per unit volume, we get the electric current density via
 8 Ohm's Law,

$$\vec{J} = ne\vec{v} = \left(\frac{ne^2\tau}{m} \right) \vec{E} = \sigma \vec{E}. \quad (2.6)$$

9 To describe superconductivity, London assumed that a certain fraction of electron density n_s
 10 experience no relaxation i.e., letting τ_s in (2.4) go to infinity. This leads to

$$\frac{d\vec{J}_s}{dt} = \left(\frac{n_s e^2}{m} \right) \vec{E}, \quad (2.7)$$

1 where n_s is density of the superconducting carriers. Taking curl on both side of the (2.7),
 2 we get

$$\frac{m}{n_s e^2} \left(\vec{\nabla} \times \frac{d\vec{J}_s}{dt} \right) = \vec{\nabla} \times \vec{E}. \quad (2.8)$$

3 Substituting Maxwell (2.3) in (2.8), we obtain the second London equation

$$\frac{mc}{n_s e^2} \left(\vec{\nabla} \times \frac{d\vec{J}_s}{dt} \right) + \frac{d\vec{B}}{dt} = 0. \quad (2.9)$$

4 Interchanging the order of differentiation with respect to space and time in (2.9), London
 5 postulated

$$\frac{mc}{n_s e^2} (\vec{\nabla} \times \vec{J}_s) + \vec{B} = 0. \quad (2.10)$$

6 Assuming no time varying electric field, another Maxwell equation connects \vec{J}_s with \vec{B} with
 7 the equation

$$\vec{J}_s = \frac{c}{4\pi} (\vec{\nabla} \times \vec{B}) \quad (2.11)$$

Substituting (2.11) into (2.10), we get

$$\begin{aligned} \lambda^2 (\vec{\nabla} \times \vec{\nabla} \times \vec{B}) + \vec{B} &= 0, \\ \lambda^2 \nabla^2 \vec{B} + \vec{B} &= 0, \end{aligned} \quad (2.12)$$

8 where

$$\frac{1}{\lambda^2} = \frac{4\pi n_s e^2}{mc^2}. \quad (2.13)$$

9 In a vacuum-superconductor interface (which is also the case in our experiment), the solution
 10 of (2.12) is given by

$$B(x) = B_0 \exp\left(-\frac{x}{\lambda}\right) \quad (2.14)$$

11 where B_0 is the magnitude of the external applied field. The quantity λ is known as London
 12 penetration depth and $\lambda^{-2} \propto n_s$. The most important success of the London (2.11) and
 13 (2.12) is that a static magnetic field is screened from the interior of a bulk superconductor
 14 over a characteristic penetration depth λ . A simple estimate shows that this distance is a
 15 macroscopical one that is much larger than the mean distance r between electrons in the
 16 superconductor. As one approaches the critical temperature T_c , $n_s \rightarrow 0$ continuously and
 17 as a consequence, $\lambda(T)$ diverges as $T \rightarrow T_c$, according to (2.13). While the (2.14) may be
 18 valid for a superconductor with an atomically flat surface, a rough surface might give rise
 19 to a suppressed order parameter for few tens of nanometers and a modified London model

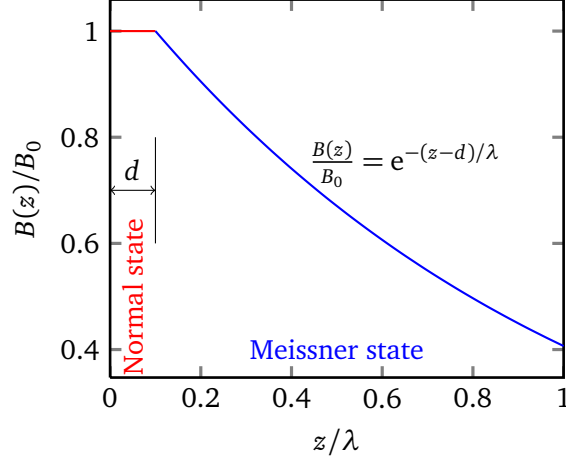


Figure 2.4: External magnetic field drops exponentially ((2.15)) as it enters a superconductor in Meissner state. The characteristic distance λ is called the London penetration depth

1 (figure 2.4)

$$B(z) = \begin{cases} B_0 \exp\left(-\frac{z-d}{\lambda}\right) & \text{if } z \geq d \\ B_0 & \text{if } z < d \end{cases} \quad (2.15)$$

2 may be more appropriate. Here B_0 is the magnitude of the applied field, $\lambda_{a,b}$ is the magnetic
 3 penetration depth in the a or b direction, respectively, z is the depth into the crystal, and d
 4 is an effective dead layer inside of which the supercurrent density is suppressed.

2.3 Pairing Mechanism And Order parameter symmetry

The critical temperature T_c is the onset of long-range, macroscopic phase coherence in the Cooper pairs. Long range correlations between pairs are described by off-diagonal long-range order (ODLRO) [128, 129], with no classical analog, which implies non-zero value of the the pair correlation function

$$\begin{aligned} \rho(\vec{r}, \vec{r}') &= \langle \psi_{\downarrow}^{\dagger}(\vec{r}) \psi_{\uparrow}^{\dagger}(\vec{r}) \psi_{\downarrow}(\vec{r}') \psi_{\uparrow}(\vec{r}') \rangle \\ &= \langle \psi_{\downarrow}^{\dagger}(\vec{r}) \psi_{\uparrow}^{\dagger}(\vec{r}) \rangle \langle \psi_{\downarrow}(\vec{r}') \psi_{\uparrow}(\vec{r}') \rangle \end{aligned} \quad (2.16)$$

6 in the limit the pair separation $|\vec{r} - \vec{r}'|$ is infinite. Here, $\psi_{\uparrow}^{\dagger}(\vec{r})$ and $\psi_{\uparrow}(\vec{r})$ are the particle
 7 field operators ¹ for creation and annihilation at a coordinate \vec{r} , with spin $\vec{k} \uparrow$ From the
 8 finite value of the pair correlation function ((2.16)), the local pair amplitude $\langle \psi_{\downarrow}^{\dagger}(\vec{r}) \psi_{\uparrow}^{\dagger}(\vec{r}) \rangle$
 9 must be non-zero, which is, in essence the amplitude squared of the GL order parameter,
 10 $|\psi(\vec{r})|^2 \propto n_s$, the superfluid density. It's important to note that, although n_s is “local pair”

¹ $\psi_{\uparrow}(\vec{r}) = \langle \psi | \psi_{\uparrow}(\vec{r}) | \psi \rangle$ is the real space representation, where $|\psi\rangle$ is the ground state wavefunction.

1 amplitude, pairings are non-local, ie, partners of a single pair are in macroscopic distance.
 2 With macroscopic ODLRO in effect, it's possible to derive Meissner effect [128, 130], flux
 3 quantization [128]. It has been argued that that ODLRO is a property not only of BCS
 4 superconductors but also of high- T_c superconductivity [130, 131] and of recently discovered
 5 superconductivity of Pnictide [132].

6 As in any appearance of order, superconducting order also reduces available symmetry
 7 of the system. In case of 2nd order, continuous, superconducting transition, order parameter
 8 is a measure of the amount of symmetry breaking in the ordered state. Symmetry group
 9 H describing the superconducting state must be a subgroup of the normal state symmetry
 10 group G :

$$G = X \times R \times U(1) \times T \quad \text{for } T > T_c \quad (2.17)$$

11 and

$$H \subset G \quad \text{for } T < T_c \quad (2.18)$$

12 where X is the symmetry group of the crystal lattice, R the symmetry group of spin rotation,
 13 $U(1)$ the one dimensional global gauge symmetry, and T the time reversal symmetry
 14 operation. Nearly all group-theoretic classifications of superconducting states are based on
 15 point-group symmetry. Point-group symmetry classification of pair states has been extensively
 16 studied in cuprate superconductors [133–135].

17 Order parameter symmetry can give insight into the mechanism/nature of pair conden-
 18 sate and limit the possible interactions that are possible. Crystal structures that have mirror
 19 symmetry (eg, CuO_2 layer based superconductors) can be described by parity of the the pair
 20 state. It has been argued that the complex phase diagram of high- T_c superconductors can be
 21 deduced from a symmetry principle that unifies antiferromagnetism and order parameter
 22 symmetry [136].

The superconducting energy gap $\Delta(\vec{k}, T)$ for s -wave superconductors, are believed to
 symmetric in momentum space (figure 2.5a). One other very important pairing symmetry is
 of d -wave where the energy gap is thought to be of the form

$$\begin{aligned} \Delta(\vec{k}_F, T) &= \Delta_0(\cos k_x - \cos k_y) \\ &\approx \frac{\Delta_0}{2}(k_x^2 - k_y^2), \text{ along the nodes, } k_x, k_y \text{ small} \end{aligned} \quad (2.19)$$

23 where momentum \vec{k}_F is measured from the Fermi surface. It may be noted that for $|\hat{k}_x| = |\hat{k}_y|$,
 24 the gap is zero (figure 2.5b) meaning thermal excitations can easily destroy superconducting
 25 carriers. High- T_c superconductor family of YBCO are believed to be primarily of d -wave
 26 [137–139]. Establishment of predominantly d -wave order in T_c materials, over a wide
 27 range of doping and temperature range, entails the idea that d -wave symmetry is robust.
 28 This also suggests that d -wave pairing in cuprates has a common origin. Newly discovered

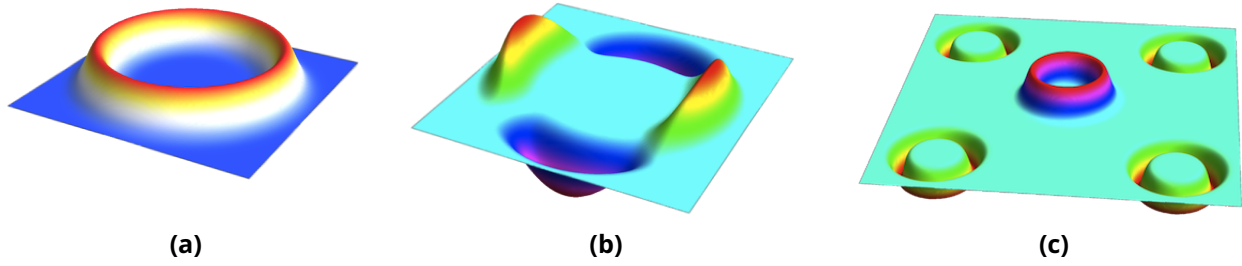


Figure 2.5: A schematic representation of the superconducting order parameter in different cases: (a) a conventional, s wave superconductor (eg. Nb); (b) a d wave, as is the case in copper oxides; (c) an s_{\pm} wave, as is thought to be the case in iron-based superconductors. In (a) and (b), the two-dimensional Fermi surface is approximated by one circle. In (c), the Fermi surface is approximated by a small circle in the center (the first band) surrounded by four larger circles (to comply with the tetragonal symmetry [140]; the second band). In all cases, the height of the “rubber sheet” is proportional to the magnitude of the order parameter (including its sign).

- 1 family of FE-PNICTIDE superconductors are suggested to have s_{\pm} (figure 2.5c) symmetry of
- 2 order parameter from band structure calculations [81, 141]. Although a superconducting
- 3 mechanism isn't determined by the order parameter, the pairing hamiltonian must obey the
- 4 point-group symmetry of the gap function $\Delta(\vec{k})$.

2 Experimental Techniques

3.1 Introduction To μ SR

4 Muons were discovered in the 1930's and their properties learned in the 1940's and were
 5 used as probes of magnetism in matter [Rasetti, 1944]. μ SR/ $M\mu$ SR refers to muon Spin
 6 [Rotation/Relaxation/Resonance](#) techniques which uses anisotropic decay of almost 100%
 7 spin-polarized muons to investigate local magnetic environment of matter, both in bulk and
 8 in thin films. This is significant improvement on other magnetic resonance probes such
 9 as nuclear magnetic resonance (NMR) and electron spin resonance (ESR) methods that
 10 must rely upon thermal equilibrium spin polarization in a magnetic field so that sufficient
 11 polarization is often achieved only at low temperatures and/or in strong magnetic fields.

12 When a muon(μ^+ , solely used in our experiments) decays, it emits a fast decay positron
 13 preferentially along the direction of its spin due to the parity violation. From a single decay
 14 positron one cannot be certain which direction the muon spin is pointing in the sample.
 15 However, by measuring the anisotropic distribution of the decay positrons from a large
 16 number of muons deposited at the same conditions, the statistical average direction of
 17 the spin polarization of the muon ensemble can be determined. The time evolution of the
 18 muon spin polarization depends very sensitively on the spatial distribution and dynamical
 19 fluctuations of the muons' magnetic environment.

3.1.1 Properties And Production Of Muons

Muons are leptons, 207 times more massive than electrons. Muon properties are briefly mentioned in the following table 3.1. Muons are generated from the decay of charged pions (π^\pm), produced via collision of high-energy protons with target nuclei, such as carbon or beryllium. The charged pions that are produced live for only about 26 ns and then decay into a muon and muon neutrino (antineutrino), as schematically shown in figure 3.1;



Negative pions in targets behaves as heavy electrons and are captured by nucleus instead of decaying to negative muons. Positive pions do, however, are repelled by nuclei and take up interstitial positions in target atoms and subsequently decay into positive muon and

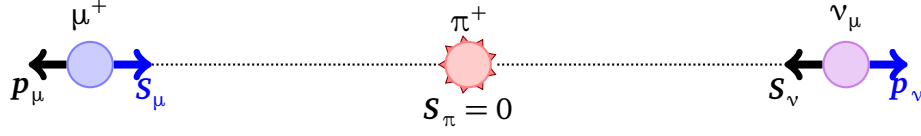


Figure 3.1: Positively charged pions live for about 26 ns and then decay into muon and a neutrino. The muons are almost 100% spin-polarized and their spins are opposite to their momentum. The muons carry a kinetic energy of 4.12 MeV in the rest frame of pion. These muons are referred to as “surface muons” as they originate from pions decaying near the surface of the production target.

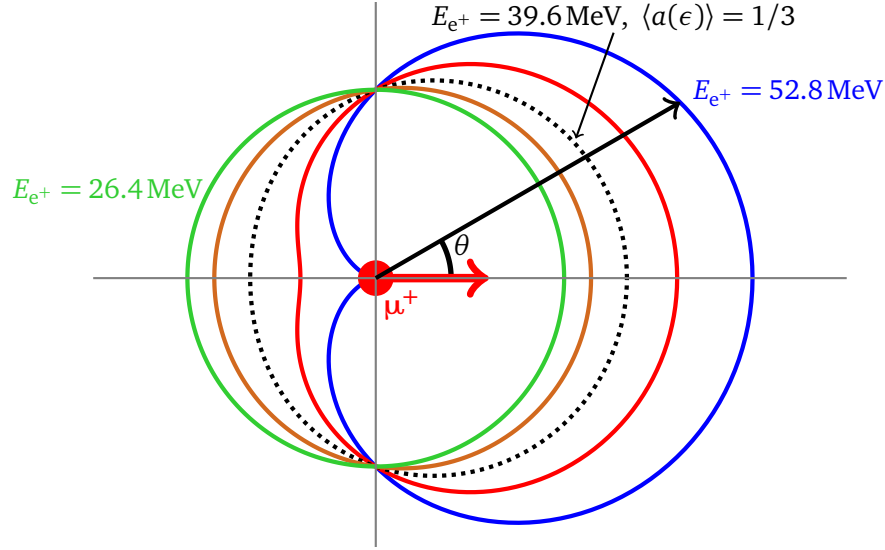


Figure 3.2: Angular probability distribution ($K(\epsilon, \theta)$, between 26.4 MeV and 52.8 MeV) of positrons emitted from muons with polarization along the red arrow direction is shown. The maximum average asymmetry for such a β -decay process is 1/3 (the dotted curve).

a neutrino. For this reason, only positive muons are used to investigate local magnetic environments in materials. Because of the parity violating nature of weak beta-decay, the positron in a μ^+ decay is correlated with direction of muon spin at that instant. Ensemble average polarization may be determined from the decay asymmetry of emitted positrons. The highly relativistic positron's probability per unit time, in decaying at an angle θ with respect to the μ^+ spin polarization is given by

$$\frac{dW(\epsilon, \theta)}{dt} = \frac{e^{-t/\tau_\mu}}{\tau_\mu} [1 + a(\epsilon) \cos(\theta)] n(\epsilon) d\epsilon d(\cos(\theta)) \quad (3.2a)$$

$$\equiv \frac{e^{-t/\tau_\mu}}{\tau_\mu} K(\epsilon, \theta) n(\epsilon) d\epsilon d(\cos(\theta)) \quad (3.2b)$$

¹ where “reduced energy” $\epsilon = E/E_{\max}$, the **asymmetry** $a(\epsilon) = (2\epsilon - 1)/(3 - 2\epsilon)$, energy

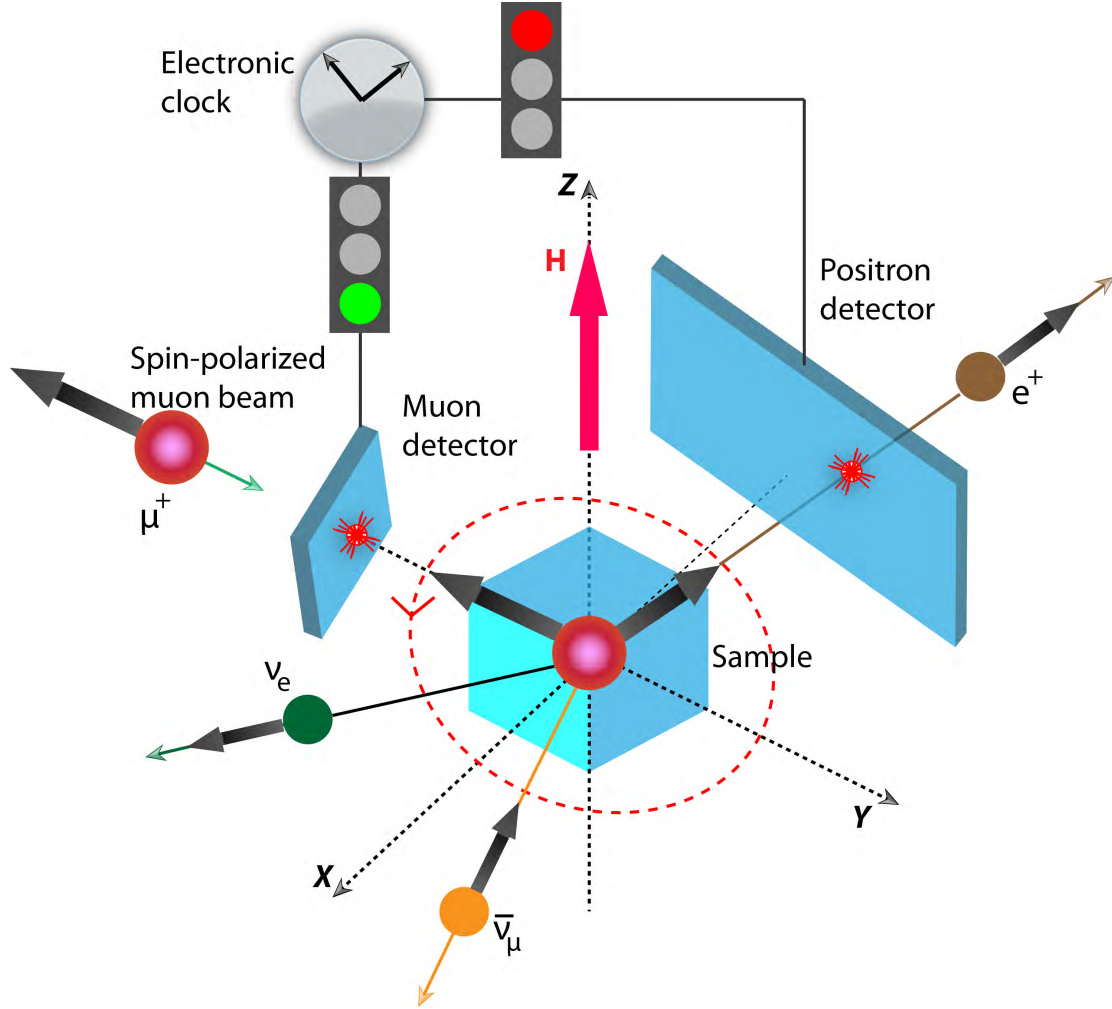


Figure 3.3: Schematic of the arrangement for a TF- μ SR experiment. The muon spin Larmor precesses about the local magnetic field \mathbf{B} at its stopping site in the sample, and subsequently undergoes the three-body decay $\mu^+ \rightarrow e^+ + \nu_e + \bar{\nu}_\mu$. The time evolution of the muon spin polarization is accurately determined by detection of the decay positrons from $\sim 10^6$ muons implanted one at a time.

- 1 density function $n(\epsilon) = 2\epsilon^2(3 - 2\epsilon)$. The maximum positron energy $E_{\max} \simeq 52.8 \text{ MeV}$, about
- 2 half of the muon rest energy. Integrating over energy (ϵ), we get

$$dW(\theta) = \frac{e^{-t/\tau_\mu}}{\tau_\mu} [1 + \langle a(\epsilon) \rangle \cos(\theta)] d(\cos(\theta)) dt \quad (3.3)$$

- 3 where, the average of the asymmetry function is

$$\langle a(\epsilon) \rangle = \int_0^1 a(\epsilon) n(\epsilon) d\epsilon = \frac{1}{3} \quad (3.4)$$

Table 3.1: Properties of Muon [144]

Mass, m_μ	105.658389(34) MeV/ c^2
Lifetime, τ_μ	2.197034(21) μ s
Charge, q	$\pm e$
Spin	$\frac{\hbar}{2}$
Magnetic moment	$4.49044786(16) \times 10^{-26}$ J/T
Spin g-factor, g_μ	2.0023318414(12)
Gyromagnetic ratio, $\gamma_\mu = g_\mu \mu_\mu / \hbar$	$2\pi \times 135.696\,82(5)$ MHz T $^{-1}$

1 The probability function $K(\epsilon, \theta)$ as a function of polar angle θ is plotted in figure 3.2
2 for reduced energy values of $\epsilon = 0.5, 0.625, 0.75, 0.875$ and 1.0 . For an ensemble of
3 muons, the maximum theoretical β -decay asymmetry is therefore $1/3$. The asymmetry is
4 determined in our experiments in a **transverse field (TF- μ SR)** arrangement as shown in
5 figure 3.3. **TF- μ SR** refers to the case of incoming muon polarization being perpendicular to
6 the external field direction For more details of muon production the reader is referred to
7 these references [142, 143].

3.1.2 General μ SR Techniques

9 Detailed accounts of techniques may be found in the following references: the book of
10 Schenck [145], the review article of Cox [146] & of H. Keller [147]. For general technical
11 and statistical details, readers may consult these theses: Riseman [142], Chow [148] and
12 Luke [149]. While conventional surface muon beams can be used to investigate rather small
13 samples, there is a desire for still lower energy muons that can be stopped near sample
14 surfaces (for example to determine depth dependent magnetic field), in thin films and near
15 multi-layer interfaces (to determine exotic magnetic phenomenon). A number of innovative
16 methods have been used in attempts to produce **ultra slow** muon beams. The results in
17 this thesis were obtained using one such method employing ultra slow muons as probe,
18 described in the next section.

3.2 Low Energy μ SR

20 The experiments detailed in this thesis were done in the low energy (≤ 30 keV) **LEM- μ SR**
21 beamline (μ E4 [150]) in Paul Scherrer Institut (PSI). LEM group has developed a technique
22 of slowing down a surface muon beam of 4 MeV and 100% polarization to a beam of low
23 energy (0-30 keV), polarized muons. Figure 3.4 shows the schematic low energy beamline
24 μ E4. The 4 MeV beam passes through a **moderator** consisting of a thin layer (~ 100 nm) of
25 rare gas solid or solid nitrogen deposited on 125 μ m silver substrate. A very small fraction
26 of the muons escape the moderator with a mean energy about 15 eV with an energy spread
27 (FWHM) of ~ 20 eV. The dominant fraction of the beam exits the moderator target as **fast**
28 (degraded but not moderated) muons with a mean energy of 500 keV and a FWHM of the

1 same order. These fast muons are separated from the slow ones by a 90 degree deflection
 2 by an electrostatic mirror. This deflection, of slow muons, necessarily changes momentum
 3 direction of muons while keeping the spin direction unaltered. After deflection, muon
 4 spin and momentum directions are perpendicular. Fast muons are little affected by the
 5 electrostatic mirror and are monitored by multi channel plate[MCP] detector. The **low**
 6 **energy muons** are clearly identified by a time-of-flight (TOF) measurement between the
 7 start scintillator and the **trigger detector**. The trigger detector, made of an ultra-thin carbon
 8 foil ($2.2 \mu\text{g cm}^{-2}$), is used to set **time-zero**, t_0 for the incoming low energy muons. The
 9 muons traversing the foil emit a few electrons, which are deflected by 90 degrees and
 10 detected by a MCP to give the start signal for the μSR measurement. Trigger detector causes
 11 an energy loss of the muons $\sim 1.6 \text{ keV}$ with a Gaussian energy spread $\sim 500 \text{ eV}$. Detection
 12 efficiency of trigger detector is $\sim 80\%$. After passing trigger detector, the μ^+ beam is focused
 13 on the sample by an einzel lens (L3) and a conically shaped electrostatic lens.

14 The sample and it's Ni-coated¹ Al holder are electrically insulated by a thick sapphire
 15 crystal and can be biased -12.5 keV to $+12.5 \text{ keV}$. Sapphire crystal also provides a good
 16 thermal contact between the cold finger and the sample. The bias voltage, coupled with
 17 the voltage at trigger detector (between 12 and 20 kV), determines the muon energy at
 18 the sample ranging from 0.5 keV to 30 keV . A Helmholtz coil is used to generate external
 19 magnetic field applied to the muons. External magnetic field(B_{ext}) can be applied in two
 20 directions; either parallel to muon momentum direction or perpendicular to it, i.e, parallel to
 21 sample plane (ab). In the first case, muons precess in the sample plane and four scintillator
 22 telescopes (Left, Right, Top and Bottom) are used to count emitted positrons. In the other
 23 case, muon spins precess out of the plane and only left and right positron counters record
 24 positron decays. The experiments detailed in this thesis uses the second scenario where B_{ext}
 25 is parallel to sample plane. Extensive details on low energy muon beamline may be found
 26 elsewhere [151, 152].

3.2.1 Principles Of LE- μSR

28 Positron detectors help accumulating histograms of positron detection events having the
 29 mathematical form

$$N(t) = N_{\text{bg}} + N_0 e^{-t/\tau_\mu} (1 + \mathcal{A}(t)), \quad (3.5)$$

30 where N_0 is the normalization, N_{bg} is a time-independent background and $\mathcal{A}(t)$ is the time
 31 dependent asymmetry for the detector along \hat{n} direction, defined as

$$\mathcal{A}(t) = A_0 \mathcal{P}(t) = A_0 \hat{n} \cdot \mathcal{P}(t) \quad (3.6)$$

¹The sample holder is coated with $\sim 1 \mu\text{m}$ of Ni. Since Ni is ferromagnetic, muons that miss the sample, experience a big hyperfine field and disappears from the frequency window of interest. This very effective background suppression method was the critical step which allows low energy μSR to be applied to crystals much smaller than the beam diameter.

1 where A_0 is directly related to the theoretical maximum **asymmetry** $a(\epsilon)$ referred in (3.4)
 2 Muon polarization $\mathcal{P}(t)$ reflects time-dependent spin-polarization and its modulus defined
 3 as

$$\mathcal{P}(t) = \frac{\langle \mathbf{S}(t) \cdot \mathbf{S}(0) \rangle}{\langle S(0)^2 \rangle} \quad (3.7)$$

where $\mathcal{P}(0) = \pm \hat{n}$. \hat{n} refers to the direction of observation (detector). Experimentally observed asymmetry is lower than the maximum value of 1/3 as the initial spin polarization is less than 1 and emitted positrons are collected in a limited solid angle. Nevertheless, muon asymmetry (polarization) contains all information about muons interaction with the local magnetic environment. Upon entering the sample, the muon spins interact with local magnetic environment and ensemble average spin changes according to the Bloch equation,

$$\frac{d\mathbf{S}}{dt} = \boldsymbol{\mu} \times \mathbf{B} \quad (3.8)$$

where, $\mathbf{B} = \mathbf{B}_{\text{ext}} + \mathbf{B}_{\text{int}}$. $\mathbf{B}_{\text{ext}} \gg \mathbf{B}_{\text{int}}$, for the experiments detailed in this thesis. Without loss of generality, static external magnetic field may be assumed as $\mathbf{B}_{\text{ext}} = B\hat{z}$, yielding

$$\frac{dS_x}{dt} = \gamma S_y B \quad (3.9a)$$

$$\frac{dS_y}{dt} = \gamma S_x B \quad (3.9b)$$

$$\frac{dS_z}{dt} = 0 \quad (3.9c)$$

4 The above equations (3.9a) and (3.9b) are solved by

$$\begin{aligned} S_x(t) &= S(0) \sin(\gamma B t + \varphi) \\ S_y(t) &= S(0) \cos(\gamma B t + \varphi) \end{aligned} \quad (3.10)$$

5 where $S(0)$ and φ are determined by spin direction at $t = 0$.

6 So far, a big external field's effect (precession of polarization) has been discussed. Here
 7 we discuss the effects of (small) internal fields that are present in any sample due to randomly
 8 oriented magnetic moments.

$$\mathcal{P}(t) = \iiint P(\mathbf{B}) \mathcal{P}_B(t) d\mathbf{B} \quad (3.11)$$

9 where \mathbf{B} is the local magnetic field muon experiences, $B = |\mathbf{B}|$, $\mathcal{P}_B(t)$ is the time-dependent
 10 (oscillating) muon polarization and $P(B)$ is the normalized probability distribution of mag-
 11 netic field inside the sample. Inside the sample, randomly oriented magnetic moments can
 12 generate a distribution of magnetic field, at any given muon site, and may be approximated

1 by a three-dimensional Gaussian distribution,

$$P(\mathbf{B}) = \left(\frac{\gamma_\mu}{\sqrt{2\pi}\sigma} \right)^3 \exp \left(-\frac{\gamma_\mu^2 B^2}{2\sigma^2} \right) \quad (3.12)$$

2 For an external field perpendicular to muon spin direction, e.g. $\mathbf{B}_{\text{ext}} = B_{\text{ext}} \hat{\mathbf{x}}$, the Gaussian
3 probability distribution (3.12) is centered around field $\mathbf{B} = (B_{\text{ext}}, 0, 0)$, and has the form

$$P(\mathbf{B}) = \left(\frac{\gamma_\mu}{\sqrt{2\pi}\sigma} \right)^3 \exp \left(-\frac{\gamma_\mu^2 \left((B_x - B_{\text{ext}})^2 + B_y^2 + B_z^2 \right)}{2\sigma^2} \right) \quad (3.13)$$

With $\mathcal{P}(0) \parallel \hat{\mathbf{z}}$, the muon polarization may be written as,

$$\begin{aligned} \mathcal{P}(t) &= \left(\frac{\gamma_\mu}{\sqrt{2\pi}\sigma} \right)^3 \int \int \int \exp \left(-\frac{\gamma_\mu^2 \left((B_x - B_{\text{ext}})^2 + B_y^2 + B_z^2 \right)}{2\sigma^2} \right) \cos(\gamma_\mu B t) d\mathbf{B} \\ &\simeq \frac{\gamma_\mu}{\sqrt{2\pi}\sigma} \int_{B_x=-\infty}^{\infty} \exp \left(-\frac{\gamma_\mu^2 (B_x - B_{\text{ext}})^2}{2\sigma^2} \right) \cos(\gamma_\mu B_x t) dB_x \\ &= \left(\frac{\gamma_\mu}{\sqrt{2\pi}\sigma} \right) \left(\frac{\sqrt{2}\sigma}{\gamma_\mu} \right) \int_{n=-\infty}^{\infty} \exp(-n^2) \cos \left(\gamma_\mu \left(\frac{\sqrt{2}\sigma n}{\gamma_\mu} + B_{\text{ext}} \right) t \right) dn \\ &= \left(\frac{1}{\sqrt{\pi}} \right) \int_{n=-\infty}^{\infty} \exp(-n^2) \cos(\sqrt{2}\sigma t n + \gamma_\mu B_{\text{ext}} t) dn \\ &= \exp \left(-\frac{\sigma^2 t^2}{2} \right) \cos(\gamma_\mu B_{\text{ext}} t) \end{aligned} \quad (3.14)$$

4 As may be seen from (3.14), random moments in a sample give rise to damping in the
5 muon polarization. Additionally, when muons are implanted into a sample with inequivalent
6 magnetic sites (e.g. superconducting state), there will be a distribution ($\rho(B)$), discussed in
7 detail in the following section, of fields ($B(z) \equiv B_{\text{ext}}(z)$) inside the sample & the polarization
8 (3.14) takes the form

$$\mathcal{P}(t) = \exp \left(-\frac{\sigma^2 t^2}{2} \right) \int_0^\infty \rho(z) \cos(\gamma_\mu B(z) t) dz \quad (3.15)$$

9 The asymmetry $\mathcal{A}(t) = A_0 \mathcal{P}(t)$ is fitted to the experimentally observed asymmetries to obtain
10 physical parameters A_0 , σ and d, λ (in Meissner state).

11 An example histogram of raw data, from the **forward** counter and asymmetry $\mathcal{A}(t)$ are
12 given in figure 3.5. In this experiment, a transverse external field of 9.47 mT was applied
13 and the resulting sinusoidal oscillations can be taken into account by the theoretical model in

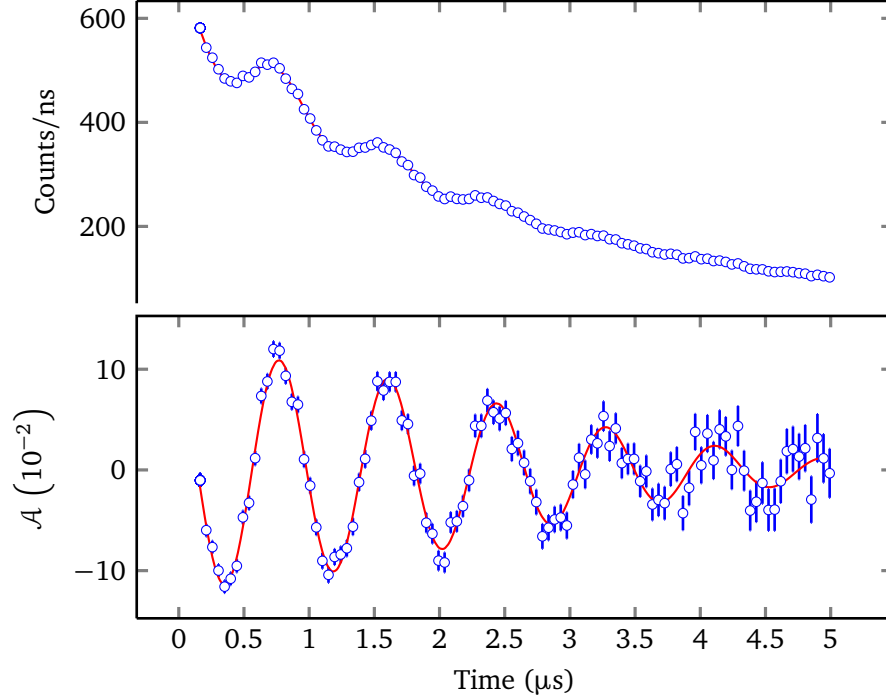


Figure 3.5: Top: A histogram from “forward” positron detector in a time-differential measurement on the sample of $\text{YBa}_2\text{Cu}_3\text{O}_{6.92}$, depicting the exponential decay of the muons and muon precession. Bottom: Larmor precession of muons’ spin magnetic moment may be noticed from the time dependence of asymmetry $\mathcal{A}(t)$, in an external applied field of 94.7G with an implantation energy of 22 KeV, with temperature of 90K.

- 1 (3.15). Probably the most important characteristic of the muon polarization decay spectrum
- 2 is the precession frequency which represents average magnetic field, including local magnetic
- 3 fluctuations, muons experience.

3.2.2 Stopping Distribution

- 5 Even at a specific energy, ions bombarded onto a material, end up at different depths
- 6 due to randomness in the collision process. The energy dependent stopping profiles can
- 7 be generated using “Transport of Ions in Solids” (TRIM) codes introduced by Ziegler *et*
- 8 *al* [153] based on the ideas of Eckstein [154]. The accuracy of TRIM in calculating ion range
- 9 distributions in various materials is well established, and they are routinely used in similar
- 10 depth controlled experiments such as Low-Energy μSR . By specifying the energy, charge, and
- 11 mass of the probe ions (μ^+ in this thesis), and the mass density and atomic numbers of the
- 12 elements of the probed material, one is able to simulate the implantation profile using TRIM.
- 13 Generated energy-dependent profiles of YBCO are shown in figure 3.6. Average depth of
- 14 muons increases with energy and an almost linear relationship ($\langle z_\mu \rangle (E) = 3.26 + 4.37 * E \text{ nm}$)

1 is obtained as shown in figure 3.6. For $\text{Ba}(\text{Co}_{0.074}\text{Fe}_{0.926})_2\text{As}_2$, a different energy dependent
2 linear relationship ($\langle z_\mu \rangle (E) = 4.26 + 4.53 * E \text{ nm}$) is obtained. The stopping profiles are only
3 relevant for the μ^+ ions stopping in the probed material. A majority fraction of incoming
4 μ^+ ions stop at Ni coated sample plate where it quickly depolarizes and do not affect the
5 calculation of penetration depth presented in this thesis. A review of depth resolved studies
6 of materials may be found in [152, 155] and references therein.

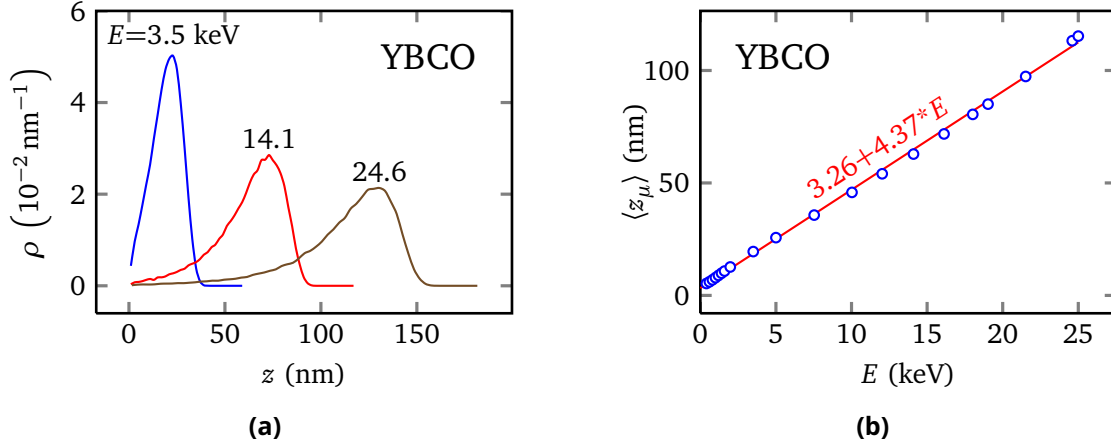


Figure 3.6: Muon implantation profiles in YBCO: Implanted muons stop at differ depths even if the incoming beam energy is the same. By specifying the energy, charge, and mass of the μ^+ ions, and the mass density and atomic numbers of the elements, profiles are simulated via Monte-Carlo algorithm using TRIM.SP. The accuracy of TRIM.SP in calculating ion range distributions in various materials is well established, and they are routinely used in similar depth controlled experiments.

1

2 Results & Analysis

3 In this chapter, measurements of λ and the anisotropies ($\equiv \lambda_a/\lambda_b$) are presented for three dif-
 4 ferent oxygen ($x = 6.52, 6.92, 6.998$) contents of $\text{YBa}_2\text{Cu}_3\text{O}_{6+x}$ and for $\text{Ba}(\text{Co}_{0.07}\text{Fe}_{0.93})_2\text{As}_2$.
 5 The measured values of λ and the anisotropies are considerably different from that of litera-
 6 ture, often found with indirect methods.

7 External magnetic field drops inside a superconductor according to London model,
 8 described in section 2.2, on the length scale of λ . Close to the surface, there may be
 9 deviations from a purely exponential $B(z)$ as conjectured in (2.15). A reduction in magnetic
 10 field can be detected using LE- μ SR as muon precession frequency is proportional to the local
 11 magnetic field. An schematic representation of the fitting procedure to obtain λ and other
 12 parameters are shown in figure 4.1. In the normal state, external field ($\mu_0 H$) penetrates the
 13 sample fully yielding an average muon precession frequency of $(\gamma_\mu \mu_0 H)/2\pi$. A distribution
 14 of the local fields, from randomly oriented nuclear moments (see (3.14)), is approximated
 15 by the broadening parameter σ . In the superconducting state, muon precession frequency
 16 depends on implantation depth (z), for the muons landing between depth z and $z + dz$ and
 17 the time dependent asymmetry may be written as

$$\mathcal{A}(t) = A_0 \exp \left[-\sigma^2 t^2 / 2 \right] \times \int \rho(z) \cos \left[\gamma_\mu B(z, d, \lambda) t + \varphi \right] dz \quad (4.1)$$

18 A slightly modified form (4.2) of the above equation (4.1) is used to fit **all** superconducting
 19 states and to extract parameters $A_0, d, \sigma, \lambda, \varphi$. Average magnetic field $\langle B \rangle$ are computed
 20 from the above mentioned parameters for various externally applied magnetic fields ranging
 21 from 1.5 mT to 10 mT. All measurements in the superconducting state were carried out
 22 under **zero-field-cooled** conditions in order to avoid flux trapping at the surface.

23 The analysis in this chapter are presented chronologically:

- 24 (i) $\text{YBa}_2\text{Cu}_3\text{O}_{6.92}$ i.e YBCO-I, section 4.1.1.
- 25 (ii) $\text{YBa}_2\text{Cu}_3\text{O}_{6.998}$ i.e YBCO-II, section 4.1.2
- 26 (iii) $\text{YBa}_2\text{Cu}_3\text{O}_{6.52}$ i.e YBCO-III, section 4.1.3
- 27 (iv) $\text{Ba}(\text{Co}_{0.07}\text{Fe}_{0.93})_2\text{As}_2$, section 4.2

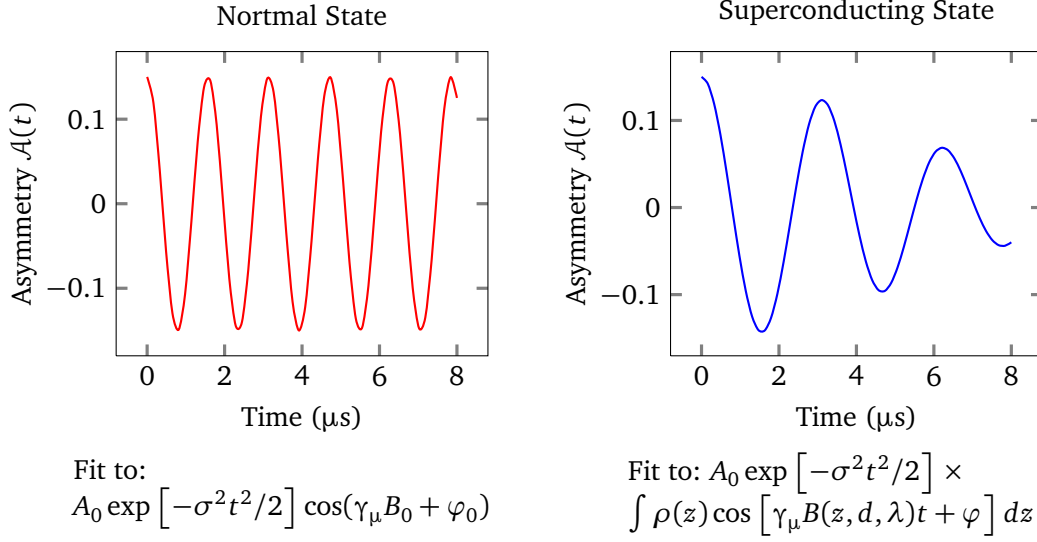


Figure 4.1: Quick outline of the fitting procedure: Left: In the normal state, oscillatory signal in muon polarization is fitted to a cosine function with a Gaussian broadening originating from randomly oriented local internal fields. Right: In the superconducting state, polarization is a sum of frequency ($\gamma_\mu B$) dependent oscillation and an additional broadening σ taking into account expelled flux from neighboring crystals or from any other sources of random fields.

4.1 LE- μ SR experiments on $\text{YBa}_2\text{Cu}_3\text{O}_{6+x}$ single crystals

The LE- μ SR experiments on $\text{YBa}_2\text{Cu}_3\text{O}_{6+x}$ have been conducted on freshly grown single crystals using the self-flux method [156]. The purity of the crystals is the same as for crystals in which quantum oscillations in resistivity have recently been reported [157]. Each of the crystals was approximately rectangular in shape with lateral dimensions in the a - b plane ranging from 1 mm to 3 mm and a thickness in the c -direction ranging from 0.1 mm to 0.3 mm. They were detwinned to a level greater than 95 %. The mounted mosaic of YBCO-II on the coldfinger is shown in the figure 4.2. Two other oxygen doped crystals were mounted in very similar method. The crystal faces were mirror-like in appearance and atomic force microscopy indicates the roughness of the surface to be a few nm (cf. figure 4.3). A UHV compatible Ag epoxy was used to attach each crystal to the sample holder made of high purity Al coated with 1 μm of Ni. Muons that miss the sample stop at the polycrystalline Ni coated sample holder and experience big hyperfine field from Ni moments; thereby quickly depolarizes and disappears from the frequency window of interest. Control experiments on a Ag disc the same size as the sample showed that such a thin layer of Ni has no effect on the precession signal in the sample. The maximum asymmetry A_0 from all these experiments are significantly less than the theoretical maximum 1/3 as decay positrons are collected in a limited solid angle and only $\sim 40\%$ muons land on $\text{YBa}_2\text{Cu}_3\text{O}_{6+x}$ crystals.

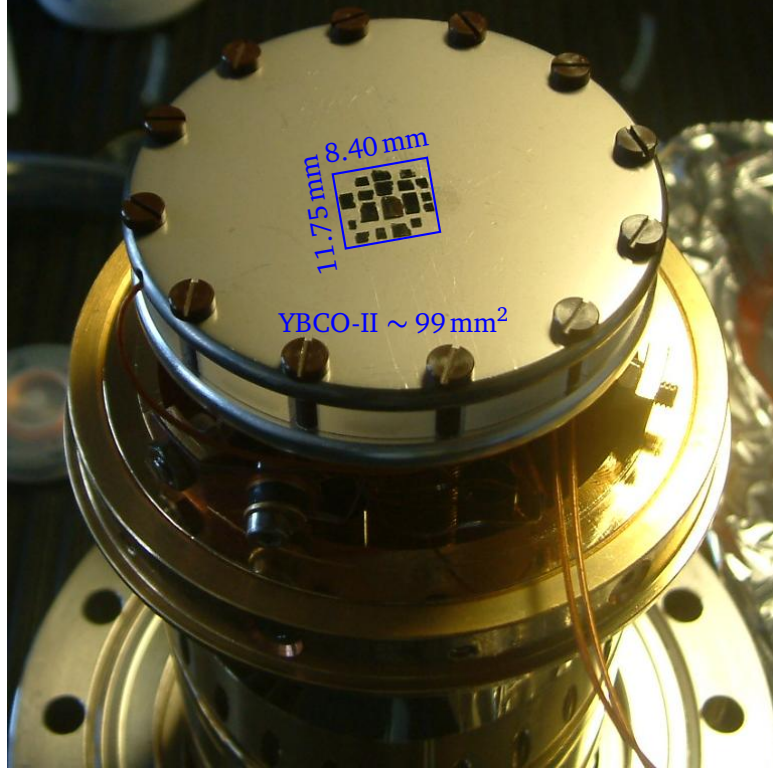


Figure 4.2: YBCO-II Mosaic: The total area of the mosaic is about 99 mm^2 . Each of the crystals was approximately 1 mm to 3 mm in the $a - b$ plane and a c -axis thickness of 0.1 mm to 0.3 mm. An ultra high vacuum compatible Ag epoxy was used to attach each crystal to the sample holder of high purity Al coated with $1 \mu\text{m}$ of Ni.

4.1.1 $\text{YBa}_2\text{Cu}_3\text{O}_{6.92}$

- 2 To analyze superconducting state asymmetry $\mathcal{A}(t)$, slightly modified version of (4.1) is used

$$\mathcal{A}(t) = A_0 \exp\left(-\frac{\sigma^2 t^2}{2}\right) \int \rho(B) \cos\left[\gamma_\mu B(z, d, \lambda)t + \varphi\right] dB, \quad (4.2)$$

- 3 where an integration over field distribution $\rho(B)$ is done instead of an integral over $\rho(z)$.
 4 $\rho(B)$ is defined as

$$\rho(B) = \rho(z) \left| \frac{dB}{dz} \right|^{-1} \quad (4.3)$$

- 5 Although equations (4.1) and (4.2) are mathematically equivalent for the analysis presented
 6 in this thesis, the latter offers a more general approach for analyzing data using models
 7 where a specific field distribution is believed to be present. To take into account any random

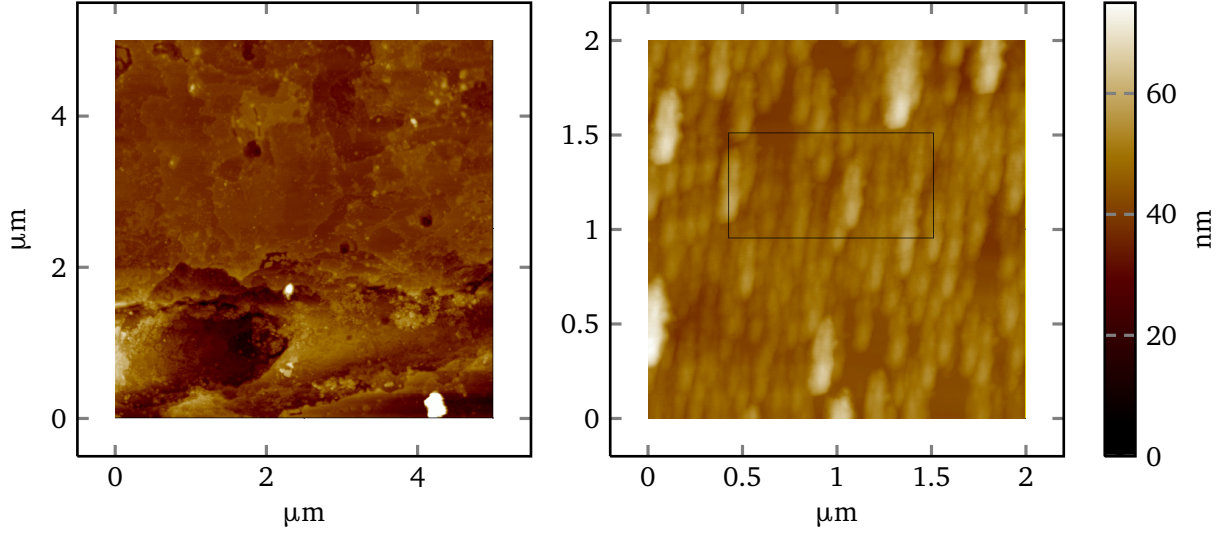


Figure 4.3: YBCO roughness: Left figure shows a $5\mu\text{m}\times 5\mu\text{m}$ area of a YBCO-I crystal being scanned by tapping AFM. Right figure shows another region of a smaller size and even smaller sized box. A 2 nm to 3 nm of average roughness is found from these measurements.

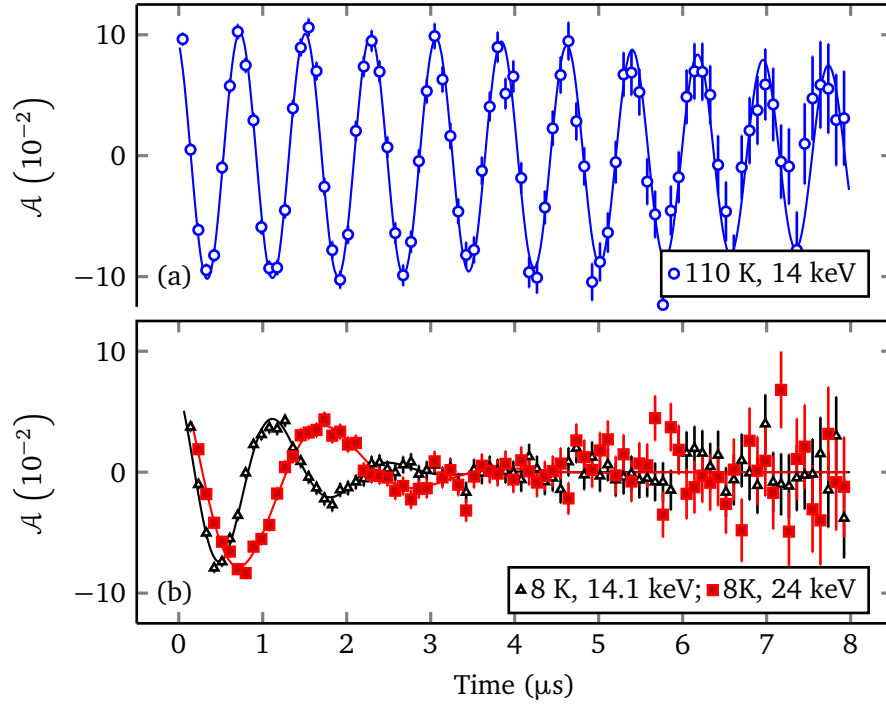


Figure 4.4: Top: The muon spin precession signal in the normal state of $\text{YBa}_2\text{Cu}_3\text{O}_{6.92}$ at 110 K in an external field of 9.46 mT applied parallel to the a direction. The mean implantation energy is $E = 14.1$ keV which corresponds to a mean implantation depth of 65 nm. Bottom: the same conditions as top except in the superconducting state at $T = 8$ K for two energies 14.1 keV and 24 keV.

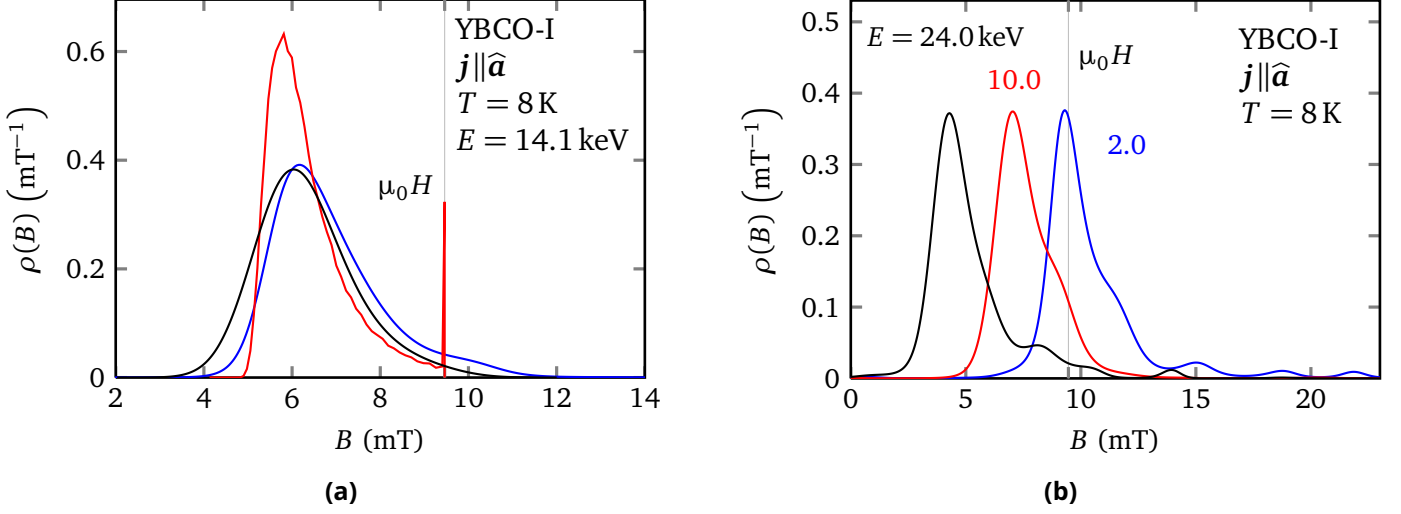


Figure 4.5: (a) Magnetic field distribution as seen by muons at an implantation energy of $E = 14.1$ keV and at $T = 8$ K in an external magnetic field $\mu_0 H = 9.5$ mT, applied parallel to the b axis of the crystals. The field distribution corresponds to the asymmetry spectrum (a) in the figure 4.4. The red line (—) is model field from pure London model with $d = 10.3$ nm, $\lambda_a = 128.9$ nm and $\sigma = 0$. The spike in $\rho(B)$ at the applied field is from muons stopping in dead layer. The black line (—) is the theoretical distribution convoluted with a Gaussian with a second central moment $\Delta B = 0.72$ mT corresponding to the average $\sigma = 0.61 \mu\text{s}^{-1}$ from the figure 4.6b). The blue line (—) is obtained from maximum-entropy analysis. The higher weight at high fields in actual field distribution is likely to be from trapped vortices close to the surface and is not taken fully into account by our symmetrically broadened field distribution. (b) Maximum-entropy field distribution are shown at three different energies. At the lowest energy, there is significant contribution from possible demagnetization and trapped vortices.

- 1 local field present at a muon site, a Gaussian probability model is assumed as,

$$P(B', B) = \left(\frac{1}{\sqrt{2\pi}\Delta B} \right) \exp \left(-\frac{1}{2} \left(\frac{B' - B}{\Delta B} \right)^2 \right) \quad (4.4)$$

- 2 where $P(B', B)$ is the probability function of the total field B' experienced by muon and ΔB
- 3 is the width of the probability function. Broadened total probability density is obtained by
- 4 convoluting (4.4) with the field distribution from the pure London model in the (4.3)

$$\rho'(B') \equiv \int_{B=0}^{\infty} P(B', B) \rho(B) dB \quad (4.5)$$

- 5 Since stopping distributions ($\rho(z)$) are obtained as discrete numbers from TRIM.SP simula-
- 6 tions, the integral in the (4.5) is replaced by a summation to calculate the total probability

density. As may be seen from the figure 4.5a, the field distributions from maximum-entropy (ME) [158–160] are wider than that expected from a pure London model ($\sigma = 0$). For the ME analysis a Gaussian apodization ($\sigma_{\text{apod}} = 2.0\mu\text{s}$) is used for all the energy dependent spectra. Apodization leads to very small symmetric broadening and smoothing of field distribution but is not expected to change the average magnetic field $\langle B \rangle$. This may be noted that there is considerable weight at higher fields (cf. figure 4.5b) than the applied field $\mu_0 H$ which is out of the scope of the (4.3).

In the equations (4.1) and (4.2), φ should ideally depend on purely geometric parameters and muon arrival time on the sample. Thereby, one way to analyze the spectra is to fix φ to values obtained at temperatures above T_c , as has been described in [161]. However, φ may be substantially different in the superconducting state compared to the values for $T > T_c$, as we will see shortly. φ may also depend on muon implantation energy in the following manner¹: in the normal state ($T > T_c$) the angular part of the asymmetry is given by

$$\mathcal{A}(t) \sim \cos(\omega(t - t_0)) \quad (4.6)$$

assuming $\varphi = 0$, for simplicity. Here $\omega = \gamma_\mu B$ is the frequency and t_0 being the time muon enters the sample. If an error is made in determining $t_0 \rightarrow t_0 - dt$, then (4.6) becomes

$$\mathcal{A}(t) \sim \cos(\omega(t - t_0) + \omega dt) \quad (4.7)$$

Equation (4.7) implies that the fitted phase will be ωdt . However, in superconducting state and in high implantation energy, muons deep inside the sample will see a reduced field and a corresponding reduced frequency $\omega'_E < \omega$, assuming for simplicity that all the muons precess in a single frequency. This implies that, in superconducting state, (4.7) may be written as

$$\mathcal{A}(t) \sim \cos(\omega'_E(t - t_0) + \omega'_E dt) \quad (4.8)$$

meaning a phase shift of $(\omega'_E - \omega)dt$ will be detected. The possibility of actual frequency distribution being more asymmetric than our theoretical frequency distribution one can also introduce an apparent phase shift. To summarize, imperfections in fitting function, TOF distribution and detector geometry may all introduce energy dependent phase shift. For the reasons above, phases for individual energies were kept free (**individual phase model**) in the global fit. A shared phase global fit analysis (**shared phase model**) was also done which yields $\lambda_{\{a,b\}}$ values within the systematic errors $\sim 3\text{nm}$. This is also a strong indication that the subtleties of muon arrival time, detector geometry and thereby the phases (φ) & broadening parameter (σ) do not significantly influence the extraction of the absolute values of London penetration depth.

¹This analysis was inspired by Rob Kiefl

Figure 4.4a shows the muon precession signal in the normal state at 110K in a small magnetic field of 9.5 mT applied along the a axis of the crystals with an implantation energy at 14.1 keV. Observed frequency in figure 4.4a also includes a damping rate of $0.086(11)\mu\text{s}^{-1}$ which is consistent with the damping from randomly oriented Cu nuclear dipole moments. Meissner screening of the external field is apparent by comparing the normal state (figure 4.4a) with the superconducting state (figure 4.4b). As mentioned earlier, the superconducting state data are fitted to (4.2) with shared A_0 , d and λ for all the spectra at 8 K in both a and b directions. The depth dependence of the average internal field is evident by comparing the two spectra (\circ and \blacksquare) in figure 4.4b which have different implantation profiles. Exemplary profiles are shown in figure 3.6a.

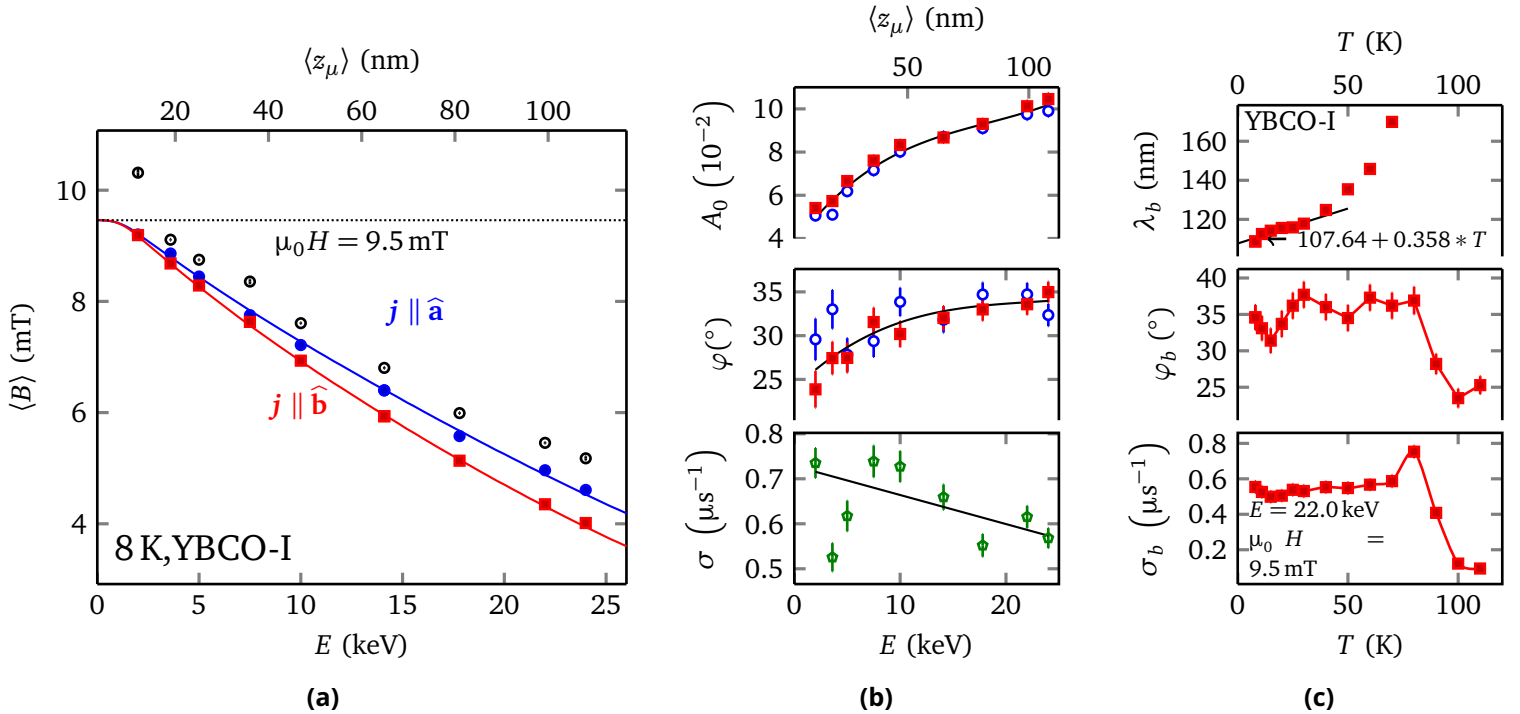


Figure 4.6: (a) The average magnetic field ($\langle B \rangle$) versus mean stopping depth in an applied field of 9.46 mT such that the shielding currents are flowing in the a direction ($\vec{j} \parallel \hat{a}$, \bullet) and b direction ($\vec{j} \parallel \hat{b}$, \blacksquare). The curves are the average fields generated from a global fit of all the spectra at 8 K taken at all energies and for both orientations. The common parameters are λ_a , λ_b and d . The individual points are from a fit to the same model but at a single depth. The differences between the data points and curves reflect how close the data at a single energy agrees with the global fit. (b) The phase, asymmetry and broadening parameter versus E . (c) Temperature dependence of λ , φ and σ when $\mu_0 H \parallel \hat{b}$. More details are in the text.

Figure 4.6a shows the average local field [$\langle B \rangle = \int \rho(z)B(z)dz$] determined from fits at a single energy as a function of beam energy (bottom scale) and corresponding mean

1 implantation depth (top scale). The filled circles (●) and filled squares (■) are from data
2 taken with the shielding currents flowing along the a and b axes respectively (or equivalently
3 the magnetic field along the b and a axes respectively); the black points (○) are from the
4 ME analysis for $H \parallel \hat{b}$ direction. The corresponding London model curves are generated
5 from a global fit of runs taken at 8 K for both orientations and all energies using the
6 calculated TRIM.SP implantation profiles. The common parameters are $\lambda_a = 128.9(12)$ nm,
7 $\lambda_b = 108.4(10)$ nm and $d = 10.3(4)$ nm. In the **shared phase model**, d is fixed to 10.3 nm
8 and the obtained $\lambda_{a,b}$ differs by ~ 1 nm as shown in the table 4.1. Statistical uncertainties
9 are determined from the global χ^2 surface and take into account the strong correlation
10 between $\lambda_{a,b}$ and d . Since there is almost no correlation between d and λ_a/λ_b , this ratio is
11 determined more accurately than the absolute values of λ_a and λ_b as may be seen in the
12 table 4.1. As may be evidenced from figure 4.6a, the average field falls exponentially from
13 the surface for higher implantation energies however, close to the surface, deviation from a
14 simple exponential is modelled from the curvature at the lowest energies. This implies that
15 the supercurrent density is suppressed near the surface relative to a London model. This is
16 idealized but the nature of the data does not warrant more complicated models. It is unclear
17 to what extent this suppression of the supercurrent density is intrinsic as a result of the
18 discontinuous nature of electronic properties near a surface. Higher average field from ME
19 analysis is likely due to trapped vortices close to the surface and from fields expelled from
20 neighboring crystals. A suppression of the supercurrent density was reported in a previous
21 low energy μ SR study of the field profile in a thin film of $\text{YBa}_2\text{Cu}_3\text{O}_{6.92}$ and attributed to
22 surface roughness [162]. It is difficult to exclude such extrinsic effects which could also lead
23 to a suppression of the supercurrent density near a surface. Measurements on atomically flat
24 cleaved surfaces are needed to resolve the origin of d . There are no other measurements of
25 electromagnetic properties as a function of depth in $\text{YBa}_2\text{Cu}_3\text{O}_{6.92}$ crystals to compare with.
26 Surface sensitive techniques such as STM and ARPES are only sensitive to the top few unit
27 cells where the properties can be very different than in the bulk.

28 It may also be noted from the figure 4.6b, that the fitted asymmetry goes from 5 % (low
29 energy) to 10 % (high energy). This is expected since at low energies, incoming muons
30 have an angular distribution as they approach the sample surface and at lower energy,
31 many of them are deflected backwards, i.e., backscattering reduces the number of total
32 muons, reducing the signal strength and asymmetry. The average phase from **individual**
33 **phase model** is close to that from the **shared phase model**, indicating that the latter model
34 determines an “effective average phase”. The broadening parameter σ ’s energy dependence
35 reflects the random local fields and is also temperature independent below $0.8 T_c$, as expected
36 and evidenced from the figure 4.6c. This is due to the bulk magnetization effects, whereby
37 flux expelled from neighboring crystals broadens the magnetic field distribution at the
38 surface of any given crystal. Since σ reflects the broadening of an **effective field** at a specific

Table 4.1: Summary of results in $\text{YBa}_2\text{Cu}_3\text{O}_{6.92}$: Measured London penetration depths at 8 K are shown for two models: “phase individual” and “phase shared”, for individual energies. The errors are reported here are just statistical errors. An additional $\sim 2\%$ (~ 2 nm) error is due to uncertainty in stopping distribution. It may be noted that the two phase models yield penetration depths within a nm of each other for both a and b axis, stressing that the determination of phase does not affect the measurement of absolute λ .

B (mT)	d (nm)	φ ($^\circ$)	$\lambda_a(8\text{ K})$ (nm)	$\lambda_b(8\text{ K})$ (nm)	$\mathcal{R} \equiv \lambda_a/\lambda_b$	χ^2/DF
9.46	10.3(5)	32.2(6) ^a	128.9(12)	108.4(10)	1.19(1)	1.058
	10.3 (fixed)	33.0(8) ^b	130.2(14)	109.2(12)	1.19(1)	1.069

^a Average of energy specific phases from “individual phase” analysis.

^b Global phase from “shared phase” analysis.

1 energy, it is always kept as a free parameter both in **individual phase model** and **shared**
2 **phase model**.

The absolute value of λ_b as a function of temperature is shown in figure 4.6c (top panel). The data points are the fitted values of λ_b determined from a fit to the model at a single implantation energy of 22 keV. Since d is not temperature dependent it was fixed at 10.3 nm. The solid line is a linear fit of our data below 30 K and gives a slope of $0.357(67)\text{ nm K}^{-1}$. This was used to extrapolate our measurement of λ_b at 8 K down to zero temperature. The slope and extrapolated value depend slightly on the fitted temperature range adding an additional systematic error of about 1 nm. To obtain $\lambda_a(0)$, normalized superfluid density in a and b axis directions are taken as approximately equal as in the (4.9)

$$\begin{aligned} \left(\frac{\lambda_a(0)}{\lambda_a(T)} \right)^2 &\simeq \left(\frac{\lambda_b(0)}{\lambda_b(T)} \right)^2 \\ \Rightarrow \lambda_a(0) &= \lambda_b(0) \left(\frac{\lambda_a(T)}{\lambda_b(T)} \right), \end{aligned} \quad (4.9)$$

3 where $\lambda_{a,b}(T)$ are the finite temperature penetration depths measured by our modified
4 London model.

5 Table 4.1 gives our results for λ_a and λ_b measured at 8 K in $\text{YBa}_2\text{Cu}_3\text{O}_{6.92}$. The errors
6 reported here are just the statistical uncertainty. Systematic errors due to uncertainties in
7 the muon stopping distribution and due to extrapolation to 0 K is $\sim 3\%$. At the moment,
8 the latter dominates the overall uncertainty but should improve with refinements of the
9 stopping distribution calculations. More details about possible slightly different stopping
10 profiles is available in the appendix. In summary we have used low energy μSR to measure
11 the magnetic field profiles in the Meissner state of a mosaic of detwinned single crystals
12 of $\text{YBa}_2\text{Cu}_3\text{O}_{6.92}$. The comparison of $\lambda_{a,b}$ values obtained here with those from different

1 methods is deferred until a later section. Since the data analysis method for the next three
2 sections will be very similar to this one, primarily differences will be mentioned.

4.1.2 $\text{YBa}_2\text{Cu}_3\text{O}_{6.998}$

4 In this section, total four sets of data are analyzed and presented: (i) in an external field
5 of 4.7 mT at three temperatures 4 K, 5 K and 12 K (ii) in an external field of 9.5 mT at the
6 temperature of 5 K.

7 Examples of the muon precession signals in the crystal mosaic may be seen in figure 4.7.
8 Figure 4.7a shows the muon precession signal in the normal state at 100 K in a small
9 magnetic field of 4.7 mT applied along the a axis of the crystals with an implantation energy
at 23.1 keV. In figure 4.7a, the average frequency corresponds to the applied field with a

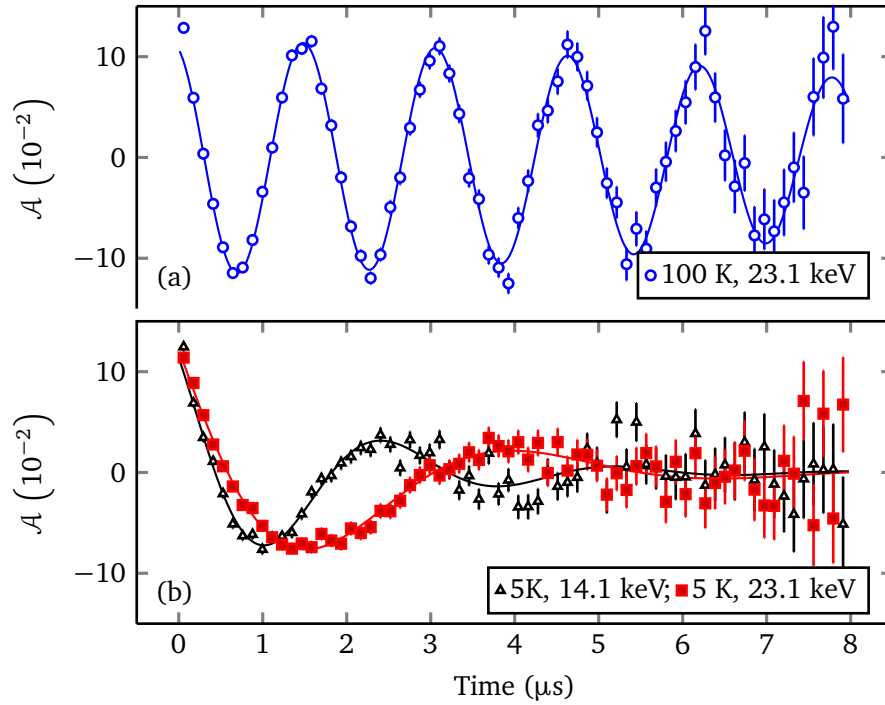


Figure 4.7: (a) The muon spin precession signal in the normal state of $\text{YBa}_2\text{Cu}_3\text{O}_{6.998}$ at 100 K, 23.1 keV in an external field of 4.7 mT applied parallel to the a direction. (b) The same conditions as (a) except in the superconducting state at $T = 5$ K with an two implantation energies 14.1 keV and 23.1 keV. The solid lines are fits to a London model profile described in the previous section.

10

11 damping rate of $0.110(10)\mu\text{s}^{-1}$, which is slightly bigger than obtained in $\text{YBa}_2\text{Cu}_3\text{O}_{6.92}$
12 but nonetheless consistent with a random local field distribution. All measurements in
13 the superconducting state were carried out under **zero-field-cooled** conditions in order to
14 avoid flux trapping at the surface. Meissner screening of the external field is apparent by
15 comparing the normal state in figure 4.7a with the superconducting states in figure 4.7b. The

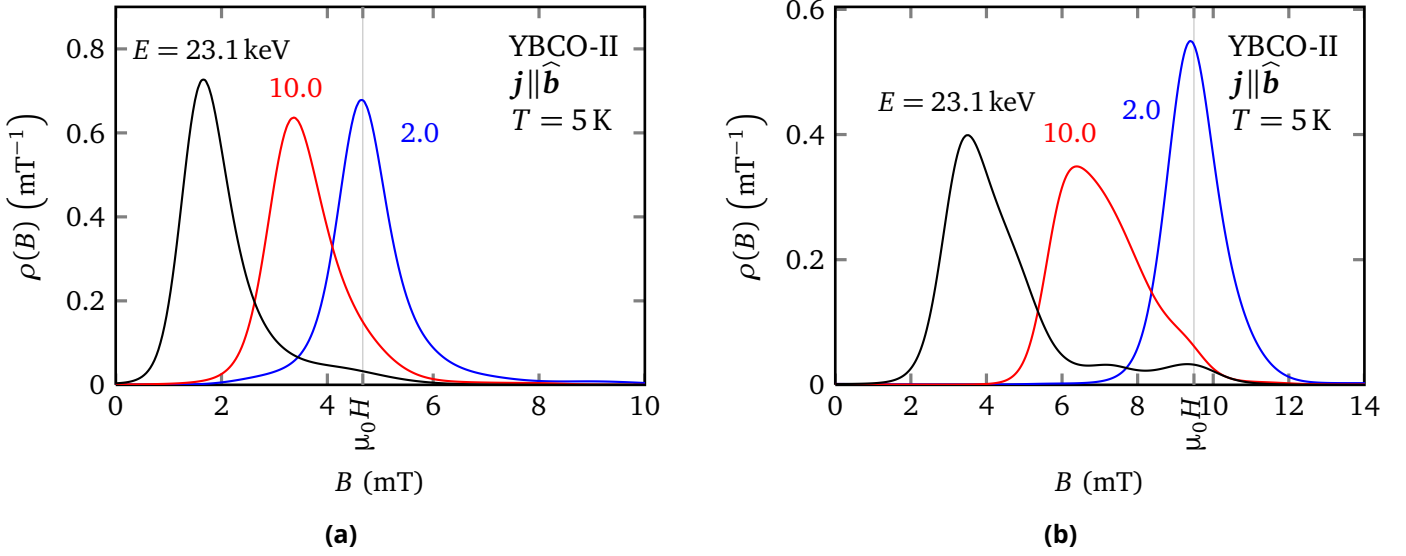


Figure 4.8: Magnetic field distribution as seen by muons at various implantation energies and at $T = 5$ K in an external applied magnetic field ($\mu_0 H$) of 4.7 mT and 9.5 mT, applied parallel to the a axis.

1 depth dependence of the average internal field(ω) is also perceptible by comparing the two
2 spectras in figure 4.7b which have different implantation profiles. The curves in figure 4.7b
3 are generated from fits to a London model profile as described in the previous section. Since,
4 the precession signal spectra bear similar characteristic as figure 4.7, further precession plots
5 are omitted for this sample.

6 Maximum entropy field distributions corresponding to the two external fields of 4.7 mT
7 and 9.5 mT are shown.in the figure 4.8. As may be noticed, $\rho(B)$, corresponding to the
8 higher applied field (9.5 mT), is more asymmetric. However, in both cases, there are long
9 tails, in field distributions, even at higher implantation energies possibly due to trapped
10 vortices close to the surface.

11 The fitted asymmetry in figure 4.9 varies between 5% (low energy) to 10% (high
12 energy). This is consistent with backscattering of muons at low energies. The phases for
13 individual runs varies between $\sim 15^\circ$ to 40° . This range is also consistent with phases noticed
14 in the previous section, underlining that the systematic errors in determining a precise phase
15 remains the same. For low temperatures significantly below the critical temperature T_c ,
16 the broadening parameter σ is about $0.4 \mu s^{-1}$ (bottom panel, figures 4.9a to 4.9c) which
17 is about half of that observed in $YBa_2Cu_3O_{6.92}$ in 9.5 mT. This is reasonable considering
18 the magnetization effects coming from neighboring crystals will also be reduced with the
19 reduced applied field of 4.8 mT. It may be also noted from figure 4.9d that the average σ
20 at the external field, $B_o = 9.5$ mT, is about the same as that from $YBa_2Cu_3O_{6.92}$, figure 4.6
21 indicating that the broadening is due to expelled flux from crystals and is not very sensitive

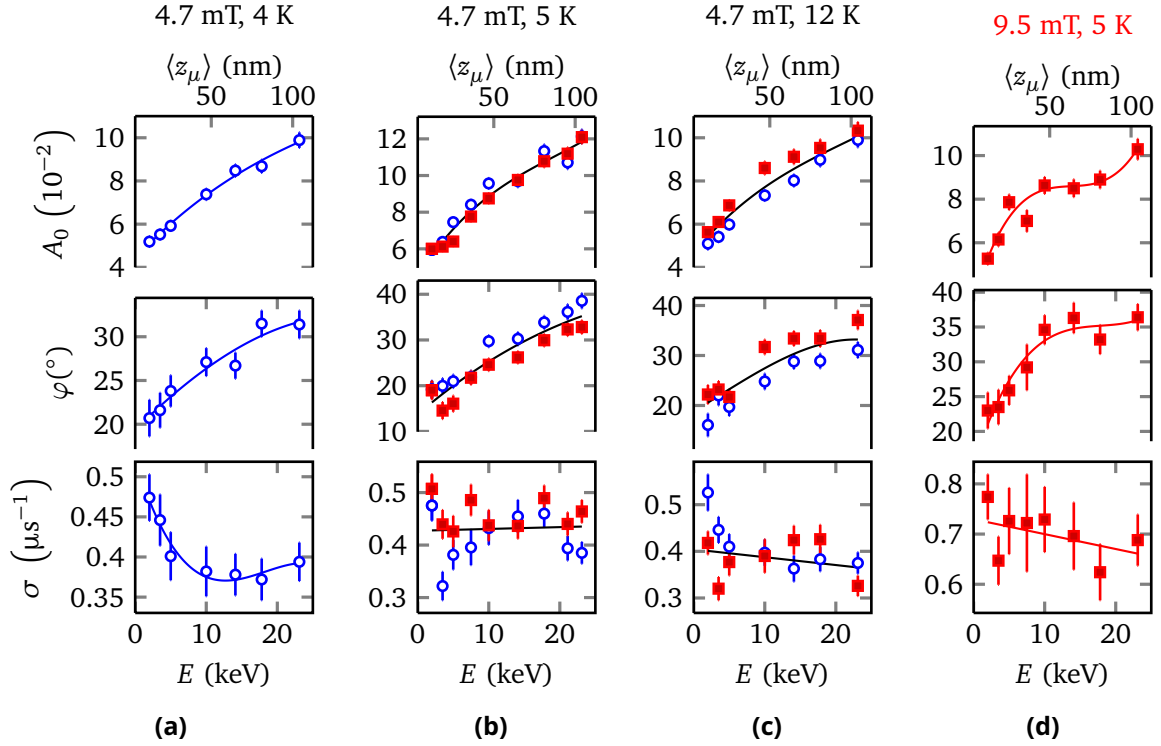


Figure 4.9: Asymmetry, phase and broadening parameter: The three important parameters for individual energy runs in the global fit, with shared λ_a , λ_b and d are shown. The small asymmetry at low energy is due to backscattering. The phase shows energy dependence, possibly due to inaccuracy in determined t_0 . The broadening parameter (σ) shows some random variation with an average $\sim 0.42 \mu s^{-1}$ at the external field $\mu_0 H = 4.7$ mT; the higher values at low energy may be due to vortices entering the samples close to the surface and broadening the field distribution.

1 to the geometric arrangement of crystals in the mosaic.
2 Figure 4.10 shows the average local field $\langle B \rangle = \int \rho(z)B(z)dz$ determined from fits
3 at a single energy as a function of beam energy (bottom scale) and corresponding mean
4 implantation depth (top scale). The open circles and filled squares are from data taken
5 with the shielding currents flowing along the a and b axes respectively (or equivalently the
6 magnetic field along the b and a axes respectively). As may be noticed in figure 4.10, the
7 theoretical global fit $\langle B \rangle$ line(s) are in excellent agreement with the individually measured
8 $\langle B \rangle$. The common parameters are all shown in the table 4.2 and $\lambda_{a,b}$ along with χ^2/DF
9 are plotted in the figure 4.13. Since there is almost no correlation between d and λ_a/λ_b ,
10 this ratio is determined more accurately than the absolute values of λ_a and λ_b as shown in
11 the seventh column of the table 4.2. Slightly different penetration depths $\lambda_{a,b}$ and other
12 parameters are obtained in the **individual phase model** compared to the **shared phase**
13 **model**. The differences in average field from the two models is negligible.

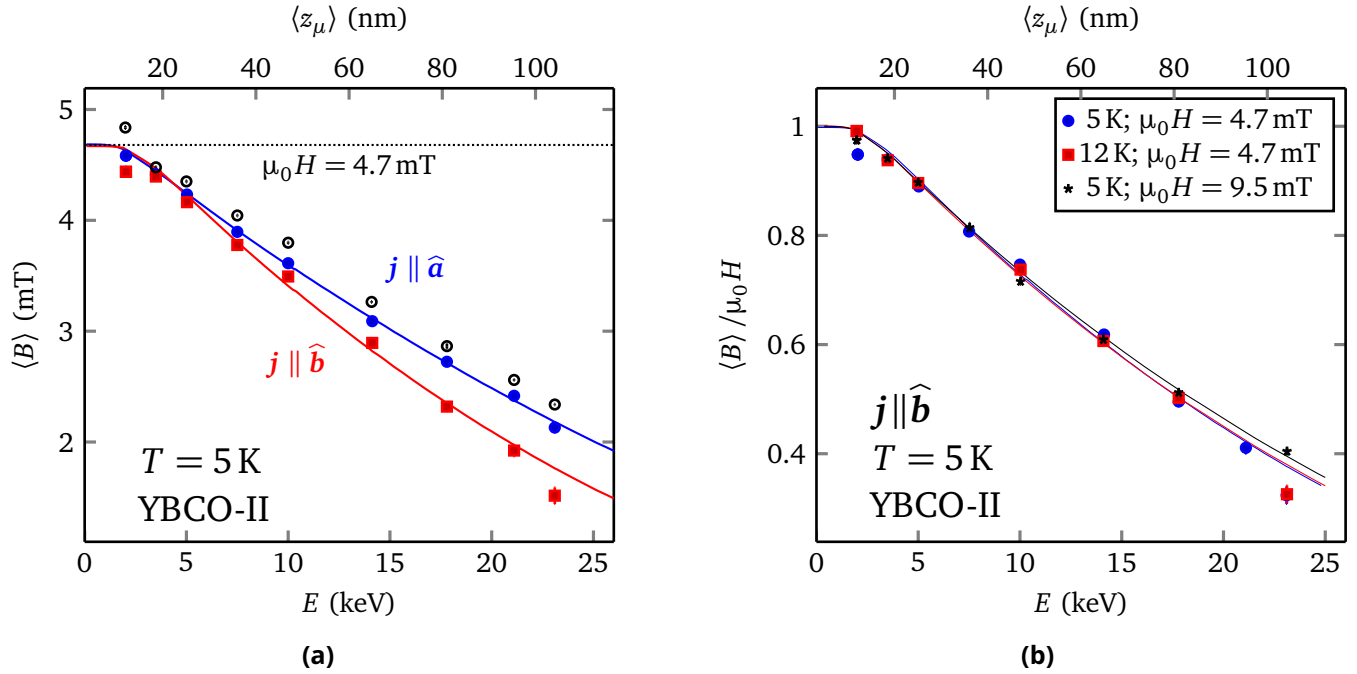


Figure 4.10: (a) The average magnetic field ($\langle B \rangle$) versus mean stopping depth in an applied field of 4.7 mT. The curves are the average fields generated from a global fit of all the spectra at 5 K taken at all energies and for both orientations (cf. figure 4.6). (b) Relative average magnetic fields in this sample for two temperatures and two magnetic fields. It is apparent that the absolute London penetration depths measured here are, differ only slightly.

Figure 4.12 shows the temperature dependence of penetration depth λ_a at 4.7 mT and 23.1 keV. The λ_a 's are obtained via the method of "individual phase" analysis of measurements with a d fixed to 14.79 nm, obtained from global fit of measurements in both a and b direction. The measured λ_a 's are fitted to a line giving $\lambda_a(0 \text{ K}) = (112.26 \pm 1.46)$ nm and slope of the line ($\Delta\lambda/\Delta T = 0.495 \pm 0.078$ (nm/K)). Since these measurements were done at a single energy, $\lambda_a(0 \text{ K})$ isn't a very good measure of penetration depth at zero temperature; however, note the closeness ($\lambda_a(5 \text{ K}) \sim 115$ nm) with the absolute λ_a 's found from global fits table 4.2. The $\Delta\lambda/\Delta T$ is a good measure of low temperature dependence of λ_a and will be used to extrapolate zero temperature penetration depths from the finite temperature ones.

It may be noted that $\lambda_{a,b}$ increases slightly as temperature is increased (4K to 5K) which is consistent with $\sim 0.5 \text{ nm K}^{-1}$ increase, as found from the temperature dependence in the figure 4.12. It may also be noted that the ratio between the two penetration depths, \mathcal{R} , slightly ($\sim 4\%$) depend on whether the **individual phase model** or the **shared phase model** was used. However, the difference is within statistical ($\sim 1\%$ to 2%) and systematic uncertainty ($\sim 3\%$) in $\lambda_{a,b}$. The **goodness of fit** χ^2/DF becomes slightly worse ($\sim 10\%$)

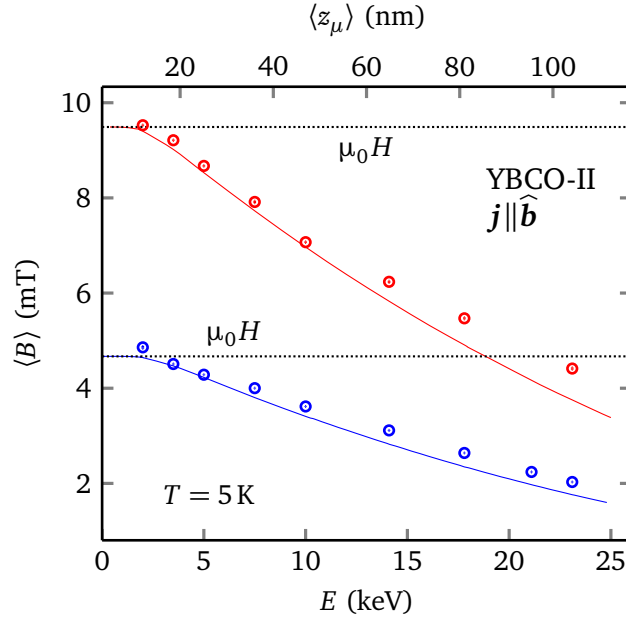


Figure 4.11: Comparison of average magnetic field from ME method with that from modified London model global fit. External fields are applied parallel to a axis of the crystal, i.e $j \parallel b$.

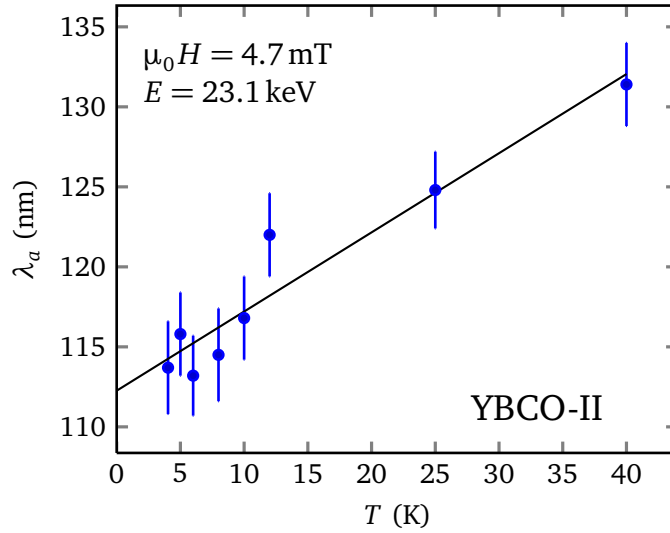


Figure 4.12: Temperature dependence of London penetration depth with in low temperatures are shown. The muon beam energy for this set of runs is $E=23.1$ keV and an external field of 4.7 mT is applied parallel to b -axis. A linear fit of $\lambda_a(T)$ yields $\lambda_a(0) = 112.26 \pm 1.46$ and $\Delta\lambda/\Delta T = 0.495 \pm 0.078$. The slope was used to extrapolate finite temperature penetration depth to 0 K.

Table 4.2: Summary of results for $\text{YBa}_2\text{Cu}_3\text{O}_{6.998}$: Measured London penetration depth in external fields of 4.7 mT & 9.5 mT are shown, for “phase individual” and “phase shared” models. There is some φ -dependence (of the order of systematic uncertainty) of measured penetration depths. It’s interesting to note that the “dead layer” d is within 10 to 20 nm indicating that it is a temperature and magnetic field invariant quantity. The shared phase is for 4.7 mT experiments is $\sim 25^\circ$ and slightly higher for the 9.5 mT set of runs. The χ^2/DF is slightly less for “individual phase” models, which indicates better fits.

B (mT)	T (K)	d (nm)	φ ($^\circ$)	λ_a (nm)	λ_b (nm)	$\mathcal{R} \equiv \lambda_a/\lambda_b$	χ^2/DF
4.66	4	14.8(9)	27.0(16) ^a	115.6(18)	\emptyset	\emptyset	1.323
			25.9(13) ^b	119.2(24)	\emptyset	\emptyset	1.385
4.67	5	17.2(15)	27.0(16) ^a	107.5(39)	84.0(35)	1.28(2)	1.257
			23.0(13) ^b	114.2(26)	92.7(22)	1.23(1)	1.382
4.66	12	16.8(6)	27.9(15) ^a	117.2(25)	87.7(21)	1.34(3)	1.448
			25.4(6) ^b	120.3(18)	93.9(14)	1.28(1)	1.586
9.49	5	16.5(8)	31.1(20) ^a	\emptyset	91.9(22)	\emptyset	1.105
			30.1(16) ^b	\emptyset	94.4(17)	\emptyset	1.135

^a Average of energy specific phases from “individual phase” analysis.

^b Global phase from “shared phase” analysis.

1 with **shared phase model**, although, global phase is determined within a statistical error of
2 $\sim 2\%$.

3 We will now summarize the analysis of this section as found in the table 4.2 and fig-
4 ure 4.13. It is interesting to note that the **dead layer** d , the layer close to the surface of
5 the crystals where supercurrent is suppressed, varies only between 15 nm to 17 nm where
6 in $\text{YBa}_2\text{Cu}_3\text{O}_{6.92}$, it was found to be 10.3 nm. Regardless of the temperature, oxygen dop-
7 ing & applied external magnetic field, there seems to be an thin ($\leq 10\%$) outside layer
8 where the supercurrent is suppressed. Regardless of the **phase models**, the determination
9 of phase is not very sensitive to whether we have data along both axis or just one axis.
10 Determination of phase is important since fitted values of $\lambda_{a,b}$ depends slightly on whether
11 phases are energy specific or a single phase should be assumed for the entire set of runs.
12 To discern between phase and frequency (and thereby average field), more oscillations in
13 signal is better, which is feasible closer to the surface. Deeper in the sample, field drops
14 by a significant fraction and thereby frequency becomes proportionately low which results
15 in phase & average frequency somewhat correlated. Yet, the correlation among φ and ω
16 doesn’t produce significant uncertainty in d and $\lambda_{a,b}$ as they are determined from a range
17 of implantation energies (i.e global fit). This may be observed from the plot of phases as
18 function of energy in figure 4.9, that the errors in phases are about the same in both low

(closer to surface) energies and high (deeper in the sample) energies. The sharp increase in σ at lower implantation energies (close to surface) is possibly due to pinned vortices at the top layers of the crystals. Broad field distribution close to the surface doesn't, however, influence determination of λ as the latter depends primarily on the field distribution deeper in the sample. The fitted phases are found to be almost temperature independent, however weakly field dependent, as φ increases $\sim 5^\circ$ as the applied field becomes doubled. With the mozaic of $\text{YBa}_2\text{Cu}_3\text{O}_{6.92}$, global φ was found to be 33.0 ± 0.8 at an external magnetic field of 9.5 mT. While the origin of phases' dependence on applied magnetic field remains to be understood, the determination of the London penetration depths $\lambda_{a,b}$ and their ratio \mathcal{R} can be determined with with a few percent uncertainty. With our simple model of London penetration depth, dead layer d and penetration depths $\lambda_{a,b}$ are inversely correlated, as d 's increase will decrease $\lambda_{a,b}$ and vice versa. However, the ratio \mathcal{R} is immune to the variations just mentioned and thereby has better accuracy. One important model (**phase**) dependent variation is the biggest uncertainty in determination of \mathcal{R} . Although measured at finite temperatures (4 K, 5 K and 12 K), \mathcal{R} is a good measure of the penetration depth anisotropy down to 0 K, assuming the nomalized superfluid density being equal at both directions at any temperature as given in the (4.9).

As may be noticed the from table 4.2 and figure 4.13, that the χ^2/DF ("goodness of fit") depends on applied external magnetic field strongly and slightly on the (phase) model. Higher external field induces more oscillations in the spectrum & thereby average magnetic field (frequency) inside the sample can be determined with better accuracy. The χ^2/DF for 9.5 mT set of measurements in $\text{YBa}_2\text{Cu}_3\text{O}_{6.998}$ is very much comparable to that of $\text{YBa}_2\text{Cu}_3\text{O}_{6.92}$. χ^2/DF also is smaller (better fit) for a fit with energy specific phases compared to a global phase. This is expected as more free (fit) parameters mean more degrees of freedom for the model and a better fit, however it introduces correlations among variables φ , σ and asymmetry. Nonetheless, statistical uncertainty in "shared phase" model is better as χ^2/DF is inversely correlated with the number of parameters. Model dependent uncertainties can be avoided if better measurements of phase may be done for a specific set of measurements. In the following section, we have a better determination of phase in a novel way, which avoids the uncertainty from a lack of knowledge of unique phase. However, it should still be noted that model dependence of $\lambda_{a,b}$ only introduces an additonal error of the order of statistical uncertainty from a single model.

4.1.3 $\text{YBa}_2\text{Cu}_3\text{O}_{6.52}$

As has been discussed in the sections 4.1.1 and 4.1.2, determination of London penetration depths $\lambda_{a,b}$ although may be done with a few percent statistical uncertainty, the **shared phase vs individual phase** models introduces additional systematic uncertainties in obtained $\lambda_{a,b}$. To have a simpler model having one effective phase (depending on when muon enters into sample and partially on other geometric factors), a novel method was used to determine

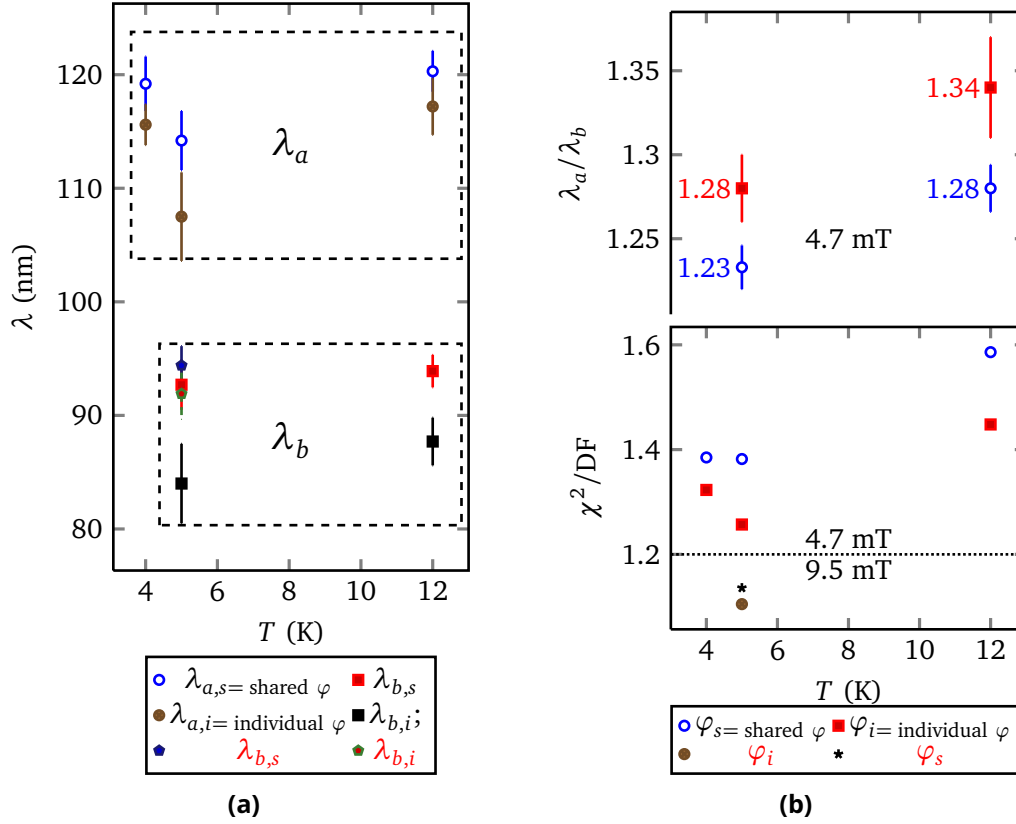


Figure 4.13: Summary of results for YBa₂Cu₃O_{6.998}: Measured London penetration depth in external fields of 4.7 mT & 9.5 mT are shown, for **individual(shared) phase** models. There is some φ -dependence (of the order of systematic uncertainty) of measured penetration depths. The λ_a/λ_b and χ^2/DF is slightly less for **individual phase model**, which indicates better fits. More discussion are in the text.

- 1 φ . Two normal state runs were taken at a single field (to be determined from fit) but one of
- 2 them having its direction reversed. The resulting spectra is plotted in the figure 4.14. These
- 3 normal states runs were taken, as a standard procedure, *after* the superconducting state
- 4 runs in zero-field-cooled magnetic field, to avoid any flux trapping and to have an accurate
- 5 determination of normal state field. Having a negative magnetic field $-B$ is identical to
- 6 having a precession in negative time, as

$$\omega t \equiv \gamma_\mu(-B)t = (\gamma_\mu B)(-t).$$

- 7 These precessions with B and $-B$ fields essentially double the length of muon precession
- 8 time and fitting to the entire length with asymmetry spectrum function

$$\mathcal{A}(t) \equiv A_0 \exp \left[-\sigma^2 t^2 / 2 \right] \cos(\gamma_\mu B_\circ t + \varphi_\circ)$$

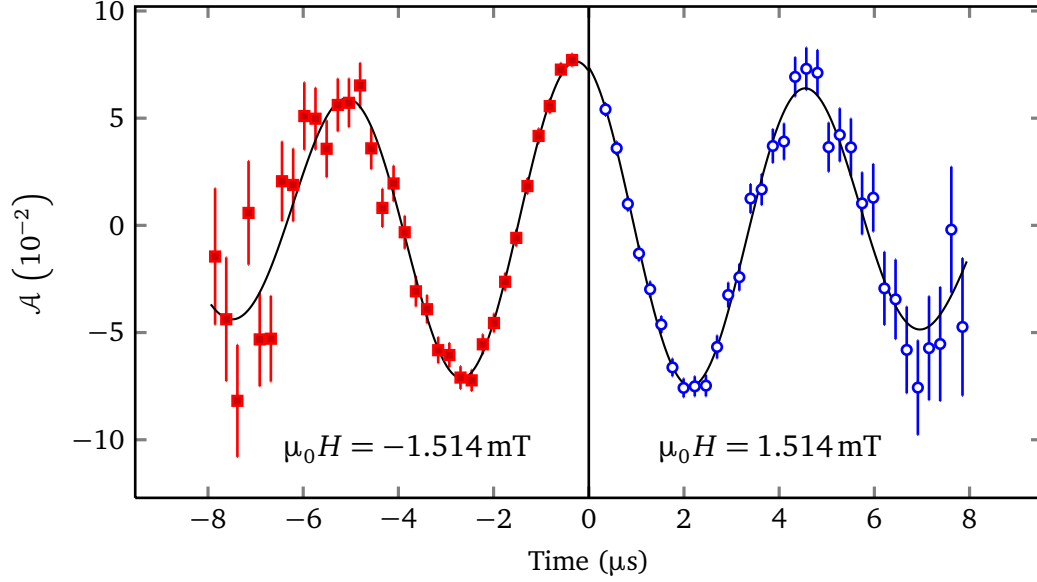


Figure 4.14: YBCO 6.52 in an applied field of 1.45 mT & -1.45 mT at 80K. Field reversing is like taking a measurement in negative time. $\varphi = 20.1 \pm 1.0$ and $\sigma = 0.14(1)$

one can determine $\mu_0 H$, φ and σ (for normal state). The fitted values from figure 4.14 were found to be $\mu_0 H = 1.514(6)$ mT, $\varphi = 20.1(10)^\circ$ and $\sigma = 0.14(1)\mu s^{-1}$. This unique determination of phase is specially crucial at low field since, muon oscillation frequencies ($\omega = \gamma_\mu B$) are also lower and fewer full oscillations are available (thereby a large correlation between φ and ω) in the spectrums as may be viewed in figure 4.15. Note the clear reduction in precession frequency (thereby, internal field) in figure 4.15 from normal state to superconducting states. This should be stressed that treating φ to be a geometric parameter and to be equal to the normal state phase is a deviation from the analyses done so far. However, with the set of runs with 1.5 mT external field, only a fixed phase (20.1, found from normal states) analysis is shown in table 4.3 as a global fit with **shared phase model** results in unrealistic average magnetic fields close to the surface. Fixing φ to the normal state values yields a better estimate of average frequencies, although usually a higher χ^2/DF . However, it may be noticed from table 4.3 that 1.5 mT set of runs yields the lowest χ^2/DF as well. The other two sets of measurements with higher external fields of 4.6 mT and 7.8 mT are analyzed with both a fixed phase (20.1) and with a **shared phase model**.

The fitted asymmetry and depolarization rate σ corresponding to the individual energies' in the global fit setup at $\mu_0 H = 1.5$ mT are shown in the figure 4.16. As may be noticed, the asymmetry rises with muon incident energy just like the previous experiments have shown, however, the very linear fashion of rise is interesting. It may also be noted that the range for asymmetry variation is $\sim 4\% - 10\%$, meaning that there is no significant loss of

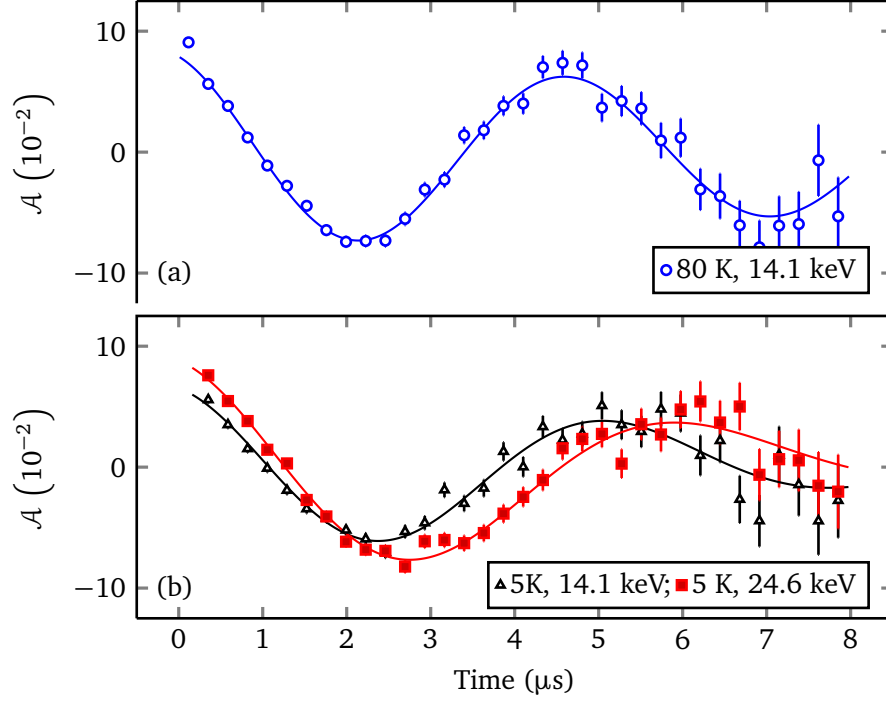


Figure 4.15: Top: The muon spin precession signal in the normal state of $\text{YBa}_2\text{Cu}_3\text{O}_{6.52}$ at 80 K in an external field of 1.5 mT applied parallel to the b -direction. The mean implantation energy is $E = 14.1$ keV which corresponds to a mean implantation depth of 65 nm. Bottom: The same conditions as above except in the superconducting state at $T = 5$ K with energy 14.1 keV & 24.6 keV.

1 signal strength compared to the experiments done on $\text{YBa}_2\text{Cu}_3\text{O}_{6.92}$ and $\text{YBa}_2\text{Cu}_3\text{O}_{6.998}$.
2 The damping rate σ is about the same as the value obtained in previous sections at higher
3 magnetic fields. This is reasonable damping from host Cu nuclear dipole moments. One
4 other feature is that σ is almost invariant as a function of implantation energy, as is ideally
5 expected, but close to the surface, it rises significantly. This suggests that the actual field
6 distribution is broader than than expected from a purely stopping distribution $\rho(z)$ related
7 one. One possible source of broadening is field expelled from neighboring crystals. However,
8 that would increase (not observed) the average field close to the surface. More feasible is the
9 possible entrance of magnetic vortices close to surface which would introduce broadening in
10 magnetic field while maintaining an average field close to the external applied field. Higher
11 external fields in the figure 4.16, yields $\sigma(E) \propto E$. It may be speculated that vortices enter
12 into significant percentage of area close to the surface and just below $\sim \text{nm}$ of the sample
13 surface, very few vortices remain, however the vortex core gets widened in as it gets deeper
14 into the sample, thereby increasing the width of the field distribution.

15 Figure 4.18 shows the average λ and individually fitted (with d fixed) λ for 1.5 mT and
16 4.6 mT external fields. It may be noted that the global fits well represent the individual

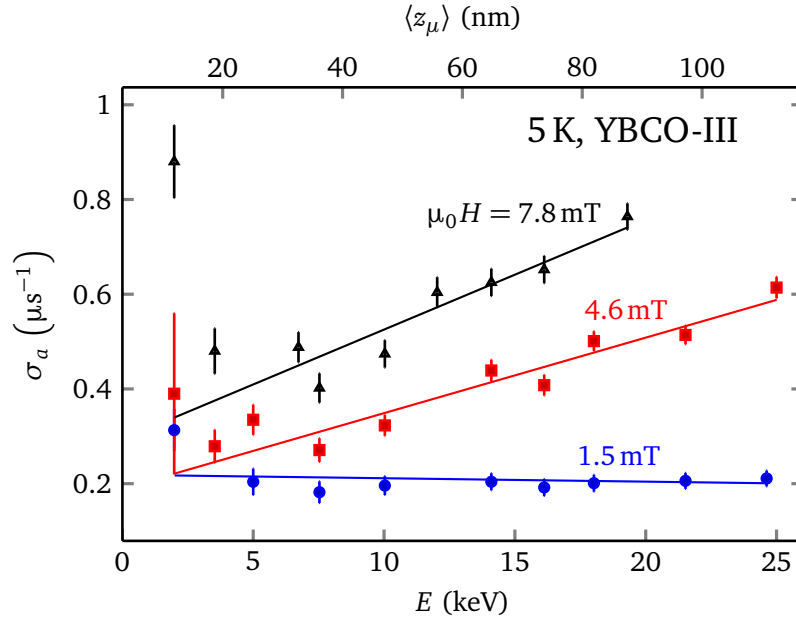
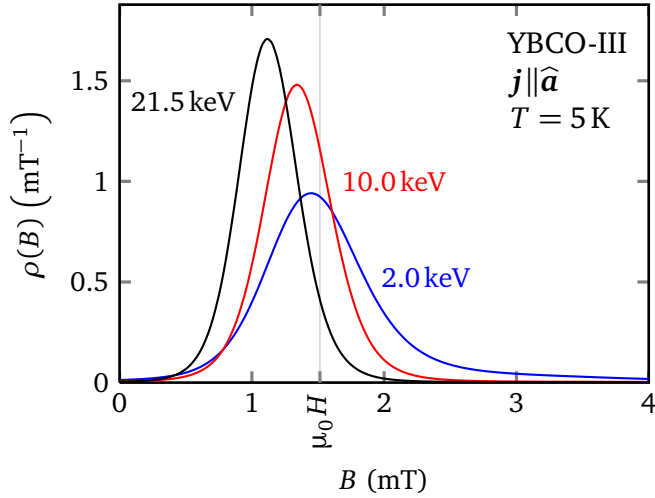
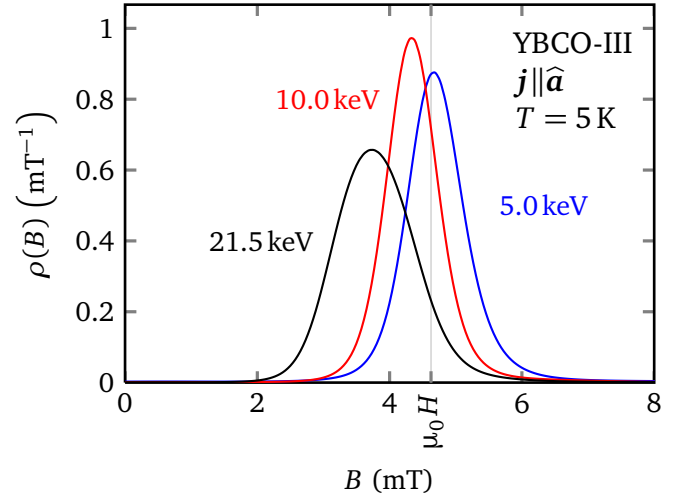


Figure 4.16: YBCO 6.52 broadening parameter are shown for an external applied field of 1.45 mT, 4.6 mT and 7.8 mT such that the shielding currents are flowing in the a direction ($j \parallel \hat{a}$). The common parameters are λ_a , λ_b and d . The upturn in σ at lower energies are possibly due to vortex entrance close to the surface. The solid lines are guides to the eye.



(a)



(b)

Figure 4.17: Magnetic field distribution as seen by muons at various implantation energies and at $T = 5$ K in an external applied magnetic field ($\mu_0 H$) of 1.5 mT and 4.6 mT, applied parallel to the b axis.

energy specific fits except at low energies, where $\langle B \rangle$ isn't very sensitive (thereby large error bars) to the penetration depths. Although λ 's show large error close to the surface, the error produced in $\langle B \rangle$ is considerably smaller as only dead layer d dominates the average magnetic field computation in this region. Fitting the set of superconducting state runs

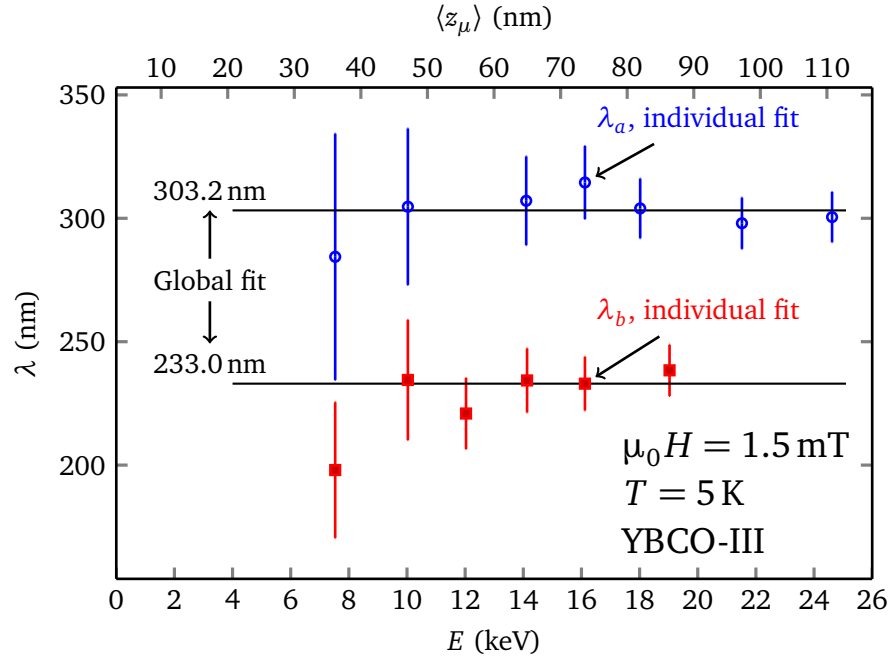


Figure 4.18: Global fit λ and individually fitted λ 's are shown for the external field of 1.5 mT. As may be noticed, individual penetration depths scatter around the global fit values except at lowest energies, since at these energies λ is less sensitive measure to the average magnetic field $\langle B \rangle \approx B_0$.

at 1.5 mT with a London model, as described earlier, global $\lambda_{a,b}$ and dead layer d are determined. The corresponding global and individual average magnetic fields are shown in the figure 4.19a. The closeness of the individual average field points to the global fit lines represent how close the data at single energies agree with global fit with shared $\lambda_{a,b}$ and d . A comparison of relative average magnetic field for 1.5 mT, 4.6 mT and 7.8 mT is shown in the figure 4.19b. It is clearly evident that the lowest $\lambda_{a,b}$ for this sample results from the 1.5 mT set of runs. As may be noticed the average field ($\langle B \rangle$) in the figure 4.19 doesn't drop until ~ 5 keV, corresponding to an implantation energy ~ 25 nm which is also reflected in the dead layer d in the table 4.3. One interesting phenomenon consistently seen in all analyses is that the d is between 10 nm to 30 nm, irrespective of the external field magnitude $\mu_0 H$ or orientation, suggesting that some intrinsic mechanism being responsible for the reduced supercurrent close to the surface. To extract $\lambda_{a,b}(0)K$, temperature dependent measurements of penetration depths have been obtained as shown in the figure 4.21. It may be noticed that low temperature dependence of λ is linear only at an external field of 1.5 mT.

1 The higher external field of 4.6 mT yields very nonlinear temperature dependence possibly
2 indicating entrance of vortices in the mosaic, as already argued noting that $\sigma(E)$ increases
3 almost linearly, with higher energy, as shown in the figure 4.16. The unusual temperature
4 dependence of $\lambda_a(T)$ in the 4.6 mT set of measurements prompted the significantly lower
5 1.5 mT set of measurements. The resulting slope from the 1.5 mT temperature dependence
6 has been used to extrapolate $\lambda_b(5\text{ K})$ to $\lambda_b(0\text{ K})$. Penetration depth in the other orientation
7 $\lambda_a(0\text{ K})$ has been obtained using the (4.9).

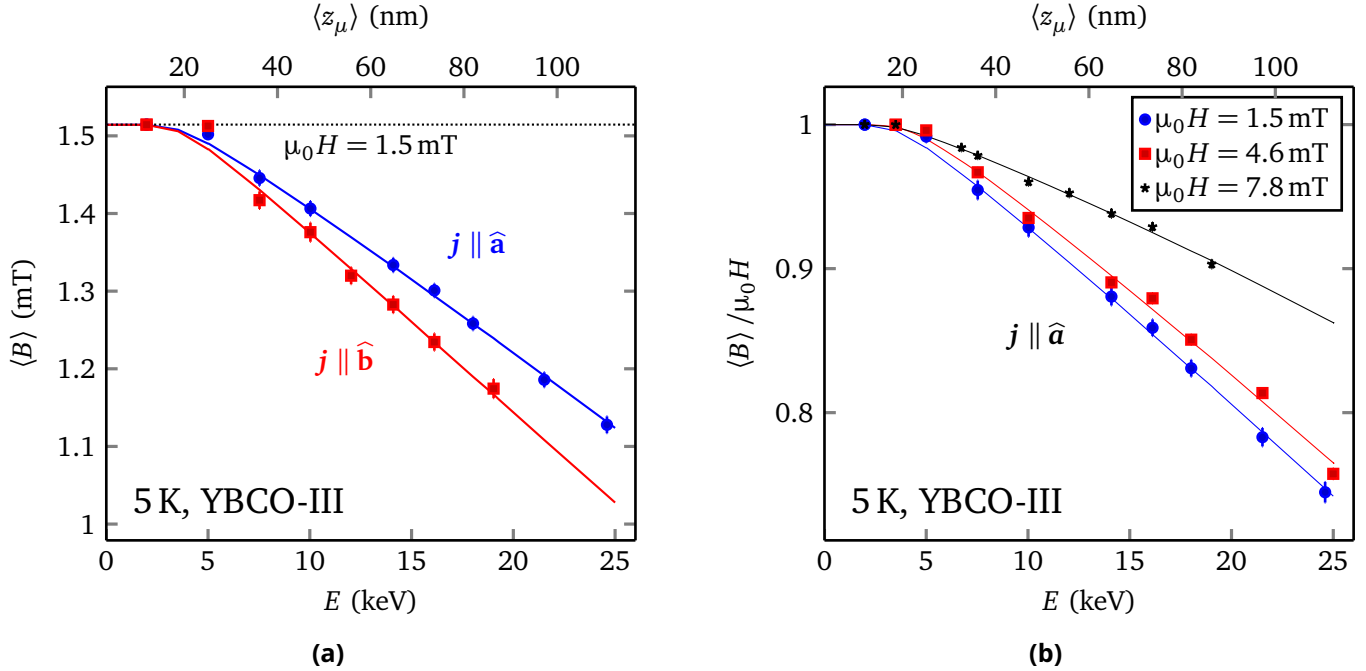


Figure 4.19: YBCO 6.52 average magnetic field \vec{B} inside the sample. The average magnetic field versus energy (mean stopping depth) in an applied field of 1.45 mT such that the shielding currents are flowing in the a direction ($\vec{j} \parallel a$, open circles) and b direction ($\vec{j} \parallel b$, filled squares). Relative average local magnetic field with respect to the applied field as a function of muon implantation energy for the two fields of 4.7 mT, and 9.5 mT applied parallel to the b axis of the YBCO-III. The depicted fields have been calculated in the same way as in Fig. and normalized to the applied fields.

8 Figure 4.22a shows effective penetration depth λ_b 's dependence on external field. The
9 phase was left fixed at the normal state value at 1.5 mT, for all three analyses. As argued
10 before, the two higher field of 4.6 mT and 7.8 mT have possible vortex penetration and
11 obtained λ_a are just effective penetration depths which can be used to determine average
12 magnetic field at various depths using the stopping distribution $\rho(z)$. Note that the effective
13 λ_a s from global fit are more reliable than the single run λ_b s (with a fixed $d = 23.6$ nm)
14 shown in figure 4.22a. Although the individually fitted λ_b values are less reliable, the almost

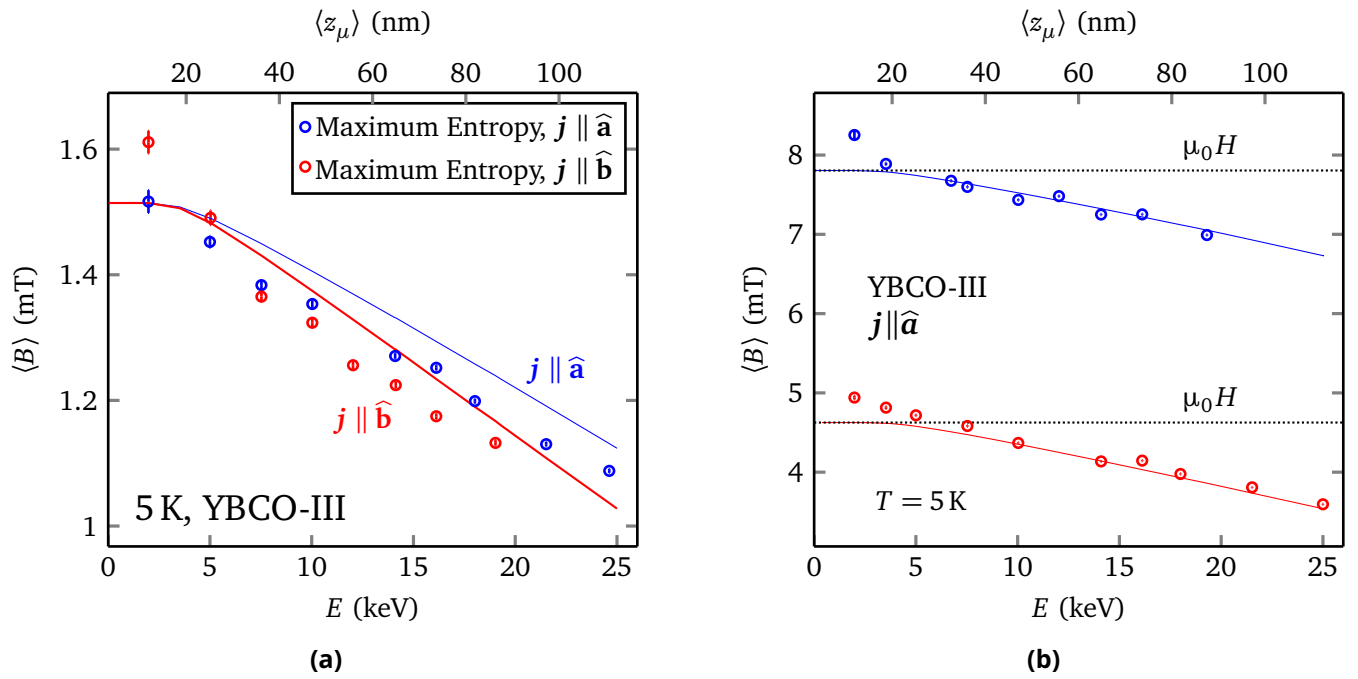


Figure 4.20: Comparison of average fields from maximum entropy and London model.

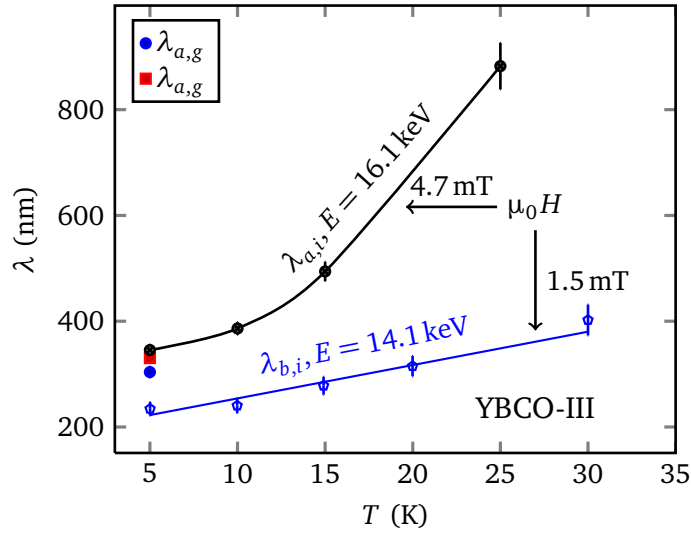


Figure 4.21: As may be noticed that the average field increases, with a corresponding large increase in λ , with temperature. Possible entrance of vortices is likely the reason of increase of “effective λ ”. This prompted us to take low field (1.6 mT) set of runs. The fit parameters at 1.5 mT external field are, intercept= 191 ± 13.38 nm. slope= 6.305 ± 0.96 nm/K. The slope is an order of magnitude bigger than that found in other oxygen dopings of YBCO.

1 linear field dependence strongly suggests magnetic vortex entrance at higher fields. Also may
2 be noted from the figure 4.22b, normal state phases to be almost independent ($\sim 25^\circ$) of
3 applied external field while the superconducting state phase seems to be slightly dependent
4 on applied field for $\mu_0 H > 6$ mT. The broadening parameter σ in the superconducting state
5 rises almost linearly with the applied external magnetic field due to the expelled flux being
6 proportional to the applied field. Although the single fit λ_b s in the figure 4.22a are not very
7 reliable, it does bring an important point that caution must be taken to measure the London
8 penetration depth in the Meissner state by excluding possibility of vortices getting in the
9 sample.

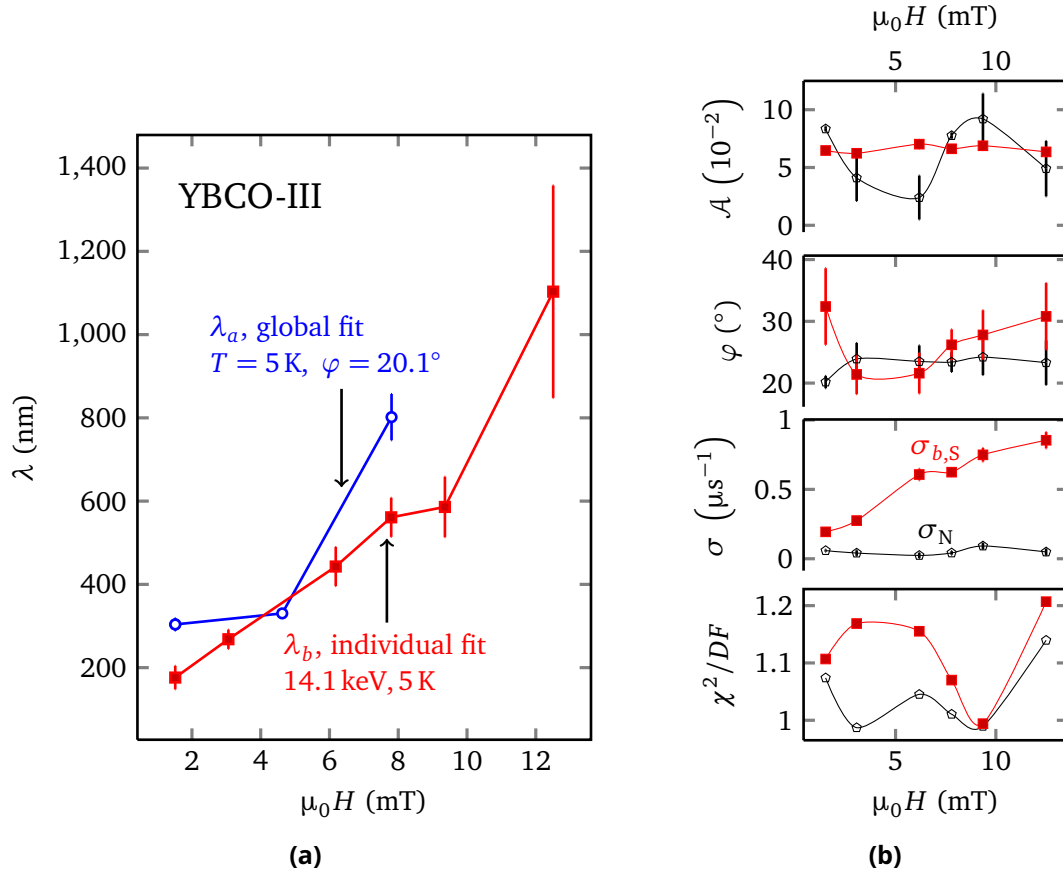


Figure 4.22: (a) Single measurements of effective penetration depths in various external magnetic fields are shown here. The almost linear rise in λ_b with magnetic field stresses that lower external field must be used and also be made sure that the samples are indeed in the Meissner state. (b) The asymmetry in the normal states seem to show some unusual variance (should be constant) with respect to $\mu_0 H$. On the other hand, these single measurements may not accurately reflect the phase from global fits. The rise of σ with muon energy is due to the expelled flux ($\propto \mu_0 H$) from the neighboring crystals.

10 As may be seen from the table 4.3, a difference of ~ 20 nm exist between the fixed

Table 4.3: Summary of results in $\text{YBa}_2\text{Cu}_3\text{O}_{6.52}$: Measured London penetration depths at 5 K are shown for two models: “phase individual” and “phase shared”, for individual energies. The errors are reported here are just statistical errors. An additional $\sim 2\%$ (~ 2 nm) error is due to uncertainty in stopping distribution. The deadlayer $d \sim 25$ nm, is found from “individual phase” model global fit & is assumed to be the same for “shared phase” model. In the lowest of the fields, 1.5 mT, phase is kept fixed to the measured phase found in the normal state, via field reversing. The lowest penetration depths were obtained for both a and b axis in 1.5 mT external field. The penetration depths at higher fields of 4.6 mT & 7.8 mT include contributions from vortices entering the sample, as may be observed from increasing σ at higher energies.

B (mT)	T (K)	d (nm)	φ ($^\circ$)	λ_a (nm)	λ_b (nm)	$\mathcal{R} \equiv \lambda_a/\lambda_b$	χ^2/DF
1.51	5	23.6(18)	φ_n^a	303.2(87)	233.0(92)	1.30(2)	1.027
4.63	5	26.6(12)	φ_n	330.3(90)	\emptyset	\emptyset	1.147
			24.6(10) ^b	310.0(75)	\emptyset	\emptyset	1.078
7.80	5	23.7(21)	φ_n	\emptyset	616.3(428)	\emptyset	1.098
			26.5(13) ^b	\emptyset	536.6(339)	\emptyset	1.069

^a $\varphi_n = 20.1^\circ$ (fixed)

^b Global phase from “shared phase” analysis.

1 phase and the shared phase models. A single normal state run at 4.6 mT yields a phase of
2 $(23.5 \pm 1.8)^\circ$ & $(0.039 \pm 0.013)^\circ$. This is interesting because shared phase φ seems to suggest
3 a different phase other than the one determined from 1.5 mT set of runs with a reversal of
4 field. From the measured $\lambda_{a,b}$ in table 4.3, it's very likely only minor vortex penetration
5 happened in 4.6 mT set of runs whereas a significant amount of vortices entered in a 7.8 mT
6 set of runs, making the global λ very long. The “effective magnetic penetration” depth is
7 also very sensitive to the muon phase φ , as may be seen in table 4.3. The phase in a “shared,
8 global phase” analysis in this case $\sim 26.5^\circ$ which is also close to the phase found from a
9 single superconducting state analysis in figure 4.22. It is tempting to suggest that the “shared
10 phase model” estimates the true phase. However, as may be seen from figure 4.22, the
11 normal state phases vary little compared to the superconducting state phases and the latter
12 has distinct field dependence, although with bigger error limits. The phases' dependence
13 of magnetic field at higher applied fields, although an interesting one, doesn't affect the
14 determination of absolute penetration depth at 0 K, extrapolated from measurements at 1.5
15 mT.

4.2 Pnictide

17 In this section, measurements of the λ in the Meissner state on a single crystal of $\text{Ba}(\text{Co}_x\text{Fe}_{1-x})_2\text{As}_2$
18 are reported, using a combination of LE- μSR and microwave perturbation. The combination

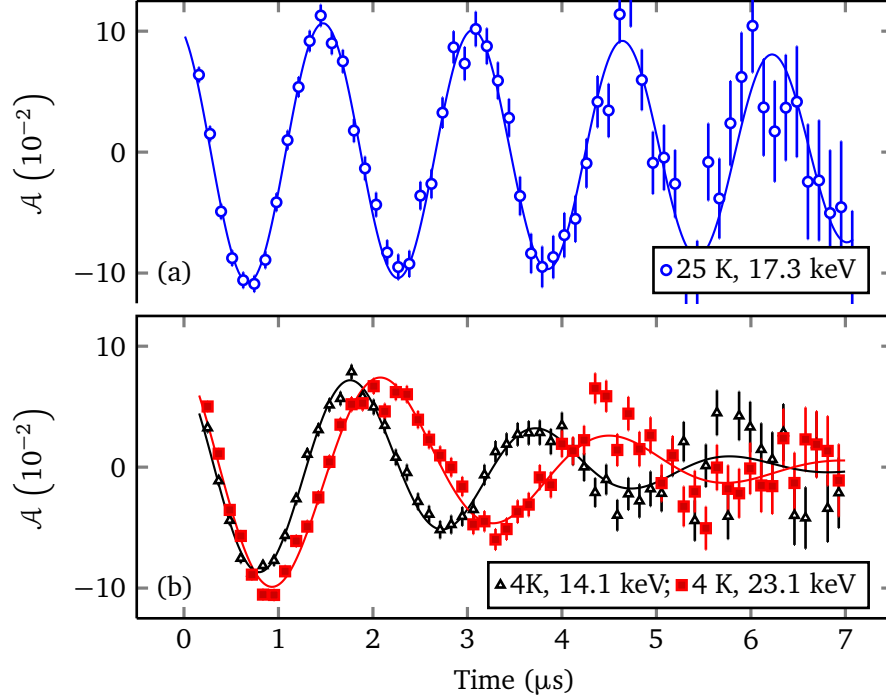


Figure 4.23: Muon precession signals in $\text{Ba}(\text{Co}_x\text{Fe}_{1-x})_2\text{As}_2$ in an applied field of $\mu_0 H = 4.7$ mT. (a) In the normal state at $T = 25$ K. (b) In the superconducting state at $T = 4$ K with $E = 14$ keV and $E = 23$ keV.

of the two techniques allows a precise determination of the T dependence of the magnetic penetration depth, which depends on the symmetry of the superconducting gap.

In the current study we measure the field profile directly on a freshly cleaved surface of $\text{Ba}(\text{Co}_{0.074}\text{Fe}_{0.926})_2\text{As}_2$ using the modified London model as described in the section 4.1.1. The single crystal of optimally-doped $\text{Ba}(\text{Co}_{0.074}\text{Fe}_{0.926})_2\text{As}_2$ was grown using a self-flux method [163]. The crystal was approximately square-shaped with dimensions $5.6 \text{ mm} \times 4.5 \text{ mm} \times 0.3 \text{ mm}$ and exhibited a sharp transition at $T_c = 21.7$ K as measured by SQUID magnetometry. The crystal was cleaved to a thickness of about 0.3 mm under flowing N_2 gas just prior to loading it into the ultra-high-vacuum sample chamber.

Figure 4.23 shows typical μSR precession signals obtained with a small transverse magnetic field applied parallel to the ab face of the crystal. The top panel shows the precession signal in the normal state where the mean internal field is equal to the applied field obtained via fitting the spectrum to a Gaussian. The normal state at $\mu_0 H = 4.7$ mT yields a σ of $0.12 \mu\text{s}^{-1}$. Signals taken below T_c are shown in the bottom panel. All the measurements in the Meissner state were made in **zero field cooled** method as detailed earlier. The reduction of precession frequency, for a higher muon implantation energy, is clearly visible comparing the two spectras (\blacktriangle and \blacksquare) in the figure 4.23. The asymmetry,

1 phase and broadening parameter are shown in the figure 4.24. The asymmetry shows the
 2 usual energy dependent behavior. The $\langle\sigma\rangle$ in the Meissner state of $\mu_0 H = 4.7$ mT is slightly
 3 higher ($0.28(1)\mu s^{-1}$) than that ($0.21(1)\mu s^{-1}$) corresponding to the $\mu_0 H = 2.5$ mT. The
 4 increase of σ with external field were attributed to **bulk magnetization effects**, where flux
 5 expelled from neighboring crystals broaden the effective field, in all three dopings of mosaic
 6 $YBa_2Cu_3O_{6+x}$. The bulk magnetization effect is linearly dependent to the external field.
 7 However, the present Pnictide sample is a single crystal and the average additional (not
 8 accounted for by the stopping distribution $\rho(z)$) broadening $\langle\sigma\rangle$ increases by $\sim 25\%$ with
 9 the approximate doubling of $\mu_0 H$. Also may be noted from the figure 4.24, that σ does not
 10 increase sharply close to the surface as has been seen previously in the two YBCO mosaics
 11 shown in the figures 4.9 and 4.16. This suggests that there is no vortices close to the surface
 12 and yet there is a suppression of superfluid density ~ 15 nm, close to the sample surface, as
 13 may be seen from the curvatures of the global fits in the figure 4.25.

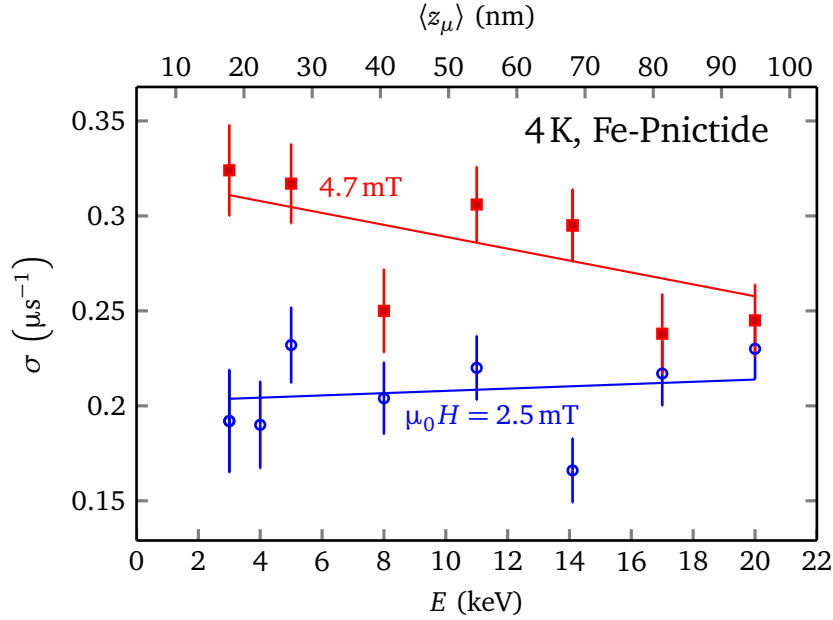


Figure 4.24: Broadening parameter (σ) in $Ba(Co_xFe_{1-x})_2As_2$ in external applied fields of $\mu_0 H = 2.5$ mT and 4.7 mT. The solid lines are guides to the eye.

14 Figure 4.25 shows the average local field $\langle B \rangle$ as a function of the beam energy at $T = 4$ K.
 15 The data are consistent with an exponential decrease as a function of increasing depth or
 16 implantation energy, as expected from a London model. Fit are $\lambda(T = 4 \text{ K}) = 251.7(19)$ nm
 17 and $d = 14.5(9)$ nm where the uncertainties are purely statistical. There is also a 3%
 18 systematic uncertainty in λ due to uncertainties in the muon stopping distribution. Similar
 19 results were obtained at a magnetic field of 2.5 mT, where $\lambda = 252.2(45)$ nm, indicating
 20 there is little field dependence in λ , which is also reflected in the $\langle B \rangle$ in the figure 4.25b.

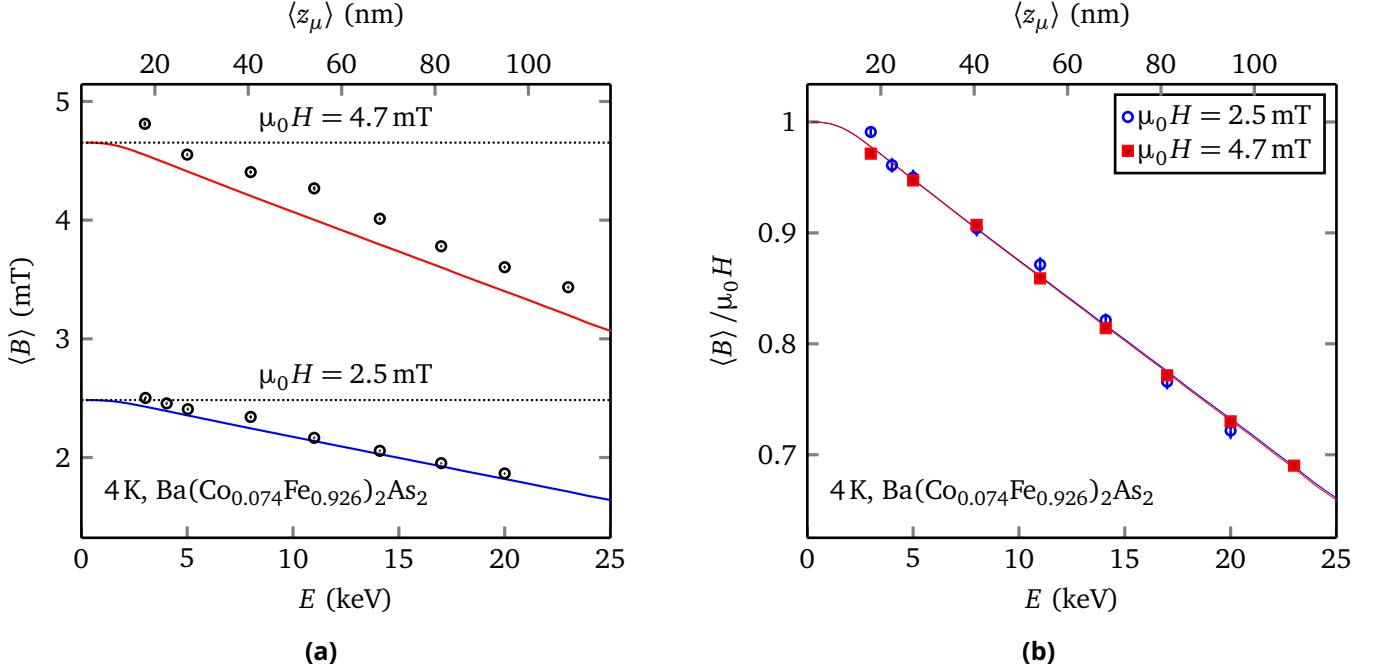


Figure 4.25: The average magnetic field versus the muon energy at $T = 4$ K with a $\mu_0 H = 2.5$ mT applied field. The dotted line indicate the applied field and the solid line indicates a fit to (2.15).

Results of analysis done on two phase (**independent and shared**) models are shown in the table 4.4. Notice that the average of phases from **individual phase model** is within $\sim 1^\circ$, while **shared phase model** yields a $\sim 3^\circ$. Yet with all the model dependence of A_0 , σ and φ , there is only ~ 2 nm difference in the measured λ in the external fields of 2.5 mT and 4.7 mT. This suggests the robustness of our method in obtaining the absolute London penetration depth in Pnictide.

The temperature dependence of λ measured with LE- μ SR (\blacksquare) and with μ W (---), MFM (\circ) and TDR (---) are shown in the figure 4.27. The data points were obtained with a single energy of 21.3 keV with d fixed to the value determined from the global fit at $T = 4$ K (see figure 4.25). Microwave resonance measurements of $\Delta\lambda$ were made on a piece of the same crystal, which was cleaved on both sides. The piece of $\text{Ba}(\text{Co}_{0.074}\text{Fe}_{0.926})_2\text{As}_2$ was mounted on a temperature-controlled sapphire plate, and a 942 MHz loop-gap resonator, described in detail elsewhere[92], was used to obtain $\Delta\lambda$. It is clear the two methods are in excellent agreement below 13 K. One can use the microwave data to extrapolate the 4 K μ SR measurement to obtain $\lambda(0) = 250.2(2.6)$ nm. Above 13 K there is some difference between the two methods which we attribute to a small amount of flux penetration in the μ SR experiment as one approaches T_c and the applied magnetic field of 4.67 mT exceeds H_{c1} . Note the temperature dependence of λ at low temperatures is similar to

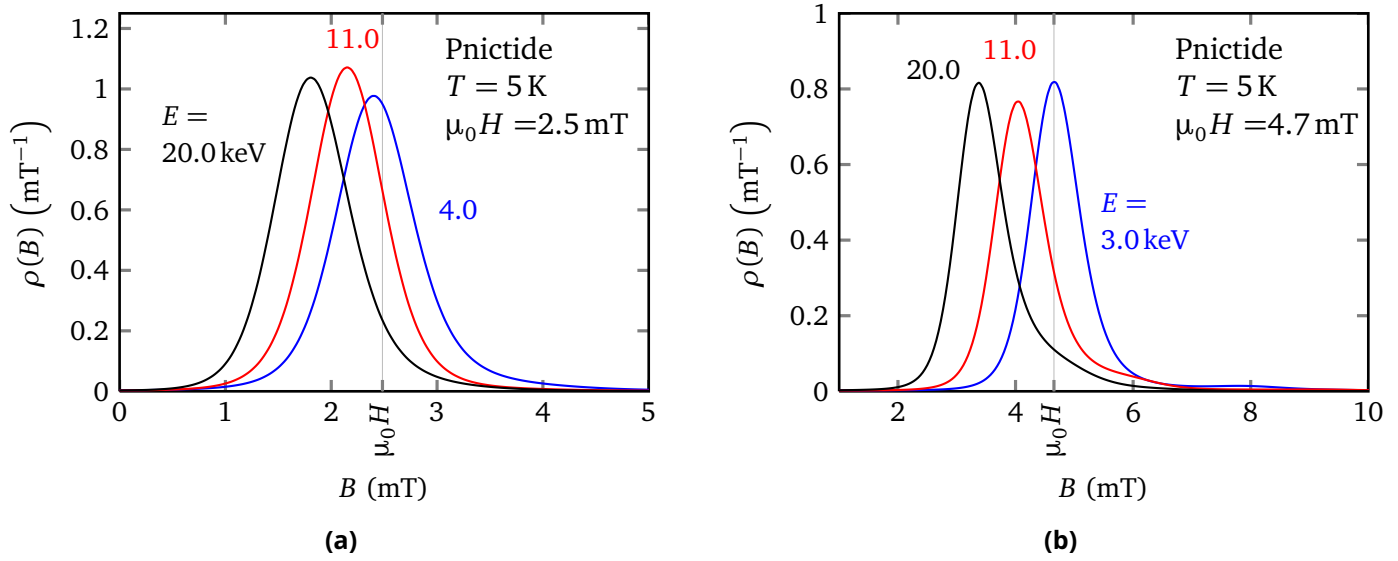


Figure 4.26: Magnetic field distribution as seen by muons at various implantation energies and at $T = 5$ K in an external applied magnetic field ($\mu_0 H$) of 2.5 mT and 4.7 mT, applied parallel to the ab plane.

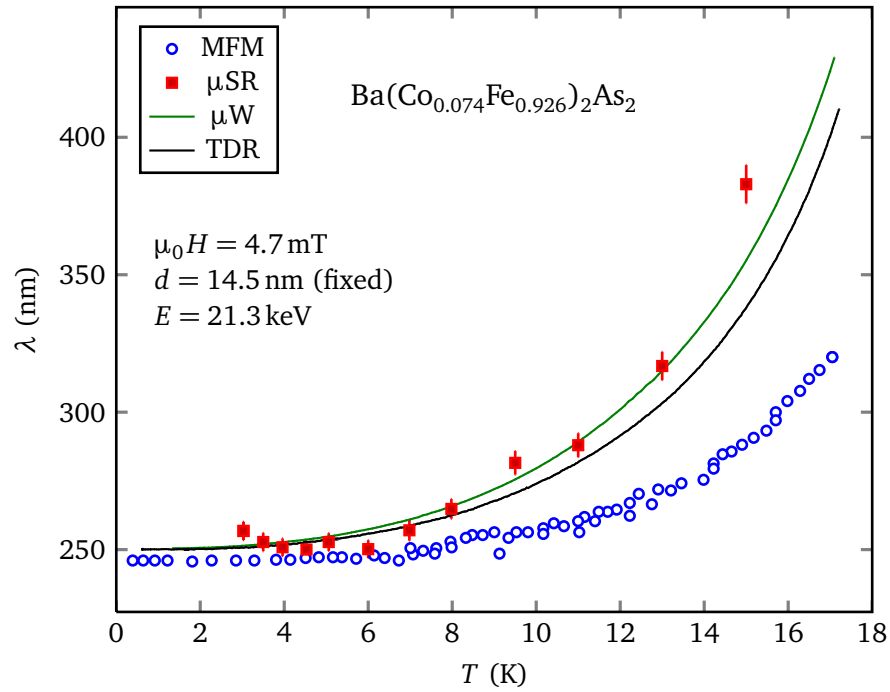


Figure 4.27: The temperature dependence of λ plotted versus $t = T/T_c$. The red squares (■) are measurements of the absolute value of λ from LE- μ SR whereas the green line (—) are from microwave cavity perturbation on a piece of the same crystal shifted to overlap with the LE- μ SR at low temperature. For comparison, we also show recent TDR (—) and MFM (○) results for $\Delta\lambda$, all shifted to agree at $T = 0$.

1 recent TDR results [164] on a thin sample but considerably weaker than previous studies on
 2 thicker crystals [165]. This suggests early studies may have been affected by an anomalous
 3 temperature-dependent field penetration from the c -axis edges. It is interesting to note
 4 that all of these results are stronger than found by MFM also shown in figure 4.27 [166].
 5 One difference is that the present measurements, as well as previous TDR results, measure
 6 an average over the surface whereas MFM is a point-like probe. Such differences between
 7 methods and crystals indicate there are considerable variations in the spectrum of low energy
 8 excitations depending on doping and/or surface quality. Combination of μ W and LE- μ SR
 9 reduces allows one to determine the superfluid density and its variation as a function of
 10 temperature with a high confidence level. The temperature dependence of the superfluid
 11 density normalized to zero temperature is shown in the figure 4.28. Indeed, a similar quality
 12 of fit for low temperatures, which also fits the whole T range, can be obtained using a
 13 phenomenological two-gap s -wave model (“ α model”)[167], where

$$\rho = 1 - x \frac{\delta n_s(\Delta_S(T), T)}{n_s(0)} - (1 - x) \frac{\delta n_s(\Delta_L(T), T)}{n_s(0)} \quad (4.10)$$

and,

$$\begin{aligned} \frac{\delta n_s(\Delta_i(T), T)}{n_s(0)} &= \frac{2}{k_B T} \int_0^\infty f(\varepsilon, \Delta_i(T), T) \\ &\times [1 - f(\varepsilon, \Delta_i(T), T)] d\varepsilon \end{aligned} \quad (4.11)$$

$$\Delta_{L,S}(T) = \Delta_{L,S}(0) \tanh \left(\frac{\pi k_B T_c}{\Delta_{L,S}(0)} \sqrt{a_{L,S} \left(\frac{T_c}{T} - 1 \right)} \right). \quad (4.12)$$

14 Here, the subscript $i = L$ denotes the larger gap which dominates at $T \sim T_c$ where the other
 15 gap $i = S$ dominates at lower temperatures. $f(\varepsilon, \Delta_i(T), T)$ is the Fermi-Dirac distribution
 16 at energy ε and gap Δ . The free parameter $a_{L,S}$ describes phenomenologically the shape
 17 of the gap, e.g. $a_{L,S} \equiv 1$ in the BCS limit; for the small gap we define $a_S = 1$ [168] and
 18 obtain $a_L = 0.83(3)$. We find the large gap $2\Delta_{0,L}/k_B T_c = 3.46(0.10)$ is close to the BCS
 19 weak-coupling limit whereas the small gap $2\Delta_{0,S}/k_B T_c = 1.20(7)$ is much less. These
 20 parameters are also close to those derived from vortex-state μ SR measurements [168].
 21 This is somewhat surprising given the high degree of vortex lattice disorder and the field
 22 induced magnetism[169]. The data were also fit to a self-consistent two-gap model which
 23 takes into account the interaction between bands (“ γ model”)[170]. The quality of the
 24 fit is similar to the phenomenological two-gap model over the full temperature range and
 25 the fitted gap parameters are about 10% larger. The data fit well to a power law form
 26 $\lambda^2(0)/\lambda^2(T) \approx 1 - \alpha(T/T_c)^n$ and are consistent with the superfluid density obtained directly

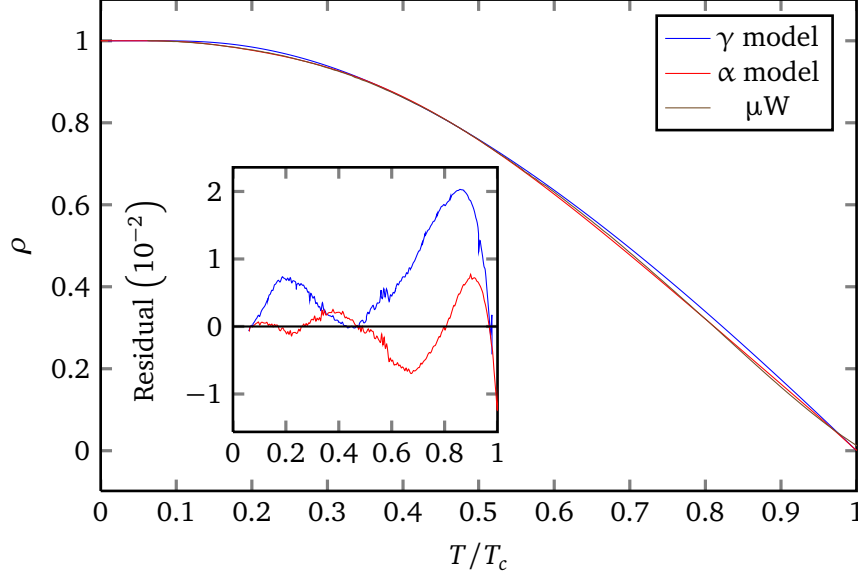


Figure 4.28: The temperature dependence of ρ plotted versus $t = T/T_c$. Solid black (dotted blue) line is a fit to the $\alpha(\gamma)$ model. The dashed curve is the fit to a power law. The inset shows the residuals at low temperature.

1 from LE- μ SR. A fit from base temperature to 12 K yields $n = 2.51(2)$ and $\alpha = 1.39(3)$ K and
2 is only weakly dependent of the fitting range up to 11 K.

3 In conclusion, we have investigated the magnetic field penetration in the Meissner
4 state of freshly-cleaved $\text{Ba}(\text{Co}_{0.074}\text{Fe}_{0.926})_2\text{As}_2$ using both LE- μ SR and microwave cavity
5 perturbation. The absolute value of λ extrapolated to $T = 0$ is 250(8) nm, where most of
6 this uncertainty originates from the muon stopping distribution. There is no evidence of
7 sharp rise in field broadening close to the sample surface. Also weaker field dependence
8 of σ indicates a different origin other than bulk magnetization effect. A two-gap s -wave
9 model and a weak power law model describes the temperature dependence of the superfluid
10 density equally well. The latter model is characteristic of any non s wave gap. There is broad
11 agreement between methods at least at this one Co concentration, except for MFM which
12 probes $\Delta\lambda$ on much smaller length scale.

4.3 Summary Of Results

14 Table 4.5 shows the summary of London penetration depths measurements for three oxygen
15 dopings of $\text{YBa}_2\text{Cu}_3\text{O}_{6+x}$ and on $\text{Ba}(\text{Co}_{0.074}\text{Fe}_{0.926})_2\text{As}_2$. The first number is the measured
16 $\lambda_{a,b}$ extrapolated to $T = 0$ K. The first error is the statistical uncertainty at the temperature
17 $\lambda_{a,b}$ are measured and the second error is the systematic uncertainty. For comparison, $\lambda_{a,b}$
18 values from other measurements are also mentioned In $\text{YBa}_2\text{Cu}_3\text{O}_{6.92}$, “individual phase”
19 and “shared phase” models yield $\lambda_{a,b}$ within a nm of each other and anisotropy is the same
20 for both models. This suggests that there is little (φ) model dependence and accurate values

Table 4.4: Pnictide Two Fields

State	4.7 mT			2.5 mT		
	λ (nm)	$\varphi(^{\circ})$	χ^2/DF	λ (nm)	$\varphi(^{\circ})$	χ^2/DF
Normal	–	25.5(18)	0.932	–	21.4(17)	0.972
Superconducting	252.8(19)	30.9(12) ^a	1.052	254.5(41)	27.6(7) ^a	1.030
	251.7(19)	28.3(6) ^b	1.052	252.2(45)	27.8(5) ^b	1.029

^a Global phase from **shared phase model** analysis.

^b Average of energy specific phases from **individual phase model** analysis.

of $\lambda_{a,b}$ can be obtained by LE- μ SR method. The $\lambda_{a,b}$ obtained here is in good agreement with bulk μ SR measurement in vortex state. It may be noted that conventional μ SR is very different type of measurement. The $\lambda_{a,b}$ in $\text{YBa}_2\text{Cu}_3\text{O}_{6.92}$ obtained here is shorter than that obtained in film. The difference is understandable considering the measurement in film was done at 20 K and the T_c of the film (87.5 K) is less than in crystals possibly indicating a different doping level than in crystals.

Row two of table 4.5 represent our results of $\lambda_{a,b}$ in Ortho-I $\text{YBa}_2\text{Cu}_3\text{O}_{6.998}$, measured at 5 K & 4.7 mT, extrapolated to 0 K by the method described above. In our analysis of “individual phase” model, slightly different $\lambda_{a,b}$ and anisotropy are obtained. However, the measurement of λ is dependent on our ability to determine phase (φ) and frequency (ω) at the same time, which is difficult in lower fields. The lower external field has one significant advantage of reducing the chance of vortex entrance. It may be noted that in $\text{YBa}_2\text{Cu}_3\text{O}_{6.998}$, both 4.7 mT & 9.5 mT measurements were done and the λ_b is about the same in “shared phase” model for 9.5 mT. However, λ at higher external field may have some contribution from vortices and “individual phase” model has significantly lower χ^2/DF . Note that, there is very close agreement between our result and ESR Gd-doped Ortho-I $\text{YBa}_2\text{Cu}_3\text{O}_{6.95}$.

Row three of table 4.5 represent our results of $\lambda_{a,b}$ in $\text{YBa}_2\text{Cu}_3\text{O}_{6.52}$, measured at 5 K & 1.5 mT, extrapolated to 0 K. $\lambda_{a,b}$ ’s were measured in 1.5 mT, 4.7 mT & 7.8 mT, however, there are clear evidences that all external fields except the lowest 1.5 mT introduced vortices. In 1.5 mT external field, a unique determination of phase was made by reversing the field, essentially doubling the range of muon polarization’s oscillation time. Determination of phase is crucial specially at low field as frequency is low and very few full oscillations are observed in muon polarization. It is also interesting that the low temperature linear dependence of λ in $\text{YBa}_2\text{Cu}_3\text{O}_{6.52}$ is an order of magnitude higher than those found in other two oxygen dopings. Note that $\lambda_{a,b}$ in LE- μ SR is significantly longer than that measured in ESR on Gd-doped $\text{YBa}_2\text{Cu}_3\text{O}_{6.52}$. This is surprising considering the other two oxygen dopings have produced very similar results.

On eleventh row (just below the horizontal line) in table 4.5, our measurement of λ_{ab} ,

1 extrapolated to 0 K is shown. Measurements were done in external field of 2.5 mT 4.7
2 mT. The λ_{ab} obtained in for both external field in “shared phase” and “individual phase”
3 models were close to each other within $\sim 4\text{nm}$ i.e, introducing $\sim 2\%$ systematic uncertainty.
4 A two-gap s -wave model describes the temperature dependence of the superfluid density but
5 an equally good fit at low temperatures can be obtained with a weak power-law behavior
6 characteristic of point nodes in the gap function. There is broad agreement between methods
7 at least at this one Co concentration, except for MFM which probes $\Delta\lambda$ on much smaller
8 length scale. For comparison some results from other methods, especially MFM are also
9 shown. Among the MFM results, one of the results with the exact same Co-doping as ours,
10 yield the same λ , however with a much larger uncertainty.

11 Figure 4.29 shows the critical temperature vs effective superfluid density $1/(\lambda_a\lambda_b)^{-1}$. A
12 linear relationship between the two quantities was first suggested by Uemura *et al.* LE- μ SR
13 results significantly differ from a linear relationship. The relationship seems to be sublinear
14 dependence of T_c on λ_{ab}^2 since, for large λ_{ab} , superfluid density will be proportionately
15 smaller and T_c will also be smaller. The linear relationship has been widely regarded as
16 an evidence of order parameter’s phase fluctuation is the parameter responsible for setting
17 T_c . The probable sublinear relationship of T_c on λ_{ab}^2 is an indication of other mechanisms
18 being influential in determining T_c . One of the interesting aspect from figure 4.29 is that
19 optimally doped cuprate & Co-doped pnictide almost falls on a line. Measurements on a
20 range of dopings will be needed to determine the exact relationship of T_c on λ_{ab}^2 .

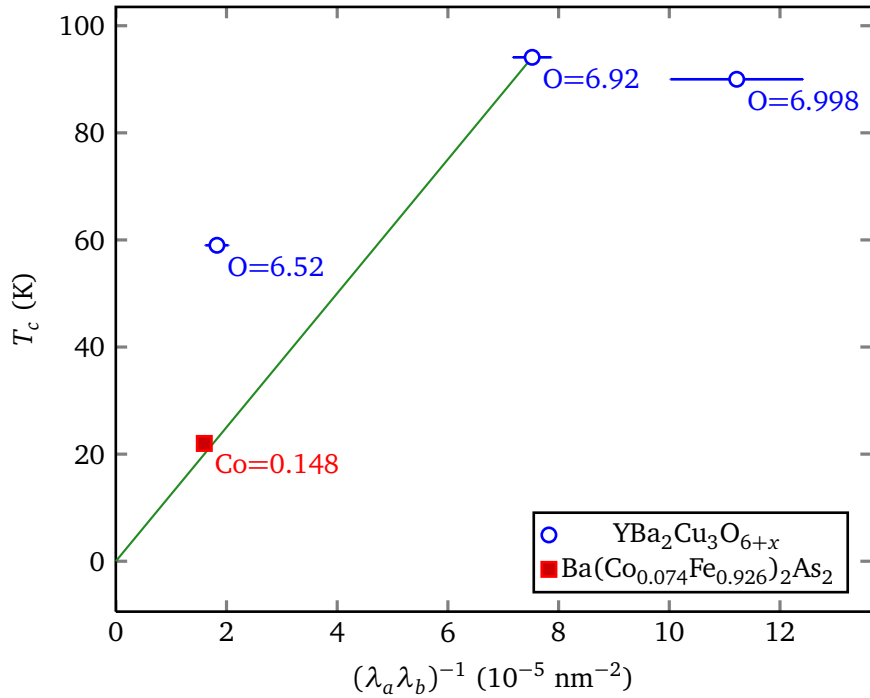


Figure 4.29: T_c vs Lambda-ab.

Table 4.5: Measurements of the absolute value of the magnetic penetration depth ($\lambda_{a,b}$) in $\text{YBa}_2\text{Cu}_3\text{O}_{6.52}$, $\text{YBa}_2\text{Cu}_3\text{O}_{6.92}$ and $\text{YBa}_2\text{Cu}_3\text{O}_{6.998}$. Average magnetic penetration depth $\lambda_{ab} = \sqrt{\lambda_a \lambda_b}$. Vortex state measurements are quoted without systematic errors.

λ_a (nm)	λ_b (nm)	λ_{ab} (nm)	λ_a/λ_b	Comment
$125.6(17) \pm 3$	$105.5(11) \pm 3$	$115.1(10) \pm 3$	1.19(1)	$\text{YBa}_2\text{Cu}_3\text{O}_{6.92}$ ^a
$105.0(39) \pm 3$	$82.0(33) \pm 3$	$92.8(26) \pm 3$	1.28(2)	$\text{YBa}_2\text{Cu}_3\text{O}_{6.998}$ ^a
$261.9(141) \pm 3$	$201.5(104) \pm 3$	$229.7(86) \pm 3$	1.30(2)	$\text{YBa}_2\text{Cu}_3\text{O}_{6.52}$ ^a
		118.0(4)		μSR in vortex state ^b [121]
		146(3)		LE- μSR in thin film at 20 K [162]
160	100	126.5	1.6	IR reflectivity at 10 K [109]
103(8)	80(5)	91(7)	1.29(7)	ESR on $\text{YBa}_2\text{Cu}_3\text{O}_{6.995}$ [171]
202(22)	140(28)	168(19)	1.4(3)	ESR on $\text{YBa}_2\text{Cu}_3\text{O}_{6.52}$ [171]
		150(10)	1.16(2)	μSR at 10 K [172]
		138(5)	1.18(2)	SANS at 10 K [173]
$250.0(26) \pm 5$	$250.0(26) \pm 5$	$250.0(26) \pm 5$	-	$\text{Ba}(\text{Co}_{0.074}\text{Fe}_{0.926})_2\text{As}_2$ ^a
		325(50)	-	MFM [166] in $\text{Ba}(\text{Co}_{0.05}\text{Fe}_{0.95})_2\text{As}_2$
		190(10)	-	Estimated for a range of dopings in $\text{BaCo}_x\text{Fe}_{2-x}\text{As}_2$ [174]
		250(36)	-	MFM [175] on $\text{Ba}(\text{Co}_{0.074}\text{Fe}_{0.926})_2\text{As}_2$

^a This work

^b Conventional μSR

4.4 Discussion On “Deadlayer”

As mentioned in earlier section, a superconductor carries no bulk magnetic field and applied external field decays exponentially inside the sample as it penetrates the surface, according to the London equations. However, as will be shown in a later chapter that, very close to surface, there is a distance over which magnetic field essentially remains constant, an effective dead layer. One possible explanation is surface roughness: small perturbations from a perfect flat geometry. A set of mathematical analysis have been done [176] assuming uneven surface geometry

$$z = \epsilon \cos(\omega_x x) \cos(\omega_y y). \quad (4.13)$$

In these set of analysis, a length of 1 corresponds to a distance of λ in physical units; a frequency ω corresponds to a physical frequency $\tilde{\omega} = \frac{2\pi}{\omega\lambda}$; a field strength of 1 corresponds to the applied external field $|\mathbf{B}_{\text{applied}}|$; roughness amplitude ϵ is believed to be no bigger than (1/10) of λ . A definition of an effective dead layer δ , in dimensionless units, may be adopted as

$$\delta = \int_0^\infty |\mathbf{b}|_{\text{avg}}(s) ds - 1, \quad (4.14)$$

where $\mathbf{b}(s)$ is the depth dependent magnetic field & with the interpretation that for a true dead layer of size δ , the area under $|\mathbf{b}|_{\text{avg}}$ from $s = 0$ to ∞ is precisely $\delta + 1$.

Without loss of generality, sample surface may be modelled as sinusoidal, as more complicated surface may always be Fourier-transformed. For a surface like this, external magnetic field will also be sinusoidal, close to the surface, as depicted in figure 4.30(a).

With an asymptotic expansion of magnetic field $\mathbf{b} \approx \mathbf{b}_0 + \epsilon \mathbf{b}_1 + \epsilon^2 \mathbf{b}_2 + \dots$, where \mathbf{b}_0 is the known solution for a flat surface & \mathbf{b}_i 's are the i -th smaller components M. Lindstrom et al. [176] has found via linear analysis, that average magnetic field $|\mathbf{b}|_{\text{avg}}$ may differ from the London solution by as much as 1%. (figure 4.30). As may be noted from the figure the external field starts decaying before entering the sample, a contrasting scenario with the experimental observation of local fields is possible only inside the surface. Our results suggest that for surfaces with roughness amplitudes in the ballpark of $\lambda/10$ whose spatial frequencies aren't too high, the dead layer is no bigger than $\lambda/20$.

One way the supercurrent at the surface may be suppressed is via vortex penetration which can be facilitated by suppression of d-wave order, i.e a reduction of energy gap near twin or grain boundaries [177, 178]. Also, surface roughness has been attributed to as the cause of vortex nucleation at fields $H \leq H_{c1}$ [179]. Surface vortices have been observed in YBCO in fields as minute as 4G applied parallel to $a - b$ plane [180]. It may be speculated that full-strength external field near the vacuum-surface boundary may be a harbinger of vortices. Also vortex-vortex interaction may be an additional element in the apparent supercurrent suppression. Field inhomogeneities may result from local variations of current

- 1 close to surface due to surface roughness and twin and grain boundaries [181]. Further
- 2 experiments on atomically flat surfaces may help elucidate the origin of the reduction of
- 3 supercurrent in the surface vicinity.

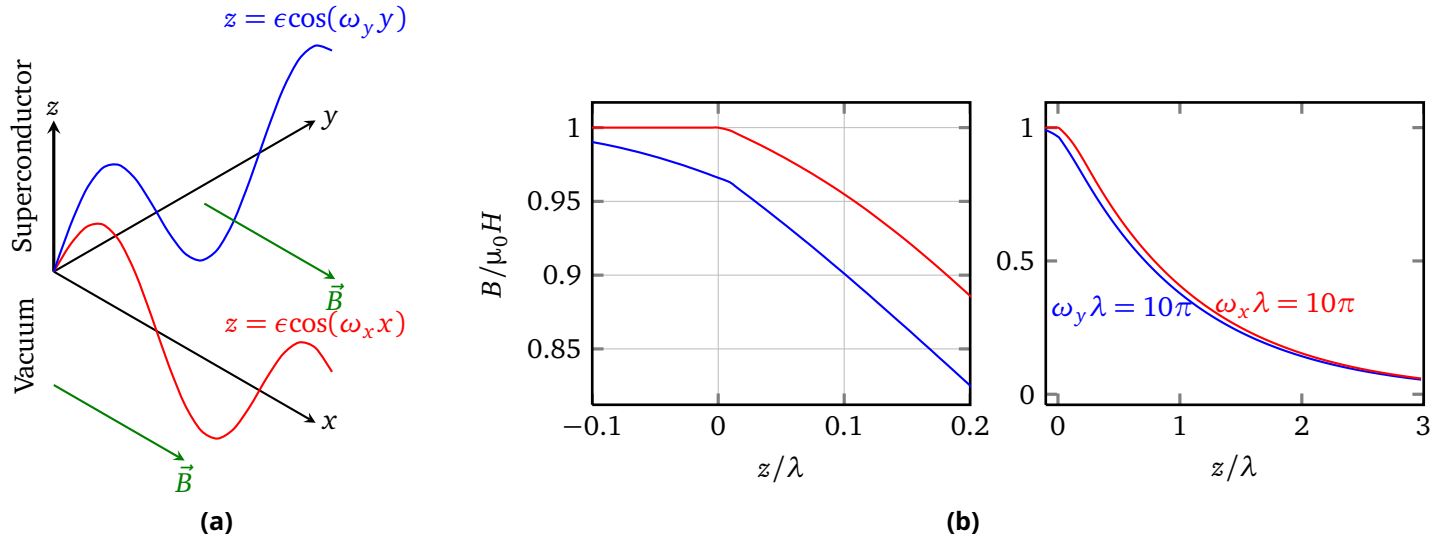


Figure 4.30: (a) A rough surface geometry may be modelled as sinusoidal as any complex surface structure can be Fourier-transformed. External field direction is taken to be along a axis of the crystal. (b) Simulated relative field as it enters the sample.

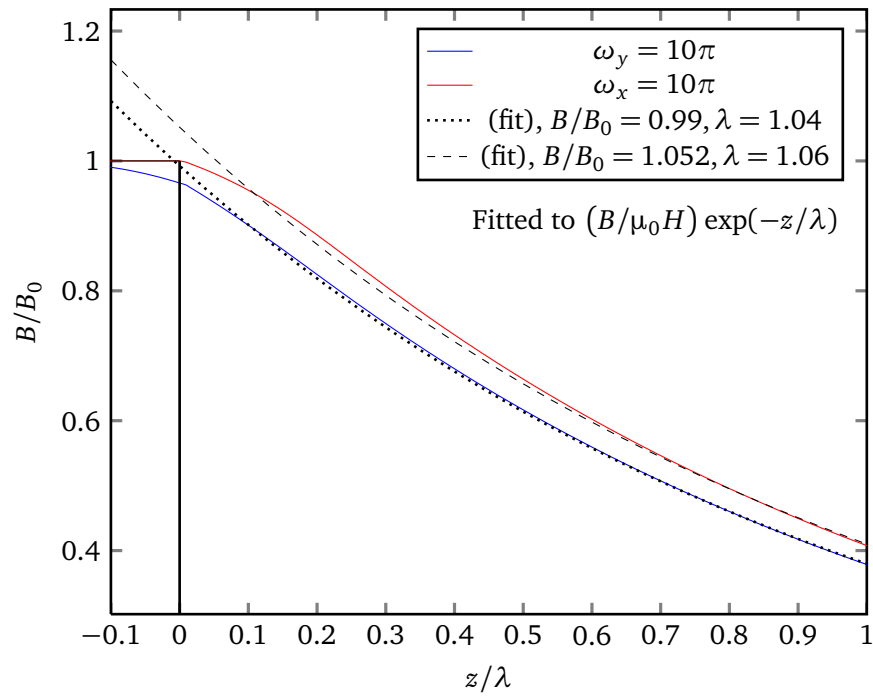


Figure 4.31: Simulated external field fitted to the London model function for the depth range 0 to 10λ . Only the region of $0-\lambda$ is shown.

Conclusions & Outlook

In this thesis, recent measurements of $\lambda_{a,b}$ and the anisotropies ($\equiv \lambda_a/\lambda_b$) have been done for three different oxygen ($x = 6.52, 6.92, 6.998$) dopings of $\text{YBa}_2\text{Cu}_3\text{O}_{6+x}$ and one on $\text{Ba}(\text{Co}_{0.07}\text{Fe}_{0.93})_2\text{As}_2$. The measured values of λ and the anisotropies are considerably different from that of literature, often found with bulk methods. An exponential decay of the magnetic field and corresponding supercurrent density ~ 100 nm inside the crystals. Small deviations from the London model are observed which indicate there is a suppression of the supercurrent density close to the surface. The measured (λ) values are also found to depart substantially from the widely reported Uemura relation ($T_c \propto 1/\lambda_a^2$). Low energy μSR is a very sensitive depth-dependent probe close to the surface of the crystals. Using London model and simulated stopping profiles, one is able to extract a very precise measure of London penetration depth as a function of observable parameters such doping, temperature, impurity. The measured penetration depths slightly depend on the exact phase models used, as is the case with any model. However the uncertainties due to an exact determination of phase are included as systematic errors in the final results. In fields on the order of ~ 10 mT, measured London depths have little model dependence compared to lower fields such as 5 mT or 1.5 mT. This is easily understood as we note that there are fewer full oscillations in asymmetry spectrum for lower fields and phase & frequency ($\gamma_\mu B$) becomes correlated. However lower fields were required for one oxygen doping in $\text{YBa}_2\text{Cu}_3\text{O}_{6+x}$ due to vortex entrance at external fields ~ 4.6 mT. The measured $\lambda_{a,b}$ have been found in YBCO good agreement with ESR and conventional μSR , with the exception of considerable difference oxygen doping 6.52. Low temperature linear dependence of $\lambda_{a,b}$ have also been observed in all the oxygen dopings in $\text{YBa}_2\text{Cu}_3\text{O}_{6+x}$, which is an important signature for a d -wave superconducting gap. One important parameter, penetration depth anisotropy \mathcal{R} , is also determined for all the dopings of YBCO. The anisotropy, being the ratio of λ in both directions, are determined with more accuracy than the penetration depths.

Pnictide penetration depth is also in very good agreement with a recent MFM (with a larger error) determination of λ and is somewhere between the earlier estimates. The temperature dependence of the superfluid density is obtained by combining low energy μSR and microwave resonance and a weak power law behavior for the superfluid density is found at low temperature while a two-gap model fits the whole temperature range.

Bibliography

- 1 Kiefl, R. F., et al. [Direct measurement of the London penetration depth in \$\text{YBa}_2\text{Cu}_3\text{O}_{6.92}\$ using low-energy \$\mu\text{SR}\$](#) . *Phys. Rev. B*, **81**, 180502 (2010). \diamond Cited on page iii.
- 2 Ofer, O., et al. [Absolute value and temperature dependence of the magnetic penetration depth in \$\text{Ba}\(\text{Co}_{0.074}\text{Fe}_{0.926}\)_2\text{As}_2\$](#) . *Phys. Rev. B*, **85**, 060506 (2012). \diamond Cited on page iii.
- 3 Onnes, H. K. *Commun. Phys. Lab. Univ. Leiden*, **120b,122b,124c** (1911). \diamond Cited on page 1.
- 4 Onnes, H. K. The resistance of pure mercury at helium temperatures. *Comm. Leiden.*, **120 b** (1911). \diamond Cited on page 1.
- 5 Meissner, W. and Oschenfel, R. *Naturwiss.*, **21** (1933). \diamond Cited on page 1.
- 6 London, F. and London, H. *Proc. R. Soc. London*, **A149** (1935). \diamond Cited on page 1.
- 7 Ginzburg, V. L. and Landau, L. D. On the Theory of superconductivity. *Zh. Eksp. Teor. Fiz.*, **20**, 1064–1082 (1950). \diamond Cited on page 1.
- 8 Bardeen, J., Cooper, L. N., and Schrieffer, J. R. [Theory of Superconductivity](#). *Phys. Rev.*, **108**, 1175–1204 (1957). \diamond Cited on page 3.
- 9 Bardeen, J., Cooper, L. N., and Schrieffer, J. R. [Microscopic Theory of Superconductivity](#). *Phys. Rev.*, **106**, 162–164 (1957). \diamond Cited on page 3.
- 10 Cooper, L. N. [Bound Electron Pairs in a Degenerate Fermi Gas](#). *Phys. Rev.*, **104**, 1189–1190 (1956). \diamond Cited on pages 3 & 16.
- 11 Bednorz, J. G. and Müller, K. A. [Possible high \$T_c\$ superconductivity in the Ba-La-Cu-O system](#). *Zeitschrift für Physik B Condensed Matter*, **64**, 189–193 (1986). \diamond Cited on page 3.
- 12 Wu, M. K., Ashburn, J. R., Torng, C. J., Hor, P. H., Meng, R. L., Gao, L., Huang, Z. J., Wang, Y. Q., and Chu, C. W. [Superconductivity at 93 K in a new mixed-phase Y-Ba-Cu-O compound system at ambient pressure](#). *Phys. Rev. Lett.*, **58**, 908–910 (1987). \diamond Cited on page 3.
- 13 Elert, G. (2002), [Highest critical temperature superconductor](#). [Online; accessed 5-February-2012]. \diamond Cited on page 4.
- 14 Blatter, G., Feigel'man, M. V., Geshkenbein, V. B., Larkin, A. I., and Vinokur, V. M. [Vortices in high-temperature superconductors](#). *Rev. Mod. Phys.*, **66**, 1125–1388 (1994). \diamond Cited on page 3.

- 1 **15** Sachdev, S. and Zhang, S.-C. [Tuning Order in Cuprate Superconductors](#). *Science*, **295**,
2 452–454 (2002). ◇ Cited on page 5.
- 3 **16** Hill, R. W., Proust, C., Taillefer, L., Fournier, P., and Greene, R. L. [Breakdown of
4 Fermi-liquid theory in a copper-oxide superconductor](#). *Nature*, **414**, 711–715 (2001).
5 ◇ Cited on page 6.
- 6 **17** Capponi, J. J., Chaillout, C., Hewat, A. W., Lejay, P., Marezio, M., Nguyen, N., Raveau,
7 B., Soubeyroux, J. L., Tholence, J. L., and Tournier, R. [Structure of the 100 K Su-
8 perconductor \$\text{YBa}_2\text{Cu}_3\text{O}_7\$ between \(5 - 300\) K by Neutron Powder Diffraction](#). *EPL*
9 (*Europhysics Letters*), **3**, 1301 (1987). ◇ Cited on page 7.
- 10 **18** Momma, K. and Izumi, F. [VESTA: a three-dimensional visualization system for electronic
11 and structural analysis](#). *Journal of Applied Crystallography*, **41**, 653–658 (2008). ◇
12 Cited on page 7.
- 13 **19** Keren, A., Le, L. P., Luke, G. M., Sternlieb, B. J., Wu, W. D., Uemura, Y. J., Tajima, S., and
14 Uchida, S. [Muon-spin-rotation measurements in infinite-layer and infinite-chain cuprate
15 antiferromagnets: \$\text{Ca}_{0.86}\text{Sr}_{0.14}\text{CuO}_2\$ and \$\text{Sr}_2\text{CuO}_3\$](#) . *Phys. Rev. B*, **48**, 12926–12935
16 (1993). ◇ Cited on pages 6 & 13.
- 17 **20** Tallon, J. L., Bernhard, C., Shaked, H., Hitterman, R. L., and Jorgensen, J. D. [Generic
18 superconducting phase behavior in high- \$T_c\$ cuprates: \$T_c\$ variation with hole concen-
19 tration in \$\text{YBa}_2\text{Cu}_3\text{O}_{7-\delta}\$](#) . *Phys. Rev. B*, **51**, 12911–12914 (1995). ◇ Cited on page
20 8.
- 21 **21** Lanzara, A., et al. [Evidence for ubiquitous strong electron-phonon coupling in high-
22 temperature superconductors](#). *Nature*, **412**, 510–514 (2001). ◇ Cited on page 8.
- 23 **22** Devereaux, T. P., Cuk, T., Shen, Z.-X., and Nagaosa, N. [Anisotropic electron-phonon
24 interaction in the cuprates](#). *Phys. Rev. Lett.*, **93**, 117004 (2004). ◇ Cited on page 8.
- 25 **23** Bohnen, K.-P., Heid, R., and Krauss, M. [Phonon dispersion and electron-phonon inter-
26 action for \$\text{YBa}_2\text{Cu}_3\text{O}_7\$ from first-principles calculations](#). *EPL (Europhysics Letters)*, **64**,
27 104 (2003). ◇ Cited on page 8.
- 28 **24** Falter, C. and Hoffmann, G. A. [Nonlocal electron-phonon coupling of ionic charge-
29 fluctuation type and phonon anomalies in high-temperature superconductors](#). *Phys.*
30 *Rev. B*, **64**, 054516 (2001). ◇ Cited on page 8.
- 31 **25** Chung, J.-H., et al. [In-plane anisotropy and temperature dependence of oxygen phonon
32 modes in \$\text{YBa}_2\text{Cu}_3\text{O}_{6.95}\$](#) . *Phys. Rev. B*, **67**, 014517 (2003). ◇ Cited on page 8.
- 33 **26** Reznik, D., Pintschovius, L., Ito, M., Iikubo, S., Sato, M., Goka, H., Fujita, M., Yamada,
34 K., Gu, G. D., and Tranquada, J. M. [Electron-phonon coupling reflecting dynamic charge
35 inhomogeneity in copper oxide superconductors](#). *Nature*, **440**, 1170–1173 (2006). ◇
36 Cited on page 8.
- 37 **27** Giustino, F., Cohen, M. L., and Louie, S. G. [Small phonon contribution to the photoe-
38 mission kink in the copper oxide superconductors](#). *Nature*, **452**, 975–978 (2008). ◇
39 Cited on page 8.

- 1 **28** Anderson, P. W. [The Resonating Valence Bond State in \$\text{La}_2\text{CuO}_4\$ and Superconductivity.](#) *Science*, **235**, 1196–1198 (1987). ◇ Cited on page 8.
- 2
- 3 **29** Anderson, P. W. [Resonating valence bonds: A new kind of insulator?](#) *Materials Research*
4 *Bulletin*, **8**, 153 – 160 (1973). ◇ Cited on page 9.
- 5 **30** Anderson, P. W., Lee, P. A., Randeria, M., Rice, T. M., Trivedi, N., and Zhang, F. C. [The](#)
6 [physics behind high-temperature superconducting cuprates: the ‘plain vanilla’ version](#)
7 [of RVB.](#) *Journal of Physics: Condensed Matter*, **16**, R755 (2004). ◇ Cited on page 9.
- 8 **31** Baskaran, G., Zou, Z., and Anderson, P. W. [The resonating valence bond state and](#)
9 [high- \$T_c\$ superconductivity – A mean field theory.](#) *Solid State Communications*, **63**, 973
10 – 976 (1987). ◇ Cited on page 9.
- 11 **32** Vaknin, D., Sinha, S. K., Moncton, D. E., Johnston, D. C., Newsam, J. M., Safinya, C. R.,
12 and King, H. E. [Antiferromagnetism in \$\text{La}_2\text{CuO}_{4-y}\$.](#) *Phys. Rev. Lett.*, **58**, 2802–2805
13 (1987). ◇ Cited on pages 9 & 12.
- 14 **33** Tranquada, J. M., et al. [Neutron-Diffraction Determination of Antiferromagnetic Struc-](#)
15 [ture of Cu Ions in \$\text{YBa}_2\text{Cu}_3\text{O}_{6+x}\$ with \$x = 0.0\$ and \$0.15\$.](#) *Phys. Rev. Lett.*, **60**, 156–159
16 (1988). ◇ Cited on page 9.
- 17 **34** Moudden, A. H., Shirane, G., Tranquada, J. M., Birgeneau, R. J., Endoh, Y., Yamada, K.,
18 Hidaka, Y., and Murakami, T. [Antiferromagnetic ordering of Cu ions in \$\text{NdBa}_2\text{Cu}_3\text{O}_{6.1}\$.](#)
19 *Phys. Rev. B*, **38**, 8720–8723 (1988). ◇ Cited on pages 9 & 13.
- 20 **35** Shirane, G., Endoh, Y., Birgeneau, R. J., Kastner, M. A., Hidaka, Y., Oda, M., Suzuki,
21 M., and Murakami, T. [Two-dimensional antiferromagnetic quantum spin-fluid state in](#)
22 [\$\text{La}_2\text{CuO}_4\$.](#) *Phys. Rev. Lett.*, **59**, 1613–1616 (1987). ◇ Cited on pages 9 & 13.
- 23 **36** Endoh, Y., et al. [Static and dynamic spin correlations in pure and doped \$\text{La}_2\text{CuO}_4\$.](#) *Phys.*
24 *Rev. B*, **37**, 7443–7453 (1988). ◇ Cited on page 9.
- 25 **37** Niedermayer, C., Bernhard, C., Blasius, T., Golnik, A., Moodenbaugh, A., and Bud-
26 nick, J. I. [Common Phase Diagram for Antiferromagnetism in \$\text{La}_{2-x}\text{Sr}_x\text{CuO}_4\$ and](#)
27 [\$\text{Y}_{1-x}\text{Ca}_x\text{Ba}_2\text{Cu}_3\text{O}_6\$ as Seen by Muon Spin Rotation.](#) *Phys. Rev. Lett.*, **80**, 3843–3846
28 (1998). ◇ Cited on page 9.
- 29 **38** Hussey, N. E. [Low-energy quasiparticles in high- \$T_c\$ cuprates.](#) *Advances in Physics*, **51**,
30 1685–1771 (2002). ◇ Cited on page 9.
- 31 **39** Hussey, N. E., Abdel-Jawad, M., Carrington, A., Mackenzie, A. P., and Balicas, L. [A coher-](#)
32 [ent three-dimensional Fermi surface in a high-transition-temperature superconductor.](#)
33 *Nature*, **425**, 814–817 (2003). ◇ Cited on page 9.
- 34 **40** Yamaji, K. [On the Angle Dependence of the Magnetoresistance in Quasi-Two-](#)
35 [Dimensional Organic Superconductors.](#) *Journal of the Physical Society of Japan*, **58**,
36 1520–1523 (1989). ◇ Cited on page 9.
- 37 **41** Tanaka, K., et al. [Distinct Fermi-Momentum-Dependent Energy Gaps in Deeply Under-](#)
38 [doped \$\text{Bi2212}\$.](#) *Science*, **314**, 1910–1913 (2006). ◇ Cited on pages 9 & 10.

- 42 Audouard, A., Jaudet, C., Vignolles, D., Liang, R., Bonn, D. A., Hardy, W. N., Taillefer, L., and Proust, C. [Multiple Quantum Oscillations in the de Haas-van Alphen Spectra of the Underdoped High-Temperature Superconductor \$\text{YBa}_2\text{Cu}_3\text{O}_{6.5}\$](#) . *Phys. Rev. Lett.*, **103**, 157003 (2009). \diamond Cited on page 10.
- 43 Ding, H., Yokoya, T., Campuzano, J. C., Takahashi, T., Randeria, M., Norman, M. R., Mochiku, T., Kadowaki, K., and Giapintzakis, J. [Spectroscopic evidence for a pseudogap in the normal state of underdoped high- \$T_c\$ superconductors](#). *Nature*, **382**, 51–54 (1996). \diamond Cited on page 10.
- 44 Daou, R., et al. [Broken rotational symmetry in the pseudogap phase of a high- \$T_c\$ superconductor](#). *Nature*, **463**, 519–522 (2010). \diamond Cited on page 10.
- 45 Timusk, T. and Statt, B. [The pseudogap in high-temperature superconductors: an experimental survey](#). *Reports on Progress in Physics*, **62**, 61 (1999). \diamond Cited on page 10.
- 46 Loeser, A. G., Shen, Z.-X., Dessau, D. S., Marshall, D. S., Park, C. H., Fournier, P., and Kapitulnik, A. [Excitation Gap in the Normal State of Underdoped \$\text{Bi}_2\text{Sr}_2\text{CaCu}_2\text{O}_{8+\delta}\$](#) . *Science*, **273**, 325–329 (1996). \diamond Cited on page 10.
- 47 Laughlin, R. B. [PERSPECTIVES A critique of two metals](#). *Advances in Physics*, **47**, 943 – 958 (1998). \diamond Cited on page 10.
- 48 Sachdev, S. [Quantum Criticality: Competing Ground States in Low Dimensions](#). *Science*, **288**, 475–480 (2000). \diamond Cited on page 10.
- 49 Tallon, J. and Loram, J. [The doping dependence of \$T^*\$ - what is the real high- \$T_c\$ phase diagram?](#) *PHYSICA C*, **349**, 53–68 (2001). \diamond Cited on page 10.
- 50 Li, Y., Baledent, V., Barisic, N., Cho, Y., Fauque, B., Sidis, Y., Yu, G., Zhao, X., Bourges, P., and Greven, M. [Unusual magnetic order in the pseudogap region of the superconductor \$\text{HgBa}_2\text{CuO}_{4+\delta}\$](#) . *Nature*, **455**, 372–375 (2008). \diamond Cited on page 10.
- 51 Varma, C. M. [Non-Fermi-liquid states and pairing instability of a general model of copper oxide metals](#). *Phys. Rev. B*, **55**, 14554–14580 (1997). \diamond Cited on page 10.
- 52 Varma, C. M. [Pseudogap Phase and the Quantum-Critical Point in Copper-Oxide Metals](#). *Phys. Rev. Lett.*, **83**, 3538–3541 (1999). \diamond Cited on page 10.
- 53 Gurvitch, M. and Fiory, A. T. [Resistivity of \$\text{La}_{1.825}\text{Sr}_{0.175}\text{CuO}_4\$ and \$\text{YBa}_2\text{Cu}_3\text{O}_7\$ to 1100 K: Absence of saturation and its implications](#). *Phys. Rev. Lett.*, **59**, 1337–1340 (1987). \diamond Cited on page 10.
- 54 Thomas, G. A., Orenstein, J., Rapkine, D. H., Capizzi, M., Millis, A. J., Bhatt, R. N., Schneemeyer, L. F., and Waszczak, J. V. [\$\text{Ba}_2\text{YCu}_3\text{O}_{7-\delta}\$: Electrodynamics of Crystals with High Reflectivity](#). *Phys. Rev. Lett.*, **61**, 1313–1316 (1988). \diamond Cited on page 10.
- 55 Gurvitch, M., Valles, J. M., Cucolo, A. M., Dynes, R. C., Garno, J. P., Schneemeyer, L. F., and Waszczak, J. V. [Reproducible tunneling data on chemically etched single crystals of \$\text{YBa}_2\text{Cu}_3\text{O}_7\$](#) . *Phys. Rev. Lett.*, **63**, 1008–1011 (1989). \diamond Cited on page 10.

- 1 56 Anderson, P. W. [The ‘strange metal’ is a projected Fermi liquid with edge singularities.](#) *Nat Phys*, **2**, 626–630 (2006). ◇ Cited on page 10.
- 3 57 Varma, C. M., Littlewood, P. B., Schmitt-Rink, S., Abrahams, E., and Ruckenstein, A. E. [Phenomenology of the normal state of Cu-O high-temperature superconductors.](#) *Phys. Rev. Lett.*, **63**, 1996–1999 (1989). ◇ Cited on page 10.
- 6 58 Gough, C. E., Colclough, M. S., Forgan, E. M., Jordan, R. G., Keene, M., Muirhead, C. M., Rae, A. I. M., Thomas, N., Abell, J. S., and Sutton, S. [Flux quantization in a high- \$T_c\$ superconductor.](#) *Nature*, **326**, 855–855 (1987). ◇ Cited on page 10.
- 9 59 Tsuei, C. C., Kirtley, J. R., Chi, C. C., Yu-Jahnes, L. S., Gupta, A., Shaw, T., Sun, J. Z., and Ketchen, M. B. [Pairing Symmetry and Flux Quantization in a Tricrystal Superconducting Ring of \$\text{YBa}_2\text{Cu}_3\text{O}_{7-\delta}\$.](#) *Phys. Rev. Lett.*, **73**, 593–596 (1994). ◇ Cited on page 10.
- 12 60 Gammel, P. L., Bishop, D. J., Dolan, G. J., Kwo, J. R., Murray, C. A., Schneemeyer, L. F., and Waszczak, J. V. [Observation of Hexagonally Correlated Flux Quanta In \$\text{YBa}_2\text{Cu}_3\text{O}_7\$.](#) *Phys. Rev. Lett.*, **59**, 2592–2595 (1987). ◇ Cited on page 10.
- 15 61 Ren, Z. A., Yang, J., Lu, W., Yi, W., Che, G. C., Dong, X. L., Sun, L. L., and Zhao, Z. X. [Superconductivity at 52 K in iron based F doped layered quaternary compound \$\text{Pr}\[\text{O}_{1-x}\text{F}_x\]\text{FeAs}\$.](#) *Materials Research Innovations*, **12**, 105–106 (2008). ◇ Cited on page 10.
- 19 62 Chen, G. F., Li, Z., Wu, D., Li, G., Hu, W. Z., Dong, J., Zheng, P., Luo, J. L., and Wang, N. L. [Superconductivity at 41 K and Its Competition with Spin-Density-Wave Instability in Layered \$\text{CeO}_{1-x}\text{F}_x\text{FeAs}\$.](#) *Phys. Rev. Lett.*, **100**, 247002 (2008). ◇ Cited on page 10.
- 22 63 Chen, X. H., Wu, T., Wu, G., Liu, R. H., Chen, H., and Fang, D. F. [Superconductivity at 43 K in \$\text{SmFeAsO}_{1-x}\text{F}_x\$.](#) *Nature*, **453**, 761–762 (2008). ◇ Cited on page 10.
- 24 64 Kamihara, Y., Watanabe, T., Hirano, M., and Hosono, H. [Iron-Based Layered Superconductor \$\text{La}\[\text{O}_{1-x}\text{F}_x\]\text{FeAs}\$ \(\$x = 0.05\text{--}0.12\$ \) with \$T_c = 26\$ K.](#) *Journal of the American Chemical Society*, **130**, 3296–3297 (2008). ◇ Cited on pages 10 & 11.
- 27 65 Kreyssig, A., et al. [Pressure-induced volume-collapsed tetragonal phase of \$\text{CaFe}_2\text{As}_2\$ as seen via neutron scattering.](#) *Phys. Rev. B*, **78**, 184517 (2008). ◇ Cited on page 10.
- 29 66 Huang, Q., Qiu, Y., Bao, W., Green, M. A., Lynn, J. W., Gasparovic, Y. C., Wu, T., Wu, G., and Chen, X. H. [Neutron-Diffraction Measurements of Magnetic Order and a Structural Transition in the Parent \$\text{BaFe}_2\text{As}_2\$ Compound of FeAs-Based High-Temperature Superconductors.](#) *Phys. Rev. Lett.*, **101**, 257003 (2008). ◇ Cited on page 11.
- 33 67 Rotter, M., Tegel, M., and Johrendt, D. [Superconductivity at 38 K in the Iron Arsenide \$\(\text{Ba}_{1-x}\text{K}_x\)\text{Fe}_2\text{As}_2\$.](#) *Phys. Rev. Lett.*, **101**, 107006 (2008). ◇ Cited on page 11.
- 35 68 de la Cruz, C., et al. [Magnetic order close to superconductivity in the iron-based layered \$\text{LaO}_{1-x}\text{F}_x\text{FeAs}\$ systems.](#) *Nature*, **453**, 899–902 (2008). ◇ Cited on pages 11 & 12.
- 37 69 Klauss, H.-H., et al. [Commensurate Spin Density Wave in \$\text{LaFeAsO}\$: A Local Probe Study.](#) *Phys. Rev. Lett.*, **101**, 077005 (2008). ◇ Cited on page 11.

- 1 **70** Krellner, C., Caroca-Canales, N., Jesche, A., Rosner, H., Ormeci, A., and Geibel, C.
2 [Magnetic and structural transitions in layered iron arsenide systems: \$\text{AFe}_2\text{As}_2\$ versus](#)
3 [\$\text{RFeAsO}\$.](#) *Phys. Rev. B*, **78**, 100504 (2008). \diamond Cited on page 11.
- 4 **71** Jesche, A., et al. [Strong coupling between magnetic and structural order parameters in](#)
5 [\$\text{SrFe}_2\text{As}_2\$.](#) *Phys. Rev. B*, **78**, 180504 (2008). \diamond Cited on page 11.
- 6 **72** Goldman, A. I., Argyriou, D. N., Ouladdiaf, B., Chatterji, T., Kreyssig, A., Nandi, S.,
7 Ni, N., Bud'ko, S. L., Canfield, P. C., and McQueeney, R. J. [Lattice and magnetic](#)
8 [instabilities in \$\text{CaFe}_2\text{As}_2\$: A single-crystal neutron diffraction study.](#) *Phys. Rev. B*, **78**,
9 100506 (2008). \diamond Cited on page 11.
- 10 **73** Gen-Fu, C., Zheng, L., Gang, L., Wan-Zheng, H., Jing, D., Jun, Z., Xiao-Dong, Z., Ping,
11 Z., Nan-Lin, W., and Jian-Lin, L. [Superconductivity in Hole-Doped \$\(\text{Sr}_{1-x}\text{K}_x\)\text{Fe}_2\text{As}_2\$.](#)
12 *Chinese Physics Letters*, **25**, 3403 (2008). \diamond Cited on page 11.
- 13 **74** Sasmal, K., Lv, B., Lorenz, B., Guloy, A. M., Chen, F., Xue, Y.-Y., and Chu, C.-W. [Super-](#)
14 [conducting Fe-Based Compounds \$\(\text{A}_{1-x}\text{Sr}_x\)\text{Fe}_2\text{As}_2\$ with \$\text{A} = \text{K}\$ and \$\text{Cs}\$ with Transition](#)
15 [Temperatures up to 37 K.](#) *Phys. Rev. Lett.*, **101**, 107007 (2008). \diamond Cited on page 11.
- 16 **75** Ren, Z.-A., et al. [Superconductivity and phase diagram in iron-based arsenic-oxides](#)
17 [\$\text{ReFeAsO}_{1-\delta}\$ \(\$\text{Re} = \text{rare-earth metal}\$ \) without fluorine doping.](#) *EPL (Europhysics*
18 *Letters)*, **83**, 17002 (2008). \diamond Cited on page 11.
- 19 **76** Kito, H., Eisaki, H., and Iyo, A. [Superconductivity at 54K in F-Free \$\text{NdFeAsO}_{1-y}\$.](#) *Journal*
20 *of the Physical Society of Japan*, **77**, 063707 (2008). \diamond Cited on page 11.
- 21 **77** Tranquada, J. M. [Modulated superfluid density in an iron-pnictide superconductor.](#)
22 *Physics*, **3**, 41 (2010). \diamond Cited on page 12.
- 23 **78** Nandi, S., et al. [Anomalous Suppression of the Orthorhombic Lattice Distortion in](#)
24 [Superconducting \$\text{Ba}\(\text{Fe}_{1-x}\text{Co}_x\)_2\text{As}_2\$ Single Crystals.](#) *Phys. Rev. Lett.*, **104**, 057006
25 (2010). \diamond Cited on page 12.
- 26 **79** Dong, J., et al. [Competing orders and spin-density-wave instability in \$\text{La}\(\text{O}_{1-x}\text{F}_x\)\text{FeAs}\$.](#)
27 *EPL (Europhysics Letters)*, **83**, 27006 (2008). \diamond Cited on page 12.
- 28 **80** Boeri, L., Dolgov, O. V., and Golubov, A. A. [Is \$\text{LaFeAsO}_{1-x}\text{F}_x\$ an Electron-Phonon](#)
29 [Superconductor?](#) *Phys. Rev. Lett.*, **101**, 026403 (2008). \diamond Cited on page 12.
- 30 **81** Mazin, I. and Schmalian, J. [Pairing symmetry and pairing state in ferropnictides:](#)
31 [Theoretical overview.](#) *Physica C: Superconductivity*, **469**, 614 – 627 (2009). \diamond Cited
32 on pages 12 & 22.
- 33 **82** D.J. and Singh [Electronic structure of Fe-based superconductors.](#) *Physica C:*
34 *Superconductivity*, **469**, 418–424 (2009). \diamond Cited on page 12.
- 35 **83** Yildirim, T. [Origin of the 150-K Anomaly in \$\text{LaFeAsO}\$: Competing Antiferromagnetic](#)
36 [Interactions, Frustration, and a Structural Phase Transition.](#) *Phys. Rev. Lett.*, **101**,
37 057010 (2008). \diamond Cited on page 12.

- 1 **84** Dai, J., Si, Q., Zhu, J.-X., and Abrahams, E. [Iron pnictides as a new setting for quantum](#)
2 [criticality](#). *Proceedings of the National Academy of Sciences*, **106**, 4118–4121 (2009).
3 ◇ Cited on page 13.
- 4 **85** Sefat, A. S., Singh, D. J., Jin, R., McGuire, M. A., Sales, B. C., and Mandrus, D.
5 [Renormalized behavior and proximity of BaCo₂As₂ to a magnetic quantum critical](#)
6 [point](#). *Phys. Rev. B*, **79**, 024512 (2009). ◇ Cited on page 13.
- 7 **86** Liu, R. H., et al. [Anomalous Transport Properties and Phase Diagram of the FeAs-Based](#)
8 [SmFeAsO_{1-x}F_x Superconductors](#). *Phys. Rev. Lett.*, **101**, 087001 (2008). ◇ Cited on
9 page 13.
- 10 **87** Luetkens, H., et al. [The electronic phase diagram of the LaO_{1-x}F_xFeAs superconductor](#).
11 *Nat Mater*, **8**, 305–309 (2009). ◇ Cited on page 13.
- 12 **88** Grafe, H.-J., et al. [⁷⁵As NMR Studies of Superconducting LaFeAsO_{0.9}F_{0.1}](#). *Phys. Rev.*
13 *Lett.*, **101**, 047003 (2008). ◇ Cited on page 13.
- 14 **89** Matano, K., Ren, Z. A., Dong, X. L., Sun, L. L., Zhao, Z. X., and qing Zheng, G.
15 [Spin-singlet superconductivity with multiple gaps in PrFeAsO_{0.89}F_{0.11}](#). *EPL (Europhysics*
16 *Letters)*, **83**, 57001 (2008). ◇ Cited on page 13.
- 17 **90** Ning, F., Ahilan, K., Imai, T., Sefat, A. S., Jin, R., McGuire, M. A., Sales, B. C., and
18 Mandrus, D. [⁵⁹Co and ⁷⁵As NMR Investigation of Electron-Doped High T_c Superconduc-](#)
19 [tor BaFe_{1.8}Co_{0.2}As₂ \(T_c = 22 K\)](#). *Journal of the Physical Society of Japan*, **77**, 103705
20 (2008). ◇ Cited on page 13.
- 21 **91** Uemura, Y. J., et al. [Magnetic-field penetration depth in K₃C₆₀ measured by muon spin](#)
22 [relaxation](#). *Nature*, **352**, 605–607 (1991). ◇ Cited on page 13.
- 23 **92** Hardy, W. N., Bonn, D. A., Morgan, D. C., Liang, R., and Zhang, K. [Precision measure-](#)
24 [ments of the temperature dependence of λ in YBa₂Cu₃O_{6.95}: Strong evidence for nodes](#)
25 [in the gap function](#). *Phys. Rev. Lett.*, **70**, 3999–4002 (1993). ◇ Cited on pages 13,
26 14 & 60.
- 27 **93** Sonier, J. E., et al. [New muon-spin-rotation measurement of the temperature depen-](#)
28 [dence of the magnetic penetration depth in YBa₂Cu₃O_{6.95}](#). *Phys. Rev. Lett.*, **72**, 744–747
29 (1994). ◇ Cited on page 13.
- 30 **94** Uemura, Y. J., et al. [Universal Correlations between T_c and \$\frac{n_s}{m^*}\$ \(Carrier Density over](#)
31 [Effective Mass\) in High-T_c Cuprate Superconductors](#). *Phys. Rev. Lett.*, **62**, 2317–2320
32 (1989). ◇ Cited on page 13.
- 33 **95** Uemura, Y. J., et al. [Basic similarities among cuprate, bismuthate, organic, Chevrel-](#)
34 [phase, and heavy-fermion superconductors shown by penetration-depth measurements](#).
35 *Phys. Rev. Lett.*, **66**, 2665–2668 (1991). ◇ Cited on page 13.
- 36 **96** Drew, A. J., et al. [Coexistence of Magnetic Fluctuations and Superconductivity in the](#)
37 [Pnictide High Temperature Superconductor SmFeAsO_{1-x}F_x Measured by Muon Spin](#)
38 [Rotation](#). *Physical Review Letters*, **101**, 097010 (2008). ◇ Cited on page 13.

- 1 **97** Franz, M. and Iyengar, A. P. [Superfluid Density of Strongly Underdoped Cuprate](#)
2 [Superconductors from a Four-Dimensional XY Model](#). *Phys. Rev. Lett.*, **96**, 047007
3 (2006). ◇ Cited on page 13.
- 4 **98** Iulian Hetel, M. R., Thomas R. Lemberger [Quantum critical behaviour in the superfluid](#)
5 [density of strongly underdoped ultrathin copper oxide films](#). *Nature Physics*, **3** (2007).
6 ◇ Cited on page 13.
- 7 **99** Schrieffer, J. R., Wen, X.-G., and Zhang, S.-C. [Spin-bag mechanism of high-temperature](#)
8 [superconductivity](#). *Phys. Rev. Lett.*, **60**, 944–947 (1988). ◇ Cited on page 13.
- 9 **100** Basov, D. N. and Timusk, T. [Electrodynamics of high- \$T_c\$ superconductors](#). *Rev. Mod.*
10 *Phys.*, **77**, 721–779 (2005). ◇ Cited on page 13.
- 11 **101** Li, W.-H., Lynn, J. W., and Fisk, Z. [Magnetic order of the Cu planes and chains in](#)
12 [\$\text{RBa}_2\text{Cu}_3\text{O}_{6+x}\$](#) . *Phys. Rev. B*, **41**, 4098–4111 (1990). ◇ Cited on page 13.
- 13 **102** Zhang, K., Bonn, D. A., Kamal, S., Liang, R., Baar, D. J., Hardy, W. N., Basov, D., and
14 Timusk, T. [Measurement of the \$ab\$ Plane Anisotropy of Microwave Surface Impedance](#)
15 [of Untwinned \$\text{YBa}_2\text{Cu}_3\text{O}_{6.95}\$ Single Crystals](#). *Phys. Rev. Lett.*, **73**, 2484–2487 (1994).
16 ◇ Cited on pages 13 & 14.
- 17 **103** Grabowski, S., Schmalian, J., and Bennemann, K. H. [Electronic theory for bilayer-](#)
18 [effects in high- \$t_c\$ superconductors](#). *Physica C: Superconductivity*, **282-287**, 1681 –
19 1682 (1997). ◇ Cited on page 13.
- 20 **104** Atkinson, W. A. and Sonier, J. E. [Role of CuO chains in vortex core structure in](#)
21 [\$\text{YBa}_2\text{Cu}_3\text{O}_{7-\delta}\$](#) . *Phys. Rev. B*, **77**, 024514 (2008). ◇ Cited on pages 13 & 14.
- 22 **105** Morr, D. K. and Balatsky, A. V. [Proximity Effects and Quantum Dissipation in the Chains](#)
23 [of \$\text{YBa}_2\text{Cu}_3\text{O}_{6+x}\$](#) . *Phys. Rev. Lett.*, **87**, 247002 (2001). ◇ Cited on page 13.
- 24 **106** Nunner, T. S. and Hirschfeld, P. J. [Microwave conductivity of \$d\$ -wave superconductors](#)
25 [with extended impurities](#). *Phys. Rev. B*, **72**, 014514 (2005). ◇ Cited on page 13.
- 26 **107** Friedmann, T. A., Rabin, M. W., Giapintzakis, J., Rice, J. P., and Ginsberg, D. M.
27 [Direct measurement of the anisotropy of the resistivity in the a-b plane of twin-free,](#)
28 [single-crystal, superconducting \$\text{YBa}_2\text{Cu}_3\text{O}_{7-\delta}\$](#) . *Phys. Rev. B*, **42**, 6217–6221 (1990). ◇
29 Cited on page 14.
- 30 **108** Gagnon, R., Lupien, C., and Taillefer, L. [\$T^2\$ dependence of the resistivity in the Cu-O](#)
31 [chains of \$\text{YBa}_2\text{Cu}_3\text{O}_{6.9}\$](#) . *Phys. Rev. B*, **50**, 3458–3461 (1994). ◇ Cited on page 14.
- 32 **109** Basov, D. N., Liang, R., Bonn, D. A., Hardy, W. N., Dabrowski, B., Quijada, M., Tanner,
33 D. B., Rice, J. P., Ginsberg, D. M., and Timusk, T. [In-Plane Anisotropy of the Penetration](#)
34 [Depth in \$\text{YBa}_2\text{Cu}_3\text{O}_{7-\delta}\$ and \$\text{YBa}_2\text{Cu}_4\text{O}_8\$ Superconductors](#). *Phys. Rev. Lett.*, **74**, 598–601
35 (1995). ◇ Cited on pages 14 & 66.
- 36 **110** Gros, C., Joynt, R., and Rice, T. M. [Superconducting instability in the large- \$U\$ limit of](#)
37 [the two-dimensional Hubbard model](#). *Zeitschrift für Physik B Condensed Matter*, **68**,
38 425–432 (1987). ◇ Cited on page 14.

- 111 Weng, Z. Y., Lee, T. K., and Ting, C. S. [d-wave superconducting condensation in the spin-density-wave background](#). Phys. Rev. B, **38**, 6561–6567 (1988). ◇ Cited on page 14.
- 112 Monthoux, P., Balatsky, A. V., and Pines, D. [Toward a theory of high-temperature superconductivity in the antiferromagnetically correlated cuprate oxides](#). Phys. Rev. Lett., **67**, 3448–3451 (1991). ◇ Cited on page 14.
- 113 Annett, J., Goldenfeld, N., and Renn, S. R. [Interpretation of the temperature dependence of the electromagnetic penetration depth in \$\text{YBa}_2\text{Cu}_3\text{O}_{7-\delta}\$](#) . Phys. Rev. B, **43**, 2778–2782 (1991). ◇ Cited on page 14.
- 114 Annet, J. F., Goldenfeld, N., and Renn, S. R. Physical properties of high temperature superconductors II, edited by D. M. Ginsberg. World Scientific (1989). ◇ Cited on page 14.
- 115 C. P. Poole, H. A. F. and Creswick, R. J. Superconductivity. Academic press, 2nd ed. edn. (1995). ◇ Cited on page 14.
- 116 Suter, A., Morenzoni, E., Khasanov, R., Luetkens, H., Prokscha, T., and Garifianov, N. [Direct Observation of Nonlocal Effects in a Superconductor](#). Phys. Rev. Lett., **92**, 087001 (2004). ◇ Cited on page 14.
- 117 Amin, M. H. S., Affleck, I., and Franz, M. [Low-temperature behavior of the vortex lattice in unconventional superconductors](#). Phys. Rev. B, **58**, 5848–5855 (1998). ◇ Cited on page 14.
- 118 Sonier, J. E., Hundley, M. F., Thompson, J. D., and Brill, J. W. [Low Field Anomaly in the Specific Heat of s-Wave Superconductors due to the Expansion of the Vortex Cores](#). Phys. Rev. Lett., **82**, 4914–4917 (1999). ◇ Cited on page 14.
- 119 Sonier, J. E., Brewer, J. H., and Kiefl, R. F. [μSR studies of the vortex state in type-II superconductors](#). Rev. Mod. Phys., **72**, 769–811 (2000). ◇ Cited on page 14.
- 120 Maisuradze, A., Khasanov, R., Shengelaya, A., and Keller, H. [Comparison of different methods for analyzing μSR line shapes in the vortex state of type-II superconductors](#). Journal of Physics: Condensed Matter, **21**, 075701 (15pp) (2009). ◇ Cited on page 14.
- 121 Sonier, J. E., et al. [Hole-doping dependence of the magnetic penetration depth and vortex core size in \$\text{YBa}_2\text{Cu}_3\text{O}_{6+x}\$: Evidence for stripe correlations near \(1/8\) hole doping](#). Physical Review B (Condensed Matter and Materials Physics), **76**, 134518 (2007). ◇ Cited on pages 14 & 66.
- 122 Sonier, J. E., Kiefl, R. F., Brewer, J. H., Chakhalian, J., Dunsiger, S. R., MacFarlane, W. A., Miller, R. I., Wong, A., Luke, G. M., and Brill, J. W. [Muon-Spin Rotation Measurements of the Magnetic Field Dependence of the Vortex-Core Radius and Magnetic Penetration Depth in \$\text{NbSe}_2\$](#) . Phys. Rev. Lett., **79**, 1742–1745 (1997). ◇ Cited on page 14.
- 123 Fiory, A. T., Hebard, A. F., Mankiewich, P. M., and Howard, R. E. [Renormalization of the Mean-Field Superconducting Penetration Depth in Epitaxial \$\text{YBa}_2\text{Cu}_3\text{O}_7\$ Films](#). Phys. Rev. Lett., **61**, 1419–1422 (1988). ◇ Cited on page 14.

- 1 **124** Ma, Z., Taber, R. C., Lombardo, L. W., Kapitulnik, A., Beasley, M. R., Merchant, P.,
2 Eom, C. B., Hou, S. Y., and Phillips, J. M. [Microwave penetration depth measurements](#)
3 [on \$\text{Bi}_2\text{Sr}_2\text{CaCu}_2\text{O}_8\$ single crystals and \$\text{YBa}_2\text{Cu}_3\text{O}_{7-\delta}\$ thin films](#) . *Phys. Rev. Lett.*, **71**,
4 781–784 (1993). \diamond Cited on page 14.
- 5 **125** Klein, N., Tellmann, N., Schulz, H., Urban, K., Wolf, S. A., and Kresin, V. Z. [Evidence of](#)
6 [two-gap \$s\$ -wave superconductivity in \$\text{YBa}_2\text{Cu}_3\text{O}_{7-\delta}\$ from microwave surface impedance](#)
7 [measurements](#). *Phys. Rev. Lett.*, **71**, 3355–3358 (1993). \diamond Cited on page 14.
- 8 **126** Gorter, C. *Paramagnetic Relaxation*, vol. 1 of *Course of Theoretical Physics*. Elsevier,
9 second edn. (1947). \diamond Cited on page 17.
- 10 **127** Blatt, F. [Modern physics](#). Physics series, McGraw-Hill (1992). \diamond Cited on page 17.
- 11 **128** Yang, C. N. [Concept of Off-Diagonal Long-Range Order and the Quantum Phases of](#)
12 [Liquid He and of Superconductors](#). *Rev. Mod. Phys.*, **34**, 694–704 (1962). \diamond Cited on
13 pages 20 & 21.
- 14 **129** Nieh, H. T., Su, G., and Zhao, B.-H. [Off-diagonal long-range order: Meissner effect and](#)
15 [flux quantization](#). *Phys. Rev. B*, **51**, 3760–3764 (1995). \diamond Cited on page 20.
- 16 **130** Sewell, G. L. [Off-diagonal long-range order and the Meissner effect](#). *Journal of*
17 *Statistical Physics*, **61**, 415–422 (1990). \diamond Cited on page 21.
- 18 **131** Fisher, M. P. A. [Vortex-glass superconductivity: A possible new phase in bulk high- \$T_c\$](#)
19 [oxides](#). *Phys. Rev. Lett.*, **62**, 1415–1418 (1989). \diamond Cited on page 21.
- 20 **132** Kuroki, K., Onari, S., Arita, R., Usui, H., Tanaka, Y., Kontani, H., and Aoki, H. [Unconven-](#)
21 [tional Pairing Originating from the Disconnected Fermi Surfaces of Superconducting](#)
22 [\$\text{LaFeAsO}_{1-x}\text{F}_x\$](#) . *Phys. Rev. Lett.*, **101**, 087004 (2008). \diamond Cited on page 21.
- 23 **133** Sigrist, M. and Rice, T. M. [Symmetry classification of states in high temperature](#)
24 [superconductors](#). *Zeitschrift für Physik B Condensed Matter*, **68**, 9–14 (1987). \diamond Cited
25 on page 21.
- 26 **134** Wenger, F. and Östlund, S. [\$d\$ -wave pairing in tetragonal superconductors](#). *Phys. Rev. B*,
27 **47**, 5977–5983 (1993). \diamond Cited on page 21.
- 28 **135** Li, Q. P., Koltenbah, B. E. C., and Joynt, R. [Mixed \$s\$ -wave and \$d\$ -wave superconductivity](#)
29 [in high- \$T_c\$ systems](#). *Phys. Rev. B*, **48**, 437–455 (1993). \diamond Cited on page 21.
- 30 **136** Zhang, S.-C. [A Unified Theory Based on \$\text{SO}\(5\)\$ Symmetry of Superconductivity and](#)
31 [Antiferromagnetism](#). *Science*, **275**, 1089–1096 (1997). \diamond Cited on page 21.
- 32 **137** Kirtley, J. R., Tsuei, C. C., Ariando, Verwijs, C. J. M., Harkema, S., and Hilgenkamp,
33 H. [Angle-resolved phase-sensitive determination of the in-plane gap symmetry in](#)
34 [\$\text{YBa}_2\text{Cu}_3\text{O}_{7-\delta}\$](#) . *Nat Phys*, **2**, 190–194 (2006). \diamond Cited on page 21.
- 35 **138** Kirtley, J. R., Tsuei, C. C., Sun, J. Z., Chi, C. C., Yu-Jahnes, L. S., Gupta, A., Rupp, M.,
36 and Ketchen, M. B. [Symmetry of the order parameter in the high- \$T_c\$ superconductor](#)
37 [\$\text{YBa}_2\text{Cu}_3\text{O}_{7-\delta}\$](#) . *Nature*, **373**, 225–228 (1995). \diamond Cited on page 21.

- 1 **139** Tsuei, C. C., Kirtley, J. R., Hammerl, G., Mannhart, J., Raffy, H., and Li, Z. Z. [Robust](#)
2 [d_{x²-y²} Pairing Symmetry in Hole-Doped Cuprate Superconductors](#). *Phys. Rev. Lett.*, **93**,
3 187004 (2004). ◇ Cited on page 21.
- 4 **140** Mazin, I. I. [Superconductivity gets an iron boost](#). *Nature*, **464**, 183–186 (2010). ◇
5 Cited on page 22.
- 6 **141** Mazin, I. I., Singh, D. J., Johannes, M. D., and Du, M. H. [Unconventional Superconduct-](#)
7 [ivity with a Sign Reversal in the Order Parameter of LaFeAsO_{1-x}F_x](#). *Phys. Rev. Lett.*,
8 **101**, 057003 (2008). ◇ Cited on page 22.
- 9 **142** Riseman, T. [Ph.D. Thesis: \$\mu\$ SR MEASUREMENT OF THE MAGNETIC PENETRATION](#)
10 [DEPTH AND COHERENCE LENGTH IN THE HIGH- \$T_C\$ SUPERCONDUCTOR](#)
11 [YBa₂Cu₃O_{6.95}](#). University Of British Columbia (1993). ◇ Cited on page 26.
- 12 **143** Morris, G. [Ph.D. Thesis: Muonium Formation and Diffusion in Cryocrystals](#). University
13 Of British Columbia (1997). ◇ Cited on page 26.
- 14 **144** Nakamura, K. and Group, P. D. [Review of Particle Physics](#). *Journal of Physics G: Nuclear*
15 *and Particle Physics*, **37**, 075021 (2010). ◇ Cited on page 26.
- 16 **145** Schenck, A. [Muon Spin Spectroscopy](#). Hilger, Bristol (1985). ◇ Cited on page 26.
- 17 **146** Cox, S. F. J. [Implanted muon studies in condensed matter science](#). *Journal of Physics*
18 *C: Solid State Physics*, **20**, 3187 (1987). ◇ Cited on page 26.
- 19 **147** Keller, H. [Muon-spin rotation experiments in high- \$T_c\$ superconductors and related](#)
20 [materials](#). *IBM Journal of Research and Development*, **33**, 314 –323 (1989). ◇ Cited
21 on page 26.
- 22 **148** Chow, K. [Ph.D. Thesis: Spin dynamics and electronic structure of muonium and its](#)
23 [charged states in silicon and gallium arsenide](#). University Of British Columbia (1994).
24 ◇ Cited on page 26.
- 25 **149** Luke, G. [Ph.D. Thesis: Quantum diffusion and spin dynamics of muons in copper](#).
26 University Of British Columbia (1988). ◇ Cited on page 26.
- 27 **150** Prokscha, T., Morenzoni, E., Deiters, K., Foroughi, F., George, D., Kobler, R., Suter, A.,
28 and Vrankovic, V. [The new \$\mu\$ E4 beam at PSI: A hybrid-type large acceptance channel](#)
29 [for the generation of a high intensity surface-muon beam](#). *Nuclear Instruments and*
30 *Methods in Physics Research Section A: Accelerators, Spectrometers, Detectors and*
31 *Associated Equipment*, **595**, 317 – 331 (2008). ◇ Cited on page 26.
- 32 **151** Luetkens, K. [Ph.D. Thesis](#). Gemeinsamen Naturwissenschaftlichen Fakultt der Tech-
33 nischen Universitat Carolo-Wilhelmina zu Braunschweig (2004). ◇ Cited on pages
34 27 & 28.
- 35 **152** Morenzoni, E., Glückler, H., Prokscha, T., Khasanov, R., Luetkens, H., Birke, M., Forgan,
36 E. M., Niedermayer, C., and Pleines, M. [Implantation studies of kev positive muons](#)
37 [in thin metallic layers](#). *Nuclear Instruments and Methods in Physics Research Section*
38 *B: Beam Interactions with Materials and Atoms*, **192**, 254 – 266 (2002). ◇ Cited on
39 pages 27 & 32.

- 1 **153** Ziegler, J. F. (2011), [The stopping and range of ions in matter](#). ◇ Cited on page 31.
- 2 **154** Eckstein, W. [Computer Simulation of Ion-Solid Interactions](#). Springer, Berlin (1991). ◇
3 Cited on page 31.
- 4 **155** Morenzoni, E., Prokscha, T., Suter, A., Luetkens, H., and Khasanov, R. [Nano-scale thin
5 film investigations with slow polarized muons](#). *Journal of Physics: Condensed Matter*,
6 **16**, S4583 (2004). ◇ Cited on page 32.
- 7 **156** Liang, R., Bonn, D. A., and Hardy, W. N. [Growth of high quality YBCO single crystals
8 using BaZrO3 crucibles](#). *Physica C: Superconductivity*, **304**, 105 – 111 (1998). ◇ Cited
9 on page 34.
- 10 **157** Doiron-Leyraud, N., Proust, C., LeBoeuf, D., Levallois, J., Bonnemaïson, J.-B., Liang, R.,
11 Bonn, D. A., Hardy, W. N., and Taillefer, L. [Quantum oscillations and the Fermi surface
12 in an underdoped high- \$T_c\$ superconductor](#). *Nature Publishing Group*, **447**, 565–568
13 (2007). ◇ Cited on page 34.
- 14 **158** Riseman, T. and Forgan, E. [Maximum entropy \$\mu\$ SR analysis i: planting the kernel](#).
15 *Physica B: Condensed Matter*, **326**, 226 – 229 (2003). ◇ Cited on page 38.
- 16 **159** Riseman, T. and Forgan, E. [Maximum entropy \$\mu\$ SR analysis ii: the search for truthful
17 errors](#). *Physica B: Condensed Matter*, **326**, 230 – 233 (2003). ◇ Cited on page 38.
- 18 **160** Riseman, T. and Forgan, E. [Maximum entropy \$\mu\$ SR analysis iii: automatic selection of
19 the default level and looseness factor](#). *Physica B: Condensed Matter*, **326**, 234 – 237
20 (2003). ◇ Cited on page 38.
- 21 **161** Wojek, B. M. [Superconductivity and magnetism in cuprate single crystals and thin-film
22 heterostructures](#). Ph.D. thesis, University of Zurich (2011). ◇ Cited on page 38.
- 23 **162** Jackson, T. J., et al. [Depth-Resolved Profile of the Magnetic Field beneath the Surface of
24 a Superconductor with a Few nm Resolution](#). *Phys. Rev. Lett.*, **84**, 4958–4961 (2000).
25 ◇ Cited on pages 40 & 66.
- 26 **163** Ni, N., Tillman, M. E., Yan, J.-Q., Kracher, A., Hannahs, S. T., Bud'ko, S. L., and
27 Canfield, P. C. [Effects of Co substitution on thermodynamic and transport properties
28 and anisotropic \$H_{c2}\$ in \$\text{BaCo}_x\text{Fe}_{2-x}\text{As}_2\$ single crystals](#). *Phys. Rev. B*, **78**, 214515 (2008).
29 ◇ Cited on page 58.
- 30 **164** Kim, H., et al. [London penetration depth in \$\text{Ba}\(\text{T}_x\text{Fe}_{1-x}\)_2\text{As}_2\$ \(\$\text{T}=\text{Co}, \text{Ni}\$ \) superconduct-
31 tors irradiated with heavy ions](#). *Phys. Rev. B*, **82**, 060518 (2010). ◇ Cited on page
32 62.
- 33 **165** Gordon, R. T., et al. [Unconventional London Penetration Depth in Single-Crystal
34 \$\text{Ba}\(\text{Co}_{0.07}\text{Fe}_{0.93}\)_2\text{As}_2\$ Superconductors](#). *Phys. Rev. Lett.*, **102**, 127004 (2009). ◇ Cited
35 on page 62.
- 36 **166** Luan, L., Auslaender, O. M., Lippman, T. M., Hicks, C. W., Kalisky, B., Chu, J.-H.,
37 Analytis, J. G., Fisher, I. R., Kirtley, J. R., and Moler, K. A. [Local measurement of the
38 penetration depth in the pnictide superconductor \$\text{Ba}\(\text{Co}_{0.05}\text{Fe}_{0.95}\)_2\text{As}_2\$](#) . *Phys. Rev. B*,
39 **81**, 100501 (2010). ◇ Cited on pages 62 & 66.

- 1 **167** Gross, F., Chandrasekhar, B. S., Einzel, D., Andres, K., Hirschfeld, P. J., Ott, H. R.,
2 Beuers, J., Fisk, Z., and Smith, J. L. [Anomalous temperature dependence of the](#)
3 [magnetic field penetration depth in superconducting UBe₁₃](#). *Zeitschrift für Physik B*
4 *Condensed Matter*, **64**, 175–188 (1986). ◇ Cited on page 62.
- 5 **168** Williams, T. J., et al. [Muon spin rotation measurement of the magnetic field penetration](#)
6 [depth in Ba\(Co_{0.074}Fe_{0.926}\)₂As₂: Evidence for multiple superconducting gaps](#). *Phys.*
7 *Rev. B*, **80**, 094501 (2009). ◇ Cited on page 62.
- 8 **169** Sonier, J. E., et al. [Magnetism and Disorder Effects on Muon Spin Rotation Measure-](#)
9 [ments of the Magnetic Penetration Depth in Iron-Arsenic Superconductors](#). *Phys. Rev.*
10 *Lett.*, **106**, 127002 (2011). ◇ Cited on page 62.
- 11 **170** Kogan, V. G., Martin, C., and Prozorov, R. [Superfluid density and specific heat within a](#)
12 [self-consistent scheme for a two-band superconductor](#). *Phys. Rev. B*, **80**, 014507 (2009).
13 ◇ Cited on page 62.
- 14 **171** Pereg-Barnea, T., Turner, P. J., Harris, R., Mullins, G. K., Bobowski, J. S., Raudsepp, M.,
15 Liang, R., Bonn, D. A., and Hardy, W. N. [Absolute values of the London penetration](#)
16 [depth in YBa₂Cu₃O_{6+x} measured by zero field ESR spectroscopy on Gd doped single](#)
17 [crystals](#). *Phys. Rev. B*, **69**, 184513 (2004). ◇ Cited on page 66.
- 18 **172** Ager, C., et al. [Angular-dependent muon-spin rotation and torque magnetometry on](#)
19 [the mixed state of the high-temperature superconductor YBa₂Cu₃O_{6+x}](#). *Phys. Rev. B*,
20 **62**, 3528–3533 (2000). ◇ Cited on page 66.
- 21 **173** Johnson, S. T., et al. [Flux-Line Lattice Structures in Untwinned YBa₂Cu₃O_{6+x}](#). *Phys.*
22 *Rev. Lett.*, **82**, 2792–2795 (1999). ◇ Cited on page 66.
- 23 **174** Prozorov, R., Tanatar, M., Gordon, R., Martin, C., Kim, H., Kogan, V., Ni, N., Tillman, M.,
24 Bud'ko, S., and Canfield, P. [Anisotropic london penetration depth and superfluid density](#)
25 [in single crystals of iron-based pnictide superconductors](#). *Physica C: Superconductivity*,
26 **469**, 582 – 589 (2009). ◇ Cited on page 66.
- 27 **175** Luan, L., Lippman, T. M., Hicks, C. W., Bert, J. A., Auslaender, O. M., Chu, J.-H., Analytis,
28 J. G., Fisher, I. R., and Moler, K. A. [Local Measurement of the Superfluid Density in the](#)
29 [Pnictide Superconductor BaCo_xFe_{2-x}As₂ across the Superconducting Dome](#). *Phys. Rev.*
30 *Lett.*, **106**, 067001 (2011). ◇ Cited on page 66.
- 31 **176** Lindstrom, M. [Asymptotic and numerical modeling of magnetic field profiles in](#)
32 [superconductors with rough boundaries and multi-component gas transport in PEM](#)
33 [fuel cells](#). University Of British Columbia (2010). ◇ Cited on page 67.
- 34 **177** Aeppli, G., Ansaldo, E. J., Brewer, J. H., Cava, R. J., Kiefl, R. F., Kreitzman, S. R., Luke,
35 G. M., and Noakes, D. R. [Magnetic penetration depth and flux-pinning effects in high-*T_c*](#)
36 [superconductor La_{1.85}SrO_{.15}CuO](#) . *Phys. Rev. B*, **35**, 7129–7132 (1987). ◇ Cited on
37 page 67.
- 38 **178** Huebener, R. P. [Flux Structures in Superconductors](#). Springer (2001). ◇ Cited on page
39 67.

- 1 **179** Konczykowski, M., Burlachkov, L. I., Yeshurun, Y., and Holtzberg, F. [Evidence for](#)
2 [surface barriers and their effect on irreversibility and lower-critical-field measurements](#)
3 [in Y-Ba-Cu-O crystals](#). Phys. Rev. B, **43**, 13707–13710 (1991). ◇ Cited on page 67.
- 4 **180** Dolan, G. J., Holtzberg, F., Feild, C., and Dinger, T. R. [Anisotropic vortex structure in](#)
5 [YBa₂Cu₃O₇](#). Phys. Rev. Lett., **62**, 2184–2187 (1989). ◇ Cited on page 67.
- 6 **181** Jooss, C., Forkl, A., Warthmann, R., Habermeier, H. U., Leibold, B., and Kronmüller, H.
7 [Thickness and roughness dependence of magnetic flux penetration and critical current](#)
8 [densities in YBa₂Cu₃O_{7-δ} thin films](#). Physica C: Superconductivity, **266**, 235 – 252
9 (1996). ◇ Cited on page 68.